NORTHWESTERN UNIVERSITY

Measurement of the W Boson Mass with the DØ Run II Detector using the Electron P_T Spectrum

A DISSERTATION

SUBMITTED TO THE GRADUATE SCHOOL

IN PARTIAL FULFILLMENT OF THE REQUIREMENTS

for the degree

DOCTOR OF PHILOSOPHY

Field of Physics and Astronomy

By

Timothy R. Andeen, Jr.

EVANSTON, ILLINOIS

June 2008

© Copyright by Timothy R. Andeen, Jr. 2008

All Rights Reserved

ABSTRACT

Measurement of the W Boson Mass with the DØ Run II Detector using the Electron P_T Spectrum

Timothy R. Andeen, Jr.

This thesis is a description of the measurement of the W boson mass using the DØ Run II detector with 770 pb^{-1} of $p\bar{p}$ collision data. These collisions were produced by the Tevatron at $\sqrt{s} = 1.96$ TeV between 2002 and 2006. We use a sample of $W \rightarrow e\nu$ and $Z \rightarrow ee$ decays to determine the W boson mass with the transverse momentum distribution of the electron and the transverse mass distribution of the boson. We measure $M_W = XXXXX \pm 37$ (stat.)± 26 (sys. theo.)± 51 (sys. exp.) MeV $= XXXXX \pm 68$ MeV with the transverse momentum distribution of the electron and $M_W = XXXXX \pm 28$ (stat.)± 17 (sys. theo.)± 51 (sys. exp.) MeV $= XXXXX \pm 61$ MeV with the transverse mass distribution.

Acknowledgements

Like most worthwhile endeavours this thesis would not have been possible without the help of many people. First I'd like to thank my collaborators, commiseraters and fellow grad students at NU who provided so much help and support: Sahal, Derek, Meghan and SungWoo. I'm sure I learned more from them than nearly anyone else. I owe much thanks to the NU postdocs and staff. It was from Harald, Jon and ("honorary" NU postdocs) Michael and Brendan that I first learned the mysteries of DØ . In between keeping everything at NU from falling to apart Bob always had time for lunch or coffee.

I thank Dave for the chance to monopolize a professor's ear for hours at a time driving to and from Fermilab. I don't think it is possible to overstate the amount I have learned from my advisor Jan and his contributions to this work are immense. None of this would have been possible without my professor Heidi, whom I will never be able to thank sufficiently for years of support and guidance.

From my most recent teachers I return to my first and most important teachers: my parents. After teaching me to take my first steps they have encouraged me at every subsequent step. Any success I find I owe to them; any thanks is too little. My sister Karen has kept right on my heels ever since she could walk, and hearing her footsteps coming up behind me as she also prepares to graduate has helped keep me focused. Almost like family are many old friends, particularly Arno and Jason, who did their best (despite little success) to keep me from spending too much time at work.

Great thanks is due the group of students and postdocs at DØ , particularly Junjie, Matt, Jun, Feng, Mikolaj and Jyotsna, for their immense help and efforts. Without their work the W mass would be unmeasurable. As professors Pierre, John and Sarah were a much appreciated source of guidance and advice. There were many others who have come and gone and I regretfully am leaving many out, but I certainly must thank Marco, Adam and Michiel.

In a life of relative good fortune, I feel I have been *most* fortunate to have had wonderful teachers, both those teachers with classrooms and those without. Though there are too many to mention here I am always conscious of their influence, grateful for their efforts and mindful of my debt to them.

My questioning was my observing of them; and their beauty was their reply.

Augustine of Hippo, *Confessions*, Book 10, 4th century.

Table of Contents

ABSTRACT 3

Acknowledgements 4

List of Tables 9

List of Figures 10

Chapter 1. Introduction 16

1.1. W and Z Bosons in the Standard Model 17

1.2. Motivation for a precision measurement of M_W 18

1.3. Past measurements of M_W 18

1.4. Overview of Experimental Method 20

Chapter 2. Theory 23

2.1. Overview 23

2.2. W and Z Production 38

2.3. W and Z Decay 47

Chapter 3. Experimental Apparatus 54

3.1. The DØ Experiment 55

Chapter 4. Data Samples 76

4.1. W and Z Selection 76

4.2. W and Z Events 84

Chapter 5. Simulation and Fitting 85

5.1. Fit Method 85

5.2. Event Generation 87

5.3. Electron Simulation 89

5.4. Overview 113

Chapter 6. Recoil Measurement 117

6.1. Recoil Simulation 117

6.2. Scalar E_T 132

6.3. Overview 133

Chapter 7. Backgrounds 138

7.1. $Z \rightarrow ee$ Background 138

7.2. $W \rightarrow \tau\nu$ 139

7.3. QCD Background 140

7.4. Uncertainties 144

Chapter 8. Systematic Uncertainties 145

8.1. Theoretical 147

8.2. Experimental 151

8.3. Summary of Systematic Uncertainty 153

Chapter 9. Results and Conclusion 155

9.1. Fitting Method 155

9.2. Fitting the Distributions 156

9.3. W Mass Measurement 170

9.4. Future Prospects 172

References 174

List of Tables

3.1	Z event η_{phys} categories.	71
4.1	Level 1 Trigger criteria.	78
4.2	Level 2 Trigger criteria.	79
4.3	Level 3 Trigger criteria.	79
4.4	Selection criteria for electron candidates.	83
5.1	The angular resolution of an electron.	92
5.2	The effect of the underlying event.	99
6.1	Average SET for different primary vertices in a Z event	123
7.1	Summary of backgrounds.	139
8.1	Experimental and theoretical systematic uncertainties.	154
9.1	Result of the MC closure test.	156
9.2	W Mass (blinded).	162
9.3	Experimental systematic uncertainties, $u_{\parallel} < 0$ GeV.	170

List of Figures

1.1	The mass of the top quark versus the mass of the W boson.	19
1.2	The W mass determined by the Tevatron and LEP.	21
2.1	The particles of the Standard Model.	24
2.2	An example of a one-loop diagram.	39
2.3	The one-loop contribution of the top and bottom.	39
2.4	W boson production and decay.	40
2.5	Z boson production and decay.	40
2.6	The parton model of W and Z boson production.	41
2.7	W boson production at next to leading order.	44
2.8	W boson production at next to leading order.	45
2.9	W^+ decay and the conservation of angular momentum.	48
2.10	The W^+ decay in its rest frame.	49
2.11	An electron transverse momentum distribution.	51
2.12	A transverse mass distribution.	52
2.13	The emission of a photon from the W boson.	52
2.14	The emission of a photon from one of the quarks.	53

2.15	The emission of a photon from an electron.	53
3.1	The Fermilab chain of accelerators in Batavia, IL.	55
3.2	The tick structure of the Tevatron beams.	56
3.3	The DØ Detector.	57
3.4	The SMT detector.	59
3.5	The CFT detector.	60
3.6	Overview of the innermost subsystems.	60
3.7	View of Central and End Cap Calorimeters.	62
3.8	Cell-level view of calorimeter.	65
3.9	Quarter calorimeter.	66
3.10	One calorimeter module. [**67**]	66
3.11	Longitudinal shower development.	69
3.12	Shower development and η_{phys}.	69
3.13	Shower development and energy.	70
3.14	EM fraction per category.	71
3.15	Fit for $\Delta n X_0$.	72
3.16	The luminosity monitor.	75
4.1	A schematic view of the DØ trigger and DAQ.	77
4.2	The W vertex distribution.	81
5.1	PMCS schematic.	87

5.2	A schematic view of a typical W event.	89
5.3	A typical $Z \rightarrow ee$ event.	90
5.4	A typical $W \rightarrow e\nu$ event.	91
5.5	The boundary between two EM calorimeter modules.	93
5.6	Electron efficiency vs ϕ position in detector module.	94
5.7	Difference between ϕ position from tracking and calorimeter.	94
5.8	The $u_{\parallel}$ definition.	96
5.9	Energy in rotated electron cone.	97
5.10	Energy in rotated cone as a function of instantaneous luminosity.	98
5.11	Energy in rotated cone as a function of $u_{\parallel}$.	98
5.12	The $Z \rightarrow ee$ invariant mass distribution.	100
5.13	An example of the f_Z vs. M_Z distribution.	102
5.14	The profile of the f_Z vs. M_Z distribution.	102
5.15	The EM energy offset pull distribution.	103
5.16	The EM energy scale pull distribution.	103
5.17	EM scale and offset fit.	104
5.18	Fractional energy dependence.	106
5.19	Fractional energy dependence.	106
5.20	Mass of J/ψ.	106
5.21	Trigger efficiency for v13 trigger list.	108
5.22	Trigger efficiency for v14 trigger list.	108

5.23	Pre-selection efficiency as a function of η_{det}.	109
5.24	Track matching efficiency.	109
5.25	Hmatrix efficiency as a function of η_{det}.	110
5.26	$u_{\|\|}$ in Z events.	111
5.27	$u_{\|\|}$ in W events.	111
5.28	Geant MC W and Z $u_{\|}$ efficiency slope vs η_{phys}.	112
5.29	$u_{\|}$ efficiency vs. η_{phys}.	112
5.30	$u_{\|}$ in Z events.	113
5.31	The electron p_T distribution in $Z \rightarrow ee$ events.	114
5.32	The electron η_{phys} distribution in $Z \rightarrow ee$ events.	114
5.33	The electron η_{det} distribution in $Z \rightarrow ee$ events.	115
5.34	The $u_{\|}$ distribution in $Z \rightarrow ee$ events.	115
5.35	The $u_{\perp}$ distribution in $Z \rightarrow ee$ events.	116
5.36	The $p_T(ee)$ distribution in $Z \rightarrow ee$ events.	116
6.1	Distribution of a 20 GeV recoil response and resolution.	121
6.2	Distribution of a 5 GeV recoil response and resolution.	122
6.3	Contribution of the underlying event.	123
6.4	The Scalar E_T in $Z \rightarrow ee$.	123
6.5	The scalar E_T of minimum bias events.	125
6.6	The scalar E_T of minimum bias events after weighting.	125

6.7	The instantaneous luminosity distribution of $Z \rightarrow ee$ events.	127
6.8	The $p_T(ee)$ distribution of $Z \rightarrow ee$ events.	127
6.9	The $p_T(rec)$ distribution of $Z \rightarrow ee$ events.	128
6.10	The UA2 coordinate system.	128
6.11	The $\eta_{\rm imb}$ distribution of $Z \rightarrow ee$ events.	129
6.12	The $\xi_{\rm imb}$ distribution of $Z \rightarrow ee$ events.	130
6.13	The mean of the $\eta_{\rm imb}$ distributions.	131
6.14	The width of the $\eta_{\rm imb}$ distributions.	132
6.15	$\Delta\phi$ between the di-electron and recoil momentum.	132
6.16	The $u_{\parallel}$ distribution in $Z \rightarrow ee$ events.	133
6.17	The $u_{\perp}$ distribution in $Z \rightarrow ee$ events.	134
6.18	The W recoil p_T distribution in data and PMCS.	135
6.19	W $u_{\parallel}$ distribution in data.	136
6.20	The W $u_{\perp}$ distribution in data and PMCS.	137
7.1	Electron p_T distribution, log scale.	140
7.2	M_T distribution, log scale.	141
7.3	The electron p_T in $W \rightarrow \tau\nu$.	142
7.4	The M_T in $W \rightarrow \tau\nu$.	142
7.5	Electron fake rate probability.	143
8.1	Electron p_T uncertainty due to the PDF.	148

8.2	M_T uncertainty due to the PDF.	149
9.1	The electron p_T distribution in $W \to e\nu$ events.	158
9.2	M_T distribution for $W \to e\nu$ events.	159
9.3	The $\not\!\!E_T$ distribution for $W \to e\nu$ events.	160
9.4	The W $u_\parallel$ distribution in data and PMCS.	161
9.5	The W boson p_T distribution for $W \to e\nu$ events.	163
9.6	W boson p_T distribution, $u_\parallel > 0$ GeV.	164
9.7	W boson p_T distribution, $u_\parallel < 0$ GeV.	165
9.8	Electron p_T distribution, $u_\parallel < 0$ GeV.	166
9.9	Electron p_T distribution, $u_\parallel > 0$ GeV.	167
9.10	M_T distribution, $u_\parallel < 0$ GeV.	168
9.11	M_T distribution, $u_\parallel > 0$ GeV.	169

CHAPTER 1

Introduction

Modern particle physics is the study of matter at the most fundamental level. The present frontier of particle physics probes particles and interactions at high energies by conducting experiments at large particle colliders. The high energies give us access to extremely small scales of distance ($< 10^{-18}$ m) and the chance to study the conditions of the very early universe in the laboratory. The Standard Model[1], developed and expanded during the last half of the 20th century and the early 21st, explains all particle physics phenomena observed by experiments. Its precision and completeness make it one of the most well-tested and precise theories constructed. This thesis aims to test the Standard Model through a precision measurement of the W boson mass.

This dissertation is organized as follows: We begin in the first chapter with a brief introduction to the measurement and necessary background information. In chapter two we review the aspects of the Standard Model most relevant for this measurement. Chapter three contains a description of the DØ detector, with an emphasis on the calorimeter calibration. Chapter four describes the data collected and the selection of the events. The simulation of electrons and the recoil in our parameterized Monte Carlo simulation is introduced in chapters five and six respectively. The experimental backgrounds are assessed in chapter seven. Chapter eight describes the systematic uncertainties, both

[1]The Standard Model (SM) will be more completely explicated in the coming chapters, however two useful introductory works are [**1**] and [**2**].

theoretical and experimental, and we conclude with the result, interpretation and future prospects in chapter nine.

1.1. W and Z Bosons in the Standard Model

W and Z bosons were first theoretically described as the massive vector bosons responsible for the electroweak interaction in the 1960's by Glashow [**3**], Weinberg [**4**] and Salam [**5**]. The subsequent observation and discovery of the W and Z bosons by the UA1 [**6**] and UA2 [**7**] collaborations at the $Sp\bar{p}S$ collider at CERN[2] in 1981 and 1983 was a triumph of theoretical and experimental particle physics, cementing the theory of electroweak interactions as a pillar of the Standard Model. Since the 1980's the Standard Model has been tested extensively with greater and greater precision. With each step our theoretical understanding deepens and the experimental precision increases, but the Standard Model remains an accurate description of physical phenomena at the highest accessible energies and smallest lengths. Yet the Standard Model remains incomplete. A description of gravity, though negligible at any present laboratory based accelerator, remains beyond the scope of the Standard Model. Of interest in this thesis is that the exact mechanism of symmetry breaking remains unknown, and the related Higgs boson undiscovered[3]. The broken symmetry is necessary to give the W and Z bosons mass [**8**]. The goal of this measurement is to use the largest available collection of W bosons, acquired with the DØ detector, to measure the mass of the W boson, one of the most important parameters predicted by the Standard Model.

[2]The European Organization for Nuclear Research
[3]The boson is named for Higgs [**8**], but Brout and Englert [**9**] are due equal credit.

1.2. Motivation for a precision measurement of M_W

A precise measurement of the W boson mass is a test of the Standard Model. Deviations between the predicted value and the measured value could be indications of new physics beyond the Standard Model. When combined with a measurement of the mass of the top quark it can be used to predict the mass of the Higgs boson. In figure 1.1 [**10**] the mass of the top quark is plotted versus the mass of the W boson. The two concentric circles are the 68% and 95% confidence limits of the current combination of the direct measurements of the top and W masses ($m_T = 172.6 \pm 1.4$ GeV, $M_W = 80.398 \pm 0.025$ GeV in [**10**]). In red are plotted possible Standard Model Higgs mass predictions, and in green are Higgs mass predictions for a common supersymmetric model. Recent improvements in the top mass measurements [**11**] help further motivate a precision W mass; a top mass uncertainty of 1.4 MeV corresponds to an uncertainty on the W mass only 8 MeV.

1.3. Past measurements of M_W

The most direct antecedents of this measurement of the W boson mass are the Tevatron Run I experiments (1990 to 1997) [**12**], [**13**] and [**14**]. The two detectors, DØ and CDF[4], both measured the W mass using approximately 82 pb^{-1} of data. In the case of DØ this was done using only the $W \to e\nu$ channel, measuring a mass of $M_W = 80.483 \pm 0.084$ GeV [**15**]. At CDF both the $W \to e\nu$ and W $\to \mu\nu$ channel were exploited to find $M_W = 80.433 \pm 0.079$ GeV [**16**].

[4]The Collider Detector at Fermilab, located at Tevatron interaction point BØ . DØ is named after its interaction point.

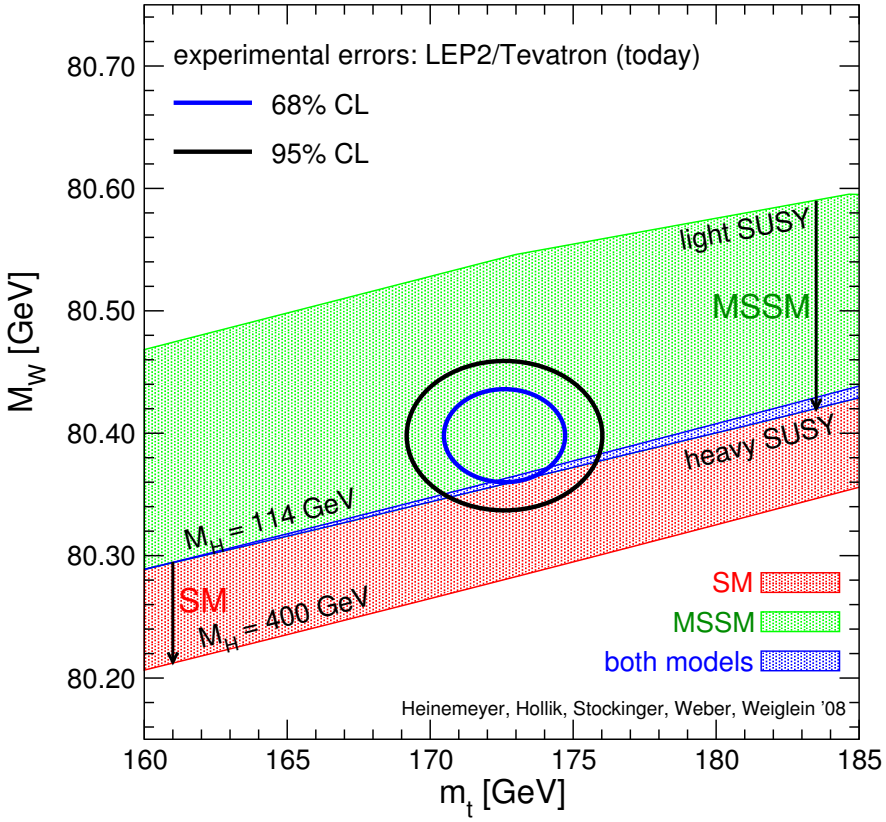


Figure 1.1. The mass of the top quark versus the mass of the W boson with Standard Model and supersymmetric predictions for Higgs masses shown in the red and green bands respectively. Recent improvements in the top mass measurements provide additional motivation for a precision W mass measurement. [**10**]

Between 1996 and 2000 four experiments[5] at the Large Electron-Positron (LEP) collider at CERN in Geneva, Switzerland collected data and measured the W mass [**17**]. The precisely tuned energy of the electron-positron collisions produced two W bosons, and their decay into either four quark jets, four leptons (two of which were neutrinos), or a combination of quarks and leptons, resulted in the most precise measurements of the W boson mass at the time. In addition to the tunable energy of the collisions, a distinct

[5]ALEPH, DELPHI, L3 and OPAL

advantage of the LEP experiments over the Tevatron experiments is their insensitivity to the theoretical description of the proton or anti-proton content. The combination of the measurements from the four LEP experiments give an average $M_W = 80376 \pm 33$ MeV [**17**].

The Tevatron and the DØ and CDF experiments were substantially upgraded between 1997 and 2001. At present the experiments are collecting data in Run II of the Tevatron, with $p\bar{p}$ collisions at $\sqrt{s} = 1.96$ TeV center of mass energy. The luminosity of the collider was upgraded and the over the course of Run II (2001 to 2009) the experiments expect to collect approximately 8 fb^{-1} of data. The CDF experiment used the first ~ 200 pb^{-1} of data to measure the W mass in 2007 [**18**]. Again CDF used the $W \to e\nu$ and W $\to \mu\nu$ decay channels to measure $M_W = 80413 \pm 48$ MeV. This measurement is the most precise single measurement of the W boson mass. With their large sample of W events the measurement was not statistically limited, but rather systematic uncertainties dominated. These measurements are summarized in the figure 1.2.

1.4. Overview of Experimental Method

This measurement of the W mass uses 770 pb^{-1} of data collected by the DØ detector, comprising most of the Run IIa data sample collected between 2002 and 2006[6]. In the Run II DØ detector it is possible to use both the $W \to e\nu$ and W$^{\pm} \to \mu^{\pm}\nu$ decay channels to measure the W mass. In this analysis we only use the $W \to e\nu$ channel. With the DØ detector the energy resolution for electrons is better than muons, and because the precision of measurement of the lepton energy in large part governs the final precision of the mass measurement the electron channel is chosen.

[6]The Run IIa sample is defined in greater detail in Chapter 4

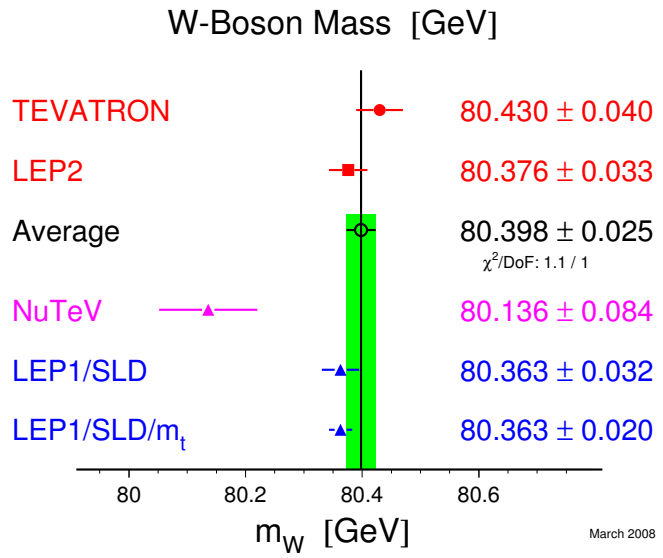


Figure 1.2. The W mass determined by the Tevatron and LEP accelerators. These are the averages of the individual experiments and include the recent result from CDF. [**17**]

The strategy of the measurement is, briefly, to calibrate the detector and tune a parameterized Monte Carlo simulation of the detector with the $Z \rightarrow ee$ events from the Run IIa sample. These events are very similar to the $W \rightarrow e\nu$ events but both decay products can be detected and the Z boson's mass can then be completely reconstructed. Additionally, the Z boson decay to two electrons is a well understood process. At the LEP collider the mass was measured with a precision greater than one part in ten thousand [**19**]. By calibrating the detector using these decays we are explicitly measuring the ratio of M_W/M_Z and depend on the much greater precision of the Z mass to derive M_W.

The neutrino from the W boson decay escapes the detector unobserved. This prevents us from determining the invariant mass of the W directly. Instead we can measure the W boson mass through the transverse mass distribution, the transverse momentum distribution of the electron, or the missing transverse momentum distribution. Of these

distributions the transverse mass has the greatest sensitivity to the W mass and historically, due to the limited number of W events, has been used to measure the mass. With the large data sample used in this analysis we are not statistically limited by the sensitivity of any of the distributions. In this measurement we use the transverse momentum distribution of the electron which is less sensitive to detector calibrations. As a result we expect to be able to reduce the experimental systematic uncertainty using this distribution.

To ensure that no bias was introduced by the experimenters themselves a random offset was added to the W mass while the analysis was begin developed. This is known as a "blind" analysis, and is used to prevent previous experimental and theoretical results from unduly influencing the analysis [**20**]. The random offset was only removed after the analysis strategy was finalized.

CHAPTER 2

Theory

This chapter describes the theoretical background pertinent to the measurement of the W boson mass. We begin with a somewhat historical overview of the Standard Model and the electroweak interactions. We briefly review the Higgs mechanism and electroweak symmetry breaking and the tree level predictions of the W mass. Higher order corrections to the mass are discussed and the production and decay of W and Z bosons at hadron colliders are explicated.

2.1. Overview

In this overview of the SM we follow several well-known texts, most notably [**2**], [**21**], and to a lesser extent [**22**], [**23**], [**1**]. The review articles of [**24**], [**25**], [**26**], [**27**] are also consulted, and detailed monographs on the subject of electroweak theory can be found in [**28**] and precision tests in [**29**]. Finally, the lecture notes of Prof. G. Anderson's course on the SM (Winter/Spring, 2003) at Northwestern University helped to provide background. Additional references are noted in the text.

2.1.1. The Standard Model

The Standard Model of particle physics is our most successful and complete theoretical description of Nature at the most fundamental level accessible[1]. It describes the most basic

[1]For this thesis we neglect the important observation of neutrino oscillations, whose explanation requires an extension of the Standard Model.

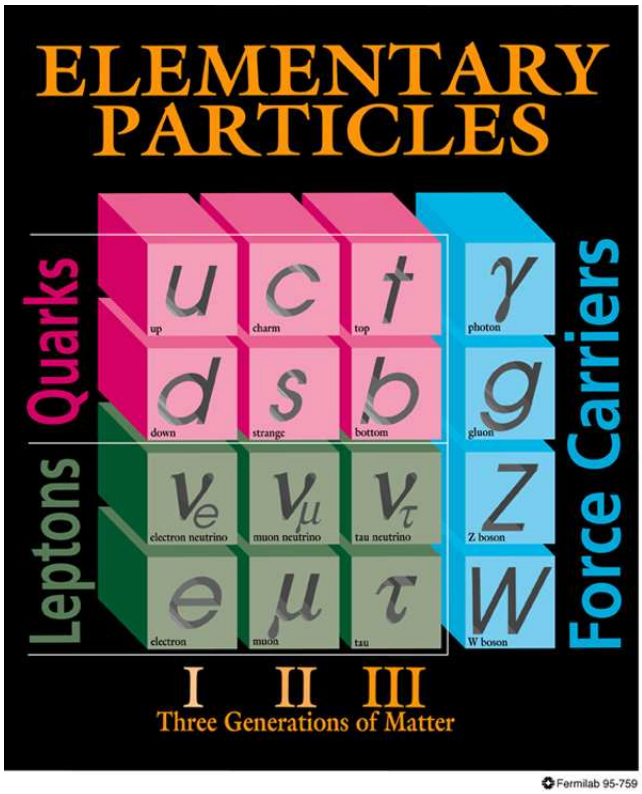


Figure 2.1. The particles of the Standard Model. The leptons and quarks are grouped into three generations, from the ordinary electrons, u and d quarks, to the higher mass copies such as the muon or the top.
[**30**]

units of matter with precision that equals our experimental ability to test. Experimentally, all fundamental particles are observed to be point-like and discrete. Theoretically, the fundamental particles are described as excitations above the vacuum state by the mathematics of quantum field theory.

In the Standard Model all fundamental particles are grouped into two categories by their intrinsic spin: fermions have half-integer spin and bosons have whole-integer spin. The fermions are divided into quarks and leptons and then further arranged into three generations, as seen in 2.1.

The first generation makes up nearly all familiar matter and consists of the up and down quarks and the electron and the electron neutrino. The second and third generations are identical copies of the first, but with higher masses. There is no fundamental explanation for why there are three generations of particles, and though there are reasons to believe there are only three generations it is possible there are additional, more massive, copies.

The other type of fundamental particles are the bosons. These particles mediate the interactions between particles and are the manifestation of the fields that describe the effects of the fundamental forces on the particles. For example, the photon is the boson which carries the electromagnetic force. Bosons are distinguished from fermions by integer spin, as opposed to the half-integer spin of the fermions. In the SM bosons are often referred to as "gauge" bosons[2] because the interactions which are mediated by these particles are described by gauge symmetries. The weak force, which was discovered in observations of nuclear β-decay, is mediated by three massive bosons: two charged W bosons and a neutral Z boson. The theory of electroweak interactions using $W^{\pm}$ and Z^0 particles, as well as photons, was first proposed by Glashow [**3**], Salam [**5**] and Weinberg [**4**] in the 1960's. This theory combined the description of the electromagnetic and weak forces and has since become, along with QED (electromagnetic interactions) and QCD (strong nuclear interactions), a central pillar of the Standard Model. The W and Z bosons were discovered with the properties predicted by the theory in the early 1980's at the UA1 [**6**] and UA2 [**7**] experiments. This measurement of the mass of the W boson is a continuation of that work. As the charged mediator of the electroweak force

[2]Except the scalar Higgs boson, which is not a gauge boson.

the W boson is fundamental to the SM. The ratio of the masses of the W and Z bosons is a parameter which is predicted by the Standard Model, and a comparison between the theoretical prediction and the experimental measurement is a basic test of the theory.

The final boson of the SM is the gluon. The gluon carries the strong force which binds the quarks together, such as within the nuclei. The theory of strong interactions is Quantum Chromodynamics (QCD). Here the Greek prefix "chromo" refers to the fact that, unlike electromagnetism with just one type of charge, the strong force has three charges, named after colors. This color has nothing to do with color as we see it and is only a name.

The graviton is occasionally also included in the list of bosons as the carrier of gravitational force. However, the description of gravity in the Standard Model remains incomplete and the graviton has never been observed. The SM is sometimes referred to as the theory of the very small, and though on the scale of planets and stars gravity is most the most important force, for precision measurements of the W boson it is entirely negligible.

2.1.1.1. The Development of Electroweak Interactions. The discovery and development of theory of electroweak interactions encompasses some of the most interesting and surprising theoretical and experimental work of 20th century particle physics[3]. Weak interactions were first observed in nuclear β-decay (though not identified as such) by Henri Becquerel in 1896 [**31**]. In this reaction electrons are emitted by an unstable atom

[3]It is traditional to discuss the history of the particle physics from the time of the ancient Greeks. Though Democritus and his "atomic" theory are often mentioned we believe that the most direct link is as follows: The Greeks invented democracy, which inspired Plato to write *The Republic*, which was read and studied by America's founding fathers. They established a government which in the 1940's created a national laboratory system. These labs were critical to the discovery and testing of the Standard Model.

whose atomic number increases by one. This process could not be described by the existing theories of the electromagnetic or strong force, so the weak force was proposed. More importantly, the continuous electron momentum spectrum from this reaction, first observed by Chadwick and Geiger in 1914 [**32**], appeared to violate the conservation of momentum. In order to restore momentum conservation Wolfgang Pauli [**33**] suggested that an unobserved particle was produced in this reaction: the neutrino. The reaction is then $n \rightarrow p + e^- + \bar{\nu_e}$. Enrico Fermi (1934, [**34**]) developed the first theory of weak interactions assuming they would be analogous to electromagnetic interactions. Instead of a massless boson like the photon the short-range nature of the force requires a massive boson. Fermi's theory was able to predict the properties of β-decay by assuming that the interaction was essentially point-like and could be described by the four-fermion coupling G_F.

The demonstration of the uniqueness of the weak force was further enhanced by Lee and Yang (1956, [**35**]). In a review of data on weak interactions they proposed that weak interactions are parity violating. Parity, or "mirror," symmetry was thought to be a conserved symmetry in any physical reaction. The experiments of Wu et al. in 1957 [**36**] demonstrated that weak interactions *maximally* violated parity. Maximal parity violating interactions are described by equations having the form $V - A$, where V is a polar vector (not parity violating) and A is an axial vector (parity violating). As a consequence of the $V-A$ form of the interaction only the left-handed components of the electron and neutrino fields participate in weak decays. Here "left-handed" refers to the negative helicity state of the particle. In other words, only right-handed $\bar{\nu_e}$ and left-handed e^- are involved in β decay. Additional confirmation came from observations of pion decay. All ν were found

to be left-handed and all $\bar{\nu}$ were right-handed. This is only exactly true if the neutrino is massless, and though this is now known to not be exactly true, the approximation of massless neutrinos is acceptable for this thesis.

One of the overarching themes of modern physics is the use of symmetry in describing nature. Noether's discovery that conservation laws can be derived from the physical symmetries of a system has proven useful again and again [**23**]. The symmetry of electroweak interactions is a gauge symmetry, which means that the equations describing the interactions are invariant under local phase transformations. The idea that the transformations should be locally invariant, instead of merely globally invariant, is a powerful idea first proposed in connection with nuclear physics by Yang and Mills in 1954 [**37**]. Most importantly, gauge invariance ensures the self-consistency of the theory.

A consequence of requiring a symmetry to be gauge invariant is that a field associated with a massless boson is introduced for each gauge invariant symmetry [**38**]. In the case of electromagnetism (QED) this massless boson is the photon. The W and Z bosons are massive, making the symmetries of the weak interaction a difficult candidate for gauge invariance. One could add the mass of the W and Z bosons to the theory "by hand," but one finds any mass term for the bosons breaks the gauge invariance. This is because the electroweak symmetry is non-Abelian and describes both particle and antiparticle fields at the same time. The ingenious device which allows massive gauge bosons is the Higgs mechanism [**8**], which spontaneously breaks the electroweak symmetry. By adding a massive Higgs boson we avoid the unitarity violation that would usually be caused by the massive gauge bosons. Before discussing the Higgs mechanism we first examine the motivation for the specific symmetry of the electroweak interaction: $SU(2)_L \times U(1)$.

2.1.1.2. Electroweak Symmetry Breaking. Weak charged-current interactions link the left-handed electron and the right-handed anti-neutrino. These particles (and the second and third generation counterparts) are paired into a doublet under the $SU(2)_L$ group for weak isospin. In the course of this development we will show that the group $SU(2)_L \times U(1)$ describes a unified the weak and electromagnetic force. Only the first generation of leptons are considered. For the other lepton generations and the quarks a similar procedure may be followed. In this section we closely follow the discussion found in chapters 17, 19 and 22 of [**2**], and also make use of [**1**], [**21**].

We first define the $SU(2)_L$ doublet for the electron and neutrino. The electron and neutrino themselves are complex fields, and in the following $e_L,\ e_R,\ \nu_L,\ \nu_R$ are understood to be the field operator:

$$L \equiv \begin{pmatrix} \nu_{eL} \\ e_L \end{pmatrix}, \quad \begin{matrix} t_3 = +1/2 \\ t_3 = -1/2 \end{matrix}, \ t = \frac{1}{2},\ y = -1 \tag{2.1}$$

$$R \equiv (e_R)\,,\ t = 0,\ y = -2 \tag{2.2}$$

where the subscripts L and R refer to the the left-handed or right-handed fields. The weak isospin t is $1/2$ for the left handed fields and 0 for the right handed fields, and t_3 is the third component of the weak isospin. The hypercharge y is defined below. The left handed and right handed fields are generically defined as:

$$\begin{aligned} \phi_L &= \tfrac{(1+\gamma_5)}{2}\phi \\ \phi_R &= \tfrac{(1-\gamma_5)}{2}\phi \end{aligned} \tag{2.3}$$

The SU(2) symmetry means that the theory is invariant under transformations of the sort

$$L_e \rightarrow e^{i\alpha\cdot\tau/2} L_e \tag{2.4}$$

where τ are the Pauli matrices. It is interesting to contrast the present case with an early use of SU(2) symmetry by Heisenberg in 1932 [**39**]. In that instance the nearly identical masses of the proton and neutron motivated the idea that, with respect to the strong force, the proton and neutron were completely degenerate. Therefore a single proton or neutron wave function could be described by an arbitrary linear combination of proton and neutron wave functions. In our case the electron and neutrino are clearly not mass degenerate so we already know this symmetry must be broken.

The U(1) symmetry was first introduced to the study of electroweak theory by Glashow in 1961 [**3**] and can be understood heuristically as the inclusion of electromagnetism. The weak hypercharge y is then related to the electric charge Q by Gell-Mann-Nishijima formula:

$$Q = t_3 + \frac{y}{2} \tag{2.5}$$

where t_3 is the third component of the weak isospin.

The gauge invariant Lagrangian which describes the electroweak interactions is

$$\mathcal{L}_G = \tilde{L} i\gamma^\mu D_\mu L + \tilde{R} i\gamma^\mu D_\mu R + \frac{1}{4} F_{\mu\nu} F^{\mu\nu} + \frac{1}{4} \mathbf{F}_{\mu\nu} \mathbf{F}^{\mu\nu}. \tag{2.6}$$

The term $F_{\mu\nu}$ is the field strength tensor of a vector field B_μ

$$F_{\mu\nu} = \partial_\mu B_\nu - \partial_\nu B_\mu. \tag{2.7}$$

Examining just the U(1) symmetry, if we only required global invariance then the Lagrangian would be invariant under a transformation $e_L \rightarrow e^{-i\alpha} e_L$. With requirement of local gauge invariance the Lagrangian is invariant under the transformation

$$e_L \rightarrow e^{-i\alpha(x)} e_L \tag{2.8}$$

where α is a function of x^μ. This also implies that

$$B_\mu \rightarrow B_\mu + \frac{2}{g'} \partial_\mu \alpha(x). \tag{2.9}$$

In a similar manner, requiring the SU(2) weak isospin symmetry to be locally gauge invariant introduces three fields $\mathbf{W}_\mu = \vec{W}_\mu \cdot \vec{\tau}/2$ where $\vec{\tau}$ are the Pauli matrices. The field strength tensor for $\mathbf{W}$ is then

$$F^a_{\mu\nu} = \partial_\mu W^a_\nu - \partial_\nu W^a_\mu + ig\epsilon^{abc} W^b_\mu W^c_\nu. \tag{2.10}$$

Finally, the covariant derivative for a gauged $SU(2)_L \times U(1)$ symmetry is $D_\mu = \partial_\mu - i\frac{g}{2} Y B_\mu + ig\mathbf{W}_\mu$. In order to recover the electromagnetic covariant derivative we identify $e = g \sin\theta_W$.

This completely describes a gauge theory of electroweak interactions with an unbroken $SU(2)\times U(1)$ symmetry. As such it has four massless gauge boson fields W^+, W^-, W^0 and B. The world we observe is quite different having three massive gauge fields and a broken SU(2) symmetry. If this electroweak Lagrangian is useful a method is needed to give the gauge bosons mass and break the SU(2) symmetry without losing gauge invariance and preserving the U(1) symmetry. The Higgs mechanism does exactly this.

2.1.1.3. The Higgs Mechanism. The salient physics of the Higgs mechanism can be understood by studying a local U(1) symmetry. We introduce a complex scalar field ϕ

$$\hat{\phi} = \frac{1}{\sqrt{2}} \left(\hat{\phi_1} - i\hat{\phi_2} \right). \tag{2.11}$$

The Lagrangian then includes the usual terms of the locally invariant U(1) with a potential V which depends on ϕ

$$\mathcal{L}_H = (D_\mu \phi^\dagger)(D^\mu \phi) - \frac{1}{4} F_{\mu\nu} F^{\mu\nu} + V(\phi). \tag{2.12}$$

where D_μ is the covariant derivative $\partial_\mu + iqA_\mu$. The potential can be defined such that the classical minimum is not at zero:

$$V = \frac{1}{4}\lambda(\phi^\dagger\phi)^2 - \mu^2\phi^\dagger\phi \tag{2.13}$$

with $\mu^2, \lambda > 0$. In this case the classical minimum is at

$$(\phi^\dagger\phi) = 2\mu^2/\lambda \equiv \nu^2/2. \tag{2.14}$$

Quantum mechanically particles are described as excitations from the vacuum and here the minimum of the vacuum is not at 0. We must expand the fields around the correct vacuum; in this case a circle of minima. In polar coordinates, we set the radius $\rho = \nu$ and $\theta_0 = 0$. Angular oscillations in the θ direction do not see any potential and remain massless. Therefore we expand ϕ around the minimum ν and write

$$\phi(x) = \frac{1}{\sqrt{2}}(\nu + h(x))e^{-i\theta(x)/\nu}. \tag{2.15}$$

This gives the Lagrangian a mass term for the h field leaving the θ field massless. The Higgs mechanism has spontaneously broken the U(1) symmetry with a non-zero vacuum expectation value of the scalar potential field and we have one massless Goldstone boson and one massive boson, corresponding to the scalar particle. So far all we have done is to break the symmetry and add a massive scalar particle which we do not observe in nature. However, we recall that this U(1) symmetry is a gauge symmetry, and that the ϕ field is invariant under the transformation

$$\phi \rightarrow e^{-i\alpha(x)}\phi. \tag{2.16}$$

We are free to choose any phase for ϕ and comparing 2.16 and 2.15 it is clear that we can simply "gauge" away the θ field by choosing $\alpha(x) = -\theta(x)/\nu$. Remarkably, we are left with just

$$\phi(x) = \frac{1}{\sqrt{2}}(\nu + h(x)) \tag{2.17}$$

from 2.15. When inserted into the Lagrangian 2.12 and writing only the terms quadratic in the fields one finds

$$\mathcal{L}^{quad}_{Higgs} = -\frac{1}{4}(\partial_\mu A_\nu - \partial_n u A_m u)(\partial^\mu A^\nu - \partial^n u A^m u) + \frac{1}{2}q^2\nu^2 A_\mu A^\mu + \frac{1}{2}\partial_\mu h \partial^\mu h - \mu^2 h^2. \tag{2.18}$$

This is the Lagrangian for a massive vector boson field (mass = $q\nu$) and a scalar field with mass $\sqrt{2}\mu$, the mass of the Higgs boson. The U(1) symmetry has been broken by the potential, but the gauge symmetry remains. This is exactly what is needed in the electroweak theory, at the cost of introducing the Higgs boson.

With the $SU(2)_L \times U(1)$ symmetry of the electroweak theory the procedure to introduce the Higgs Mechanism is the same except now the Higgs field is a scalar $SU(2)_L$ doublet

$$\hat{\phi} = \begin{pmatrix} \hat{\phi^+} \\ \hat{\phi^0} \end{pmatrix} \tag{2.19}$$

with a vacuum expectation value of

$$\langle 0|\hat{\phi}|0\rangle = \begin{pmatrix} 0 \\ \nu/\sqrt{2} \end{pmatrix}. \tag{2.20}$$

Fluctuations around this vacuum expectation value are now parameterized by

$$\hat{\phi} = \begin{pmatrix} 0 \\ \frac{1}{\sqrt{2}}(\nu + \hat{H}) \end{pmatrix}. \tag{2.21}$$

This parametrization was first suggested by Weinberg in 1967 [**4**]. It has the interesting property that this choice of the vacuum value does not break the U(1) symmetry, or the third component of the SU(2) symmetry. Going back to eqn. 2.5 we see that the electric charge Q is still a conserved quantity, as is expected.

The Lagrangian is now $\mathcal{L}_H + \mathcal{L}_G$, and after breaking the symmetry we can combine the quadratic terms and write

$$\begin{aligned}
&\mathcal{L}_{Mass} = \tfrac{1}{2}\partial_\mu H \partial^\mu H - \mu^2 H^2 \\
&-\tfrac{1}{4}(\partial_\mu W_{1\mu} - \partial_\mu W_{1\mu})(\partial^\mu W_1^\mu - \partial^\mu W_1^\mu) + \tfrac{1}{8} g^2 \nu^2 W_{1\mu} W_1^\mu \\
&-\tfrac{1}{4}(\partial_\mu W_{2\mu} - \partial_\mu W_{2\mu})(\partial^\mu W_2^\mu - \partial^\mu W_2^\mu) + \tfrac{1}{8} g^2 \nu^2 W_{2\mu} W_2^\mu \\
&-\tfrac{1}{4}(\partial_\mu W_{3\mu} - \partial_\mu W_{3\mu})(\partial^\mu W_3^\mu - \partial^\mu W_3^\mu) - \tfrac{1}{4} G_{\mu\nu} G^{\mu\nu} \\
&+\tfrac{1}{8}\nu^2 (g W_{3\mu} - g' B_\mu)(g W_3^\mu - g' B^\mu).
\end{aligned} \tag{2.22}$$

This includes a scalar field with a mass $M_H = \sqrt{2}\mu$ and two gauge bosons with mass $M_W = g\nu/2$. The W_3 and B fields are mixed in the last term, but we can untangle this with the orthogonal, linear combinations

$$\begin{aligned}
Z^\mu &= \cos\theta_W W_3^\mu - \sin\theta_W B^\mu \\
A^\mu &= \sin\theta_W W_3^\mu + \cos\theta_W B^\mu
\end{aligned} \tag{2.23}$$

where the angles are defined by

$$\cos\theta_W = g/(g^2 + g'^2)^{1/2} \quad \sin\theta_W = g'/(g^2 + g'^2)^{1/2}. \tag{2.24}$$

As a consequence we may write

$$M_Z = M_W/\cos\theta_W, \; M_A = 0 \tag{2.25}$$

and we associate the A field with the photon.

We began with the $SU(2)_L \times U(1)$ gauge symmetry. This came with four massless gauge boson fields. We spontaneously broke the symmetry of $SU(2)_L \times U(1)$ by introducing the Higgs potential which added three massless and one massive scalar fields. The three massless gauge fields "swallowed" three of the massless scalar fields (Goldstone bosons), leading to three massive gauge boson fields which we associate with the $W^{\pm}$ and the Z^0 and one remaining massless gauge boson field, the photon. The cost was the as yet unobserved, massive, scalar Higgs boson.

2.1.1.4. Tree Level Mass. In the previous sections we have found the tree level predictions for the masses of the bosons[4]. By comparing to Fermi's theory nuclear-β decay we can identify

$$\frac{G_F}{\sqrt{2}} = \frac{g^2}{8M_W^2}. \tag{2.26}$$

Recalling that $e = g \sin\theta_W$, we can predict

$$M_{W\ \text{tree}} = \left(\frac{\pi\alpha}{\sqrt{2}G_F}\right)^{1/2} \frac{1}{\sin\theta_W} \approx 77\ \text{GeV}. \tag{2.27}$$

The discovery of the W boson at approximately this mass at the UA1 [**6**] and UA2 [**7**] experiments in the early 1980's was a significant validation of the theory. Presently we need a more precise theoretical description.

The extension of this theory to the other lepton generations proceeds in exactly the same way. In considering the quarks, we have to account for the fact that their mass eigenstates are not the same as their weak eigenstates. The quarks are grouped into family by mass. Therefore, in weak interactions the quarks may mix between the mass families. This is described by the Cabibbo-Kobayashi-Maskawa transformation matrix

[4] "Tree level" referes to the leading order diagrams of the interaction, as shown in figure 2.4.

[**40**], [**41**], which transforms the strongly interacting quark fields with mass m to the weak eigenstate basis.

$$\begin{pmatrix} d' \\ s' \\ b' \end{pmatrix} = \begin{pmatrix} V_u d & V_u s & V_u b \\ V_c d & V_c s & V_c b \\ V_t d & V_t s & V_t b \end{pmatrix} \begin{pmatrix} d \\ s \\ b \end{pmatrix}. \tag{2.28}$$

2.1.1.5. Beyond Tree Level. At the tree level, if one separates out the fermion masses and mixings and the Higgs mass, the electroweak Lagrangian can be completely described with just three free parameters. It is common to choose α_{EM}, G_F, and M_Z. These parameters are determined experimentally and then used as input to the theory. This combination is then used to predict other observables. By measuring these other observables and comparing them to the predictions we can verify or falsify the theory. We can use the measurement of M_W in two of these steps. First, M_W will be used to test the validity of the electroweak theory. Small discrepancies between the data and the theory could be indicative of new physics beyond the Standard Model. Second, we will use M_W as an input into the theory in order to predict M_H.

The physical processes we measure are not restricted to leading order diagrams, but the framework we have developed is. For the desired precision we need to include loop corrections to the tree level theory. The inclusion of these corrections requires higher orders in perturbation theory which then changes not only the predictions for the observables, but also the relationships between them. When including the higher order terms it is necessary to renormalize the theory in order to remove unphysical divergences. For our purposes it is sufficient to adopt the on-shell renormalization scheme, proposed by Sirlin

[**42**], [**43**]. In this scheme

$$\sin^2\theta_W = 1 - \frac{M_W^2}{M_Z^2} \equiv s_W^2 \tag{2.29}$$

is taken as the definition of the renormalized $\sin^2\theta_W$ and which is valid to all orders. This is the a relatively simple definition and has the advantage of using the ratio of the masses, a well defined and measurable quantity. Once we have chosen on-shell renormalization the correction to M_W is parameterized with Δr

$$M_W^2 = \frac{\pi\alpha}{G_F\sqrt{2}}\frac{1}{s_W^2(1-\Delta r)} \tag{2.30}$$

where Δr includes all the radiative corrections. Two contributions to Δr are particularly important. The first is the effect of the Higgs loop, as shown in figure 2.2. This is the diagram for a W radiating and then reabsorbing a virtual Higgs boson. This contributes to the W mass as $\Delta M_W \propto \ln M_H^2$. The second contribution comes from the fermion masses, shown in figure 2.3. Here the correction goes as $\Delta M_W \propto M_t^2 - M_b^2$ [**44**], [**29**], where only the third generation fermions have a large contribution. Extra generations, or physics beyond the Standard Model could also have a similar contribution.

2.2. W and Z Production

The theoretical background immediately relevant to understanding this measurement of the M_W is the description of W and Z production from $p\overline{p}$ collisions and their subsequent decay to an electron and neutrino. In this section we will first deal with W and Z production (we refer to [**45**] for a general discussion). At the Tevatron at leading order the W and Z bosons are produced from $q\bar{q} \rightarrow W$ annihilation (figures 2.4 and 2.5). This process is best described using the parton model of quarks.

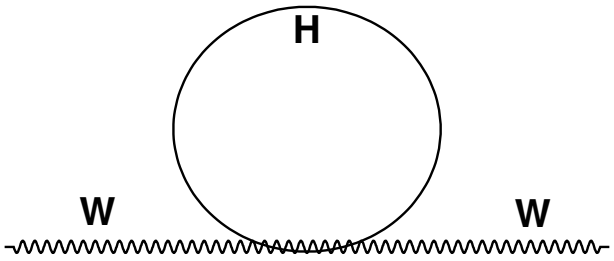


Figure 2.2. An example of a one-loop diagram in which the Higgs boson contributes to the W boson mass. This contribution goes as the $\ln M_H^2$.

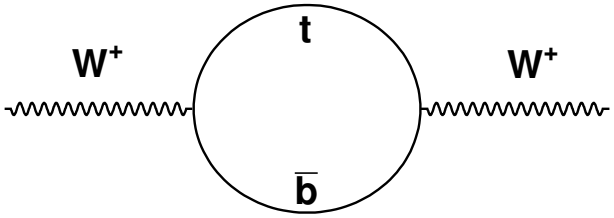


Figure 2.3. The one-loop contribution of the top and bottom quarks to the W boson mass. This contribution goes as the $M_t^2 - M_b^2$.

In a naive simplification protons and anti-protons are made up of three quarks: uud ($\bar{u}\bar{u}\bar{d}$ for the anti-proton). The W^+, for example, is created by the combination of u from the proton and a $\bar{d}$ from the anti-proton (2.6). However, this picture is not adequate for the energy of the $p\bar{p}$ collisions at the Tevatron. It is necessary to quantitatively treat the proton as a object consisting of a set of partons, which come in seven flavors, one for each of the six quarks, and one for the gluons. The distribution of the fraction of the total proton

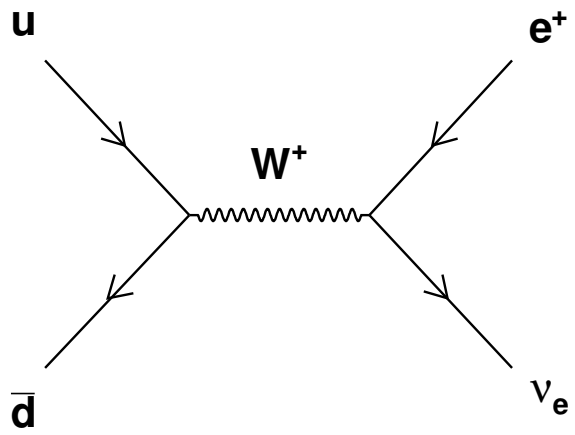


Figure 2.4. W boson production and decay at tree level.

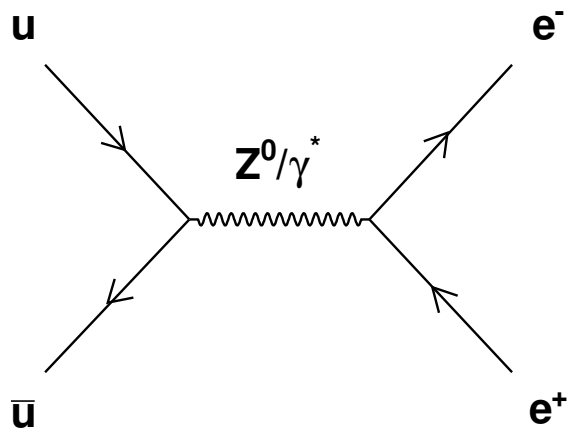


Figure 2.5. Z/γ^* production and decay at tree level.

momentum, x, carried by a parton with flavor i, when probed at the momentum scale Q^2 is described by a parton distribution function (PDF). A set of seven of these functions then completely describes the structure of the proton. These parton distribution functions are determined by combining and fitting the results of experiments such as ZEUS at DESY[5],

[5]DESY is the Deutsches Elektronen-Synchrotron in Hamburg Germany at which ZEUS was one of two large experiments (H1 being the other).

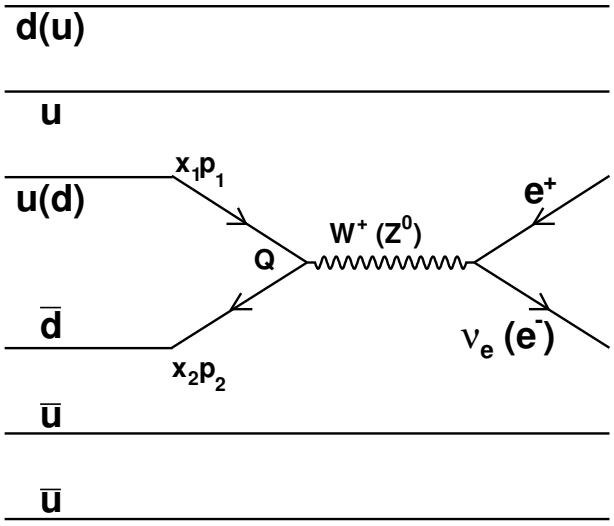


Figure 2.6. The parton model of W and Z boson production in $p\bar{p}$ collisions. x_i is the momentum fraction carried by a parton. At the Tevatron $x \simeq 0.04$. The partons which were part of the original proton (or anti-proton) which did not participate in the hard scatter are called spectator partons.

which probes the proton structure with high energy electrons. The PDF fitting is done by the CTEQ collaboration in the U.S. (or alternatively the MRST group in the U.K.). As combinations of experimental results the PDFs are naturally associated with some systematic uncertainty and methods have been developed to take this into account [**46**], [**47**].

The cross section for boson production can be calculated using the parton-level cross-section, convoluted with the PDF. The advantage of the parton model is that the parton level cross-section is found by treating the partons as fundamental particles. The partons not involved in the hard scatter are called spectator partons. Experimentally, these spectator partons are involved in hadronic interactions which are detected as many low energy particles. This is defined as the underlying event. The underlying event resembles

inelastic $p\bar{p}$ events, which are experimentally are called "minimum bias" events, referring to their very loose selection.

The parton level cross-section for the relativistic Breit-Wigner resonance produced by the two spin 1/2 quarks creating a spin 1 boson is given by [**48**]

$$\sigma_{RBW} = \frac{m^2\Gamma_0^2/M_V^2}{(m^2 - M_V^2)^2 + m^4\Gamma_0^2/M_V^2} \tag{2.31}$$

where $s = E_{cm}^2$, M_V and Γ are the mass and width of the boson. Since $M_W \gg$ the mass of any of the decay products the measurement of the W boson mass is not affected by branching fractions or other normalization factors, and they are ignored. The mass distribution of the boson has been obtained by setting $s = m^2$. The Z boson width has been measured at LEP and SLD [**19**]. The W boson width is predicted by the SM, and is found to agree well with the value measured by experiments (such as [**49**]).

As mentioned the parton-level cross-section must be convoluted with the PDFs in order to determine the observed mass spectrum. This is shown here

$$\sigma = \sum_{ij} \int dx_1 dx_2 f_i(x_1, Q^2) f_j(x_2, Q^2) \hat{\sigma}(ij) \tag{2.32}$$

where the sum is over the parton flavors, f_i and f_j are the PDF distributions for the ith flavor in the proton and the jth flavor in the anti-proton and $\hat{\sigma}(ij)$ is the parton-level cross-section. The proton direction is defined to be $+z$ and the energy and momentum of the boson can be written as

$$E_B = \frac{\sqrt{s}}{2}(x_1 + x_2) \tag{2.33}$$

$$P_l = \frac{\sqrt{s}}{2}(x_1 - x_2) \tag{2.34}$$

where $\sqrt{s} = 1.96$ TeV is the center of mass energy of the $p\bar{p}$ collision. x_1 and x_2 are defined in 2.38. It is useful to recall that the rapidity of a particle is defined as

$$y \equiv \frac{1}{2} \ln \left(\frac{E + P_l}{E - P_l} \right). \tag{2.35}$$

In the limit where $mc^2 \ll E^2$ the rapidity can be approximated by the pseudorapidity

$$\eta = -\ln \left(\tan \frac{\theta}{2} \right) \tag{2.36}$$

where θ is the polar angle. We use $\hat{s}$ (of the Mandelstam variables), which we recall is

$$\hat{s} = (x_1 p_1 + x_2 p_2)^2 = x_1 x_2 s. \tag{2.37}$$

Finally, if we equate $\hat{s} = m^2$ we can write

$$x_1 = \frac{m}{\sqrt{s}} e^y, \; x_2 = \frac{m}{\sqrt{s}} e^{-y}, \tag{2.38}$$

and it is possible to write the differential distribution of the mass and rapidity explicitly as

$$\frac{d^2\sigma_{\mathrm{LO}}}{dm\ dy} = \sum_{i,j} f_i \left(\frac{m}{\sqrt{s}} e^y, m^2 \right) f_j \left(\frac{m}{\sqrt{s}} e^{-y}, m^2 \right) \times \hat{\sigma}_{RBW}. \tag{2.39}$$

At tree level W and Z bosons are produced through the Drell-Yan diagrams as in figures 2.4 and 2.5, where the only particle in the final state is the boson. Without anything to recoil against the boson is necessarily produced at rest in the $q\bar{q}$ frame. The partons

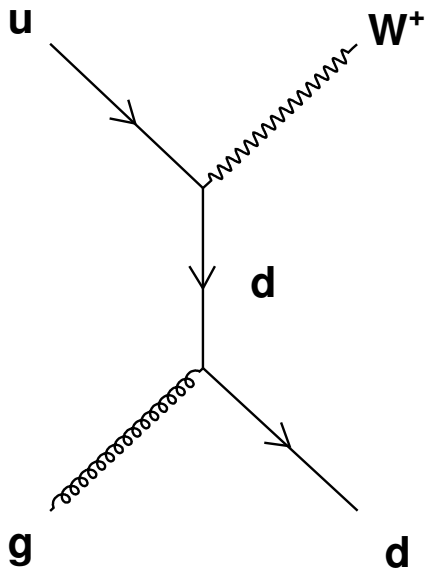


Figure 2.7. W boson production at next to leading order. Here the boson recoils against the gluon, resulting in non-zero boson transverse momentum.

themselves are assumed to have very little momentum transverse to the beam direction. This momentum is referred to as the "primordial" transverse momentum, and comes from the confinement of the parton within the proton. Applying the uncertainty principle this momentum is approximately $\hbar c/R_p \approx 200$ MeV, where R_p is the radius of the proton. Therefore the boson is produced with effectively no p_T. Higher order QCD process involve additional particles in the final state. The most straightforward to consider are the initial state radiation of a gluon (ISR) and the Compton radiation of a gluon (figures 2.7 and 2.8). This additional particle gives the boson something to recoil against. Typically this results in a boson p_T of several GeV, much larger than the "primordial" p_T.

The calculation of the p_T distribution of the bosons is a significant undertaking, the full details of which are beyond the scope of this discussion. However, because of the critical role the description of boson production plays in the prediction of the electron p_T

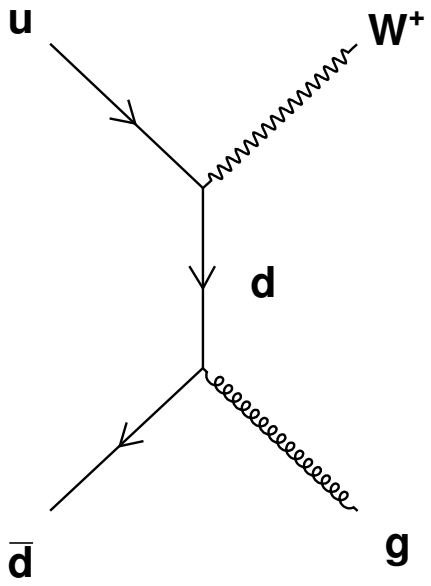


Figure 2.8. W boson production at next to leading order. Here the boson recoils against the gluon, resulting in non-zero boson transverse momentum.

spectrum it is important to examine the critical facets. The differential cross section with respect to the boson transverse momentum is written as

$$\frac{d^2\sigma}{dP_T^2} = \sum_{ij} \int dx_1 dx_2 f_i(x_1) f_j(x_2) \frac{d^2\sigma(ij \to V)}{dP_T^2}. \tag{2.40}$$

For the process $q\bar{q} \to Wg$ shown in figures 2.7 and 2.8 one can accurately calculate the transverse momentum distribution at high p_T ($p_T \approx M_W$) using perturbative QCD. In the low p_T region the results are divergent. A framework was developed by Collins, Soper and Sternman [**50**] to re-sum the perturbation series by group the divergent, non-perturbative terms together. This resummation works for all orders in perturbation theory but requires a correction at low-p_T where non-perturbative physics becomes important. The correction

is parameterized with a function W that smoothly turns off the as the boson p_T increases. The parton level cross section is then

$$\frac{d^2\sigma(q\bar{q}\to V)}{dP_T^2} \sim \int_0^\infty \left[d^2b e^{i\vec{P}_T\cdot\vec{b}} \times W(b,Q)\right] + Y(P_T,Q) \tag{2.41}$$

where Y is the perturbative piece and the impact parameter b is the a conjugate variable of p_T (as b increases p_T decreases). The form of the W function is phenomenologically motivated and is determined by combining data from several experiments. Recently the form

$$W_{NP}(b) = \exp\left(-\left(g_1 + g_2\ln\left(\frac{Q}{2Q_0}\right) + g_1 g_3 \ln(100 x_1 x_2)\right) b^2\right) \tag{2.42}$$

was proposed by Brock, Landry, Nadolsky and Yuan [**51**]. It is found to describe the data well (for example see the DØ Z transverse momentum analysis [**52**]), where the parameters are

$$Q \sim 91\text{GeV},\ Q_0 = 1.6\text{GeV},\ x_{i,j} \sim 0.05 \tag{2.43}$$

and from [**51**]

$$g_1 = 0.21 \pm 0.01\ \text{GeV}^2\ g_2 = 0.68^{+0.01}_{-0.02}\ \text{GeV}^2\ g_3 = -0.60^{+0.05}_{-0.04}. \tag{2.44}$$

In the kinematic region we are interested in the g_2 term dominates.

This completes the description of the boson production model. Once produced W and Z bosons decay almost immediately and we now describe this decay.

2.3. W and Z Decay

W and Z bosons decay into quarks or charged leptons. The branching fraction for boson decay into quarks is nearly ten times that for charged leptons. However, in $p\bar{p}$ collisions it is very difficult to distinguish the signal of quark jets produced by boson decay into quarks from the unrelated jets resulting from the large the total inelastic jet cross section. Additionally, at the luminosities at the Tevatron the analysis is not statistically limited by the number of W bosons collected. Therefore it is convenient to use the very clean signal found in the $W/Z \rightarrow$ leptons channel. Within this channel the bosons decay equally to electrons, muons or taus. The τ decays too quickly to be easily observed and becomes a background for the electron channel decay. DØ has dedicated detectors for both electrons and muons, but because of the DØ calorimeter's superior coverage and energy resolution, along with smaller QED radiative corrections, this analysis is restricted to the electron channel. At leading order this is decay is shown for $Z \rightarrow ee$ and $W \rightarrow e\nu$ in figures 2.5 and 2.4. For a given boson 4-momentum the boson decay properties are completely fixed by the azimuthal angle ϕ and the polar angle θ of the electron. The distribution of the electrons from the W decay as a function of θ is due to the V-A nature of the electroweak interaction, and is given by: ([**53**] is followed in this discussion)

$$\frac{d\sigma}{d\cos\theta} \propto (1 - \lambda Q \cos\theta)^2. \tag{2.45}$$

Q is the charge of the boson and λ depends on its helicity. To leading order the W bosons can be assumed to be produced in either the direction of the proton or the anti-proton, giving them a helicity of ± 1. For example, consider the helicity of a W^- created from an annihilation of a $\bar{u}$ from the anti-proton and a d from the proton. To conserve

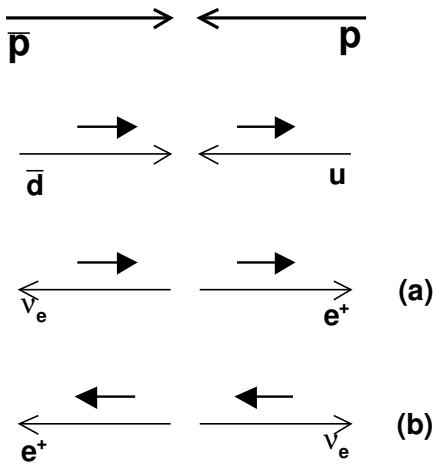


Figure 2.9. In W^+ decay the conservation of angular momentum gives the positron a preferential direction. The top arrows show the direction of the proton and anti-proton. The $\bar{d}$ and u partons collided with spin as indicated by the short arrows. The decay (a) is preferred, with the positron going in the direction of the $\bar{p}$.

angular momentum the electron is produced preferentially in the proton direction (fig. 2.9). However, we know that the W boson $p_T(W) \neq 0$, so its spin is not quite along the z-axis. The decay angular distribution then has a dependence on the boson transverse momentum [**53**]. The angular decay distribution from the neutral Z boson is not purely V-A, and goes as

$$\frac{d\sigma}{d\cos\theta} \propto A(1+\cos^2\theta) + B\cos\theta. \tag{2.46}$$

where A and B are functions which depend on the charge and weak isospin of the decay products and $\sin^2\theta_W$.

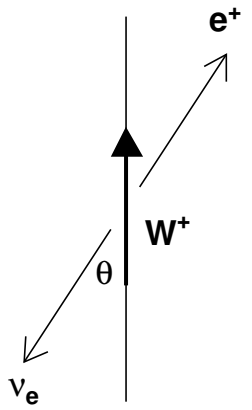


Figure 2.10. The W^+ decay in its rest frame.

2.3.1. Kinematics

If we take the electron and neutrino to be massless then in the boson's rest frame the decay is back-to-back. In the boson's rest frame each particle carries energy equal to 1/2 the boson's mass and in W events 1/2 of the momentum is carried by an unobservable neutrino. This momentum is inferred in the lab frame by balancing the momentum with the electron (and the hadronic recoil) through momentum conservation. In practice it is impossible to balance the full momentum in W events because a significant amount of the longitudinal momentum (along the beam axis) is carried down the beam pipe and not observed. As a result we cannot measure invariant mass of the W. It is possible to balance the momentum in the transverse plane, and the momentum carried by the neutrino is called the "missing" p_T or the $\not\!\!E_T$. The momentum carried by the electron $p_e = 1/2M_W$. We can define the transverse momentum of the electron as $1/2M_W \sin\theta = p_T(e)$, where the θ is the polar angle of the electron (fig. 2.10). The distribution of W events as a

function of the electron transverse momentum is then

$$\frac{d\sigma}{dp_{eT}} = \frac{d\sigma}{d\cos\theta}\frac{d\cos\theta}{dp_{eT}} = \frac{d\sigma}{d\cos\theta}\left(\frac{2p_{eT}}{M_W}\right)\left(M_W^2/4 - p_{eT}^2\right). \tag{2.47}$$

The last term describes the Jacobian peak at $M_W/2$ and by measuring the location of this peak we measure M_W. It is important to note the $\frac{d\sigma}{d\cos\theta}$ term. As we noted above this term adds a dependence to the p_{W_T} of the boson which "smears" the peak. The sensitivity to the boson p_T can be decreased by defining the transverse mass [**6**]

$$\begin{aligned} M_T^2 &= 2(E_T(e) + E_T(\nu) - \vec{p}_T(e)\cdot\vec{p}_T(\nu)) \\ &= 2p_T(e)p_T(\nu)(1-\cos\Delta\phi) \end{aligned} \tag{2.48}$$

where $\Delta\phi$ is the opening angle between the electron and neutrino in the transverse plane. The transverse mass is analogous to the full invariant mass, which is explicitly

$$\begin{aligned} M_{inv}^2 &= (p^\mu(e) + p^\mu(\nu))\cdot(p_\mu(e) + p_\mu(\nu)) \\ &= 2E_T(e)E)_T(\nu)(1-\cos\Delta\phi_3) \end{aligned} \tag{2.49}$$

where $\Delta\phi_3$ is the 3D angle. The M_T is sensitive to our ability to measure p_{ν_T}, which results in a significant smearing due to the detector resolution. In practice there is a trade off between a sensitivity to the theoretical description of the boson p_T and the detector resolution in the p_{eT} and M_T distributions respectively. This can be seen in the Monte Carlo pseudo-experiments done with a Run 1-like DØ parametrization in figures 2.11 and 2.12.

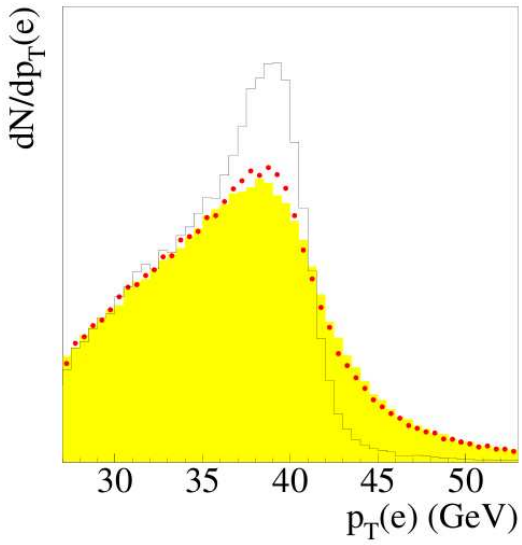


Figure 2.11. A simulated electron transverse momentum distribution. In the black histogram the boson has no transverse momentum while the red histogram has a realistic boson p_T distribution. The yellow histogram shows how the detector smearing affects the distribution. In this case the additional of a realistic boson p_T has the largest effect, while the electron is relatively insensitive to the detector smearing [**49**].

2.3.2. QED Effects

The particles involved in the production and decay of the W boson are electrically charged and can radiate photons. Calculations describing this QED process have been done to leading order in α_{EM}(for example by U. Baur et. al [**54**]). The quarks or the W boson itself can emit a photon, as shown in figures 2.13, 2.14, and photon emission by the electron is shown in figure 2.15. The radiation of the photon by the quark is referred to as initial state radiation (ISR) with radiation by a lepton is final state radiation (FSR). Additionally these processes may interfere with one another.

The largest effect of the QED radiation on the W mass measurement results from FSR. The photon radiated by the electron may carry away a significant portion of the electron's

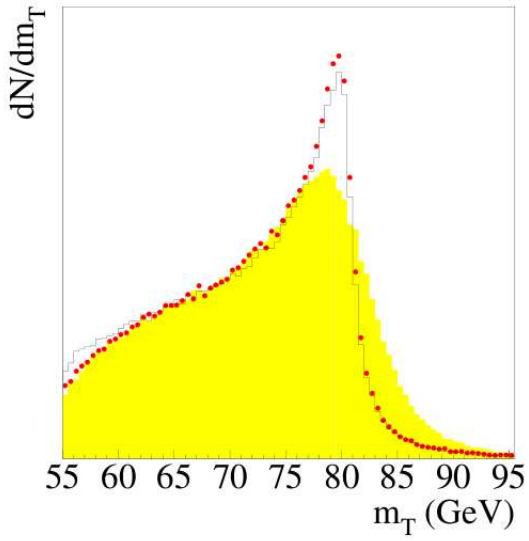


Figure 2.12. A simulated transverse mass distribution. In the black histogram the boson has no transverse momentum while the red histogram has a realistic boson p_T distribution. The yellow histogram shows how the detector smearing affects the distribution. In this case the additional of a realistic boson p_T has a smaller effect, but the detector smearing greatly affects the M_T distribution [**49**].

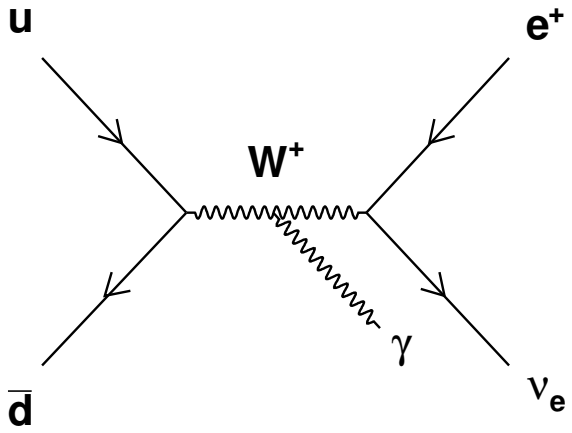


Figure 2.13. The emission of a photon from the W boson.

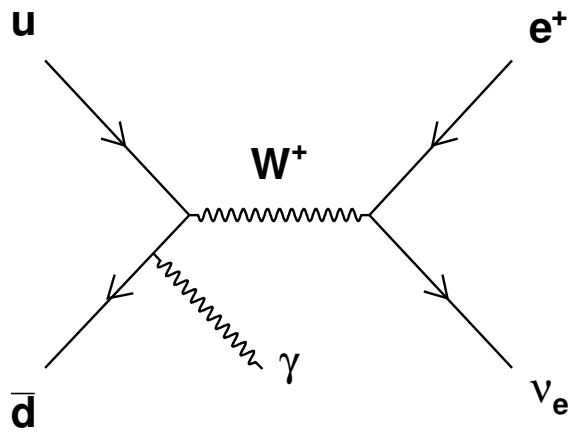


Figure 2.14. The emission of a photon from one of the quarks.

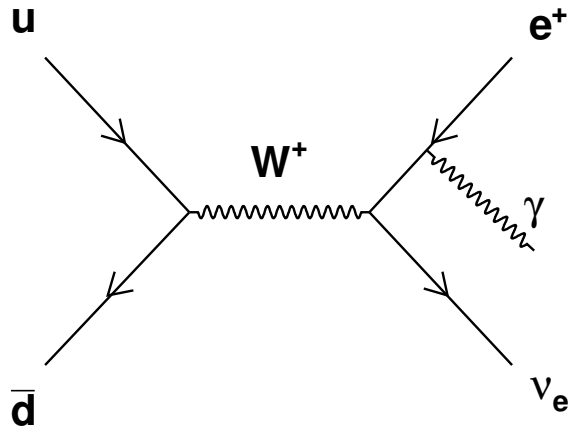


Figure 2.15. The emission of a photon from an electron, called final state radiation (FSR). This photon can be very co-linear with the electron.

energy, distorting the electron p_T spectrum. Most of these photons are emitted within an angular cone of radius ~ 0.3 about the electron. These photons are indistinguishable from the electron (in the DØ detector) and may modify the detectors energy response. It is possible to correct for this. The ISR and interference effect are not found to affect the mass measurement [**55**].

CHAPTER 3

Experimental Apparatus

This measurement was conducted at the DØ experiment at Fermi National Accelerator Laboratory (Fermilab). Fermilab operates the world's highest energy accelerator colliding proton and anti-proton beams at a center of mass energy of 1.96 TeV every 396 ns. The accelerator is actually a collection of seven specialized accelerators chained together and has approximately 200,000 adjustable parameters (figure 3.1). The largest feature in figure 3.1 is the 6.28 km in circumference final accelerator: the Tevatron. Also important in this latest iteration of the acceleration complex is the Main Injector, completed in 1999. This intermediate accelerator allows for higher energy and more frequent collisions than was possible in earlier Tevatron running[1]. In fact, the instantaneous luminosity is now high enough that in many beam crossings there are several hard $p\bar{p}$ collisions, a phenomena referred to as multiple interactions.

In the Tevatron the proton and anti-proton beams are accelerated to 980 GeV and steered around the ring by superconducting magnets. Each beam consists of 36 bunches in three super-bunches of twelve bunches each. The spacing between the bunches is measured in ticks. There are three ticks between each bunch (one tick is 132 ns) and between the super-bunches there are 17 ticks. The bunch structure is shown in figure 3.2. The beams are caused to collide at two points: BØ (the location of the Collider Detector at Fermilab) and at DØ . Quadrupole focusing magnets squeeze the beams into a cross-sectional area

[1]Run 1, from 1992 to 1996

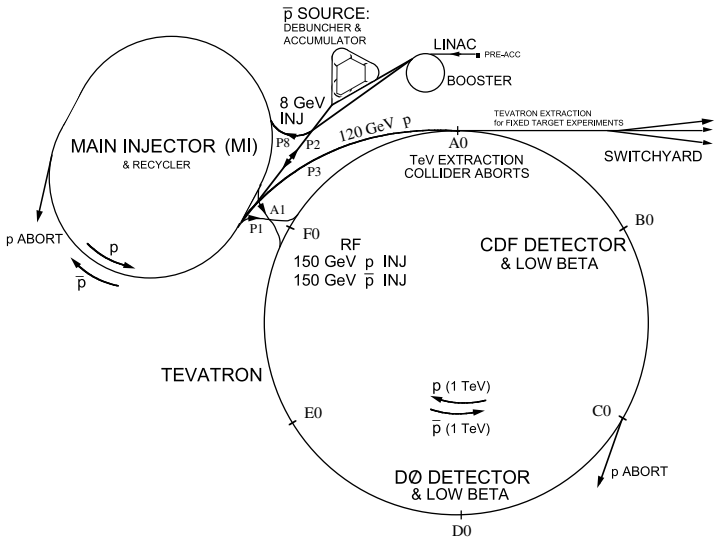


Figure 3.1. The Fermilab chain of accelerators in Batavia, IL. The largest circle represents the Tevatron. At the bottom is the location of the DØ detector.

of 5×10^{-5} cm^2 in the center of each detector. The length of the luminous region is described by the β^* is is approximately 30 cm. Though it is beyond the scope of this thesis to discuss the details of accelerator a detailed reference is [**56**] and [**57**].

3.1. The DØ Experiment

The DØ experiment (figure 3.3) is a multipurpose detector made up of several specialized sub-detectors. Of these, the most important for the measurement of M_W is the calorimeter, which measures the energy deposited by the long lived particles created by the collisions. An overview of the entire detector will be presented, along with a detailed discussion of the calorimeter.

The subsystems of the DØ detector most important for the measurement of M_W are the tracking system and the calorimeter. A short overview of the other systems is given here, but for a more detailed discussion see [**58**]. DØ is shown in figure 3.3. To describe

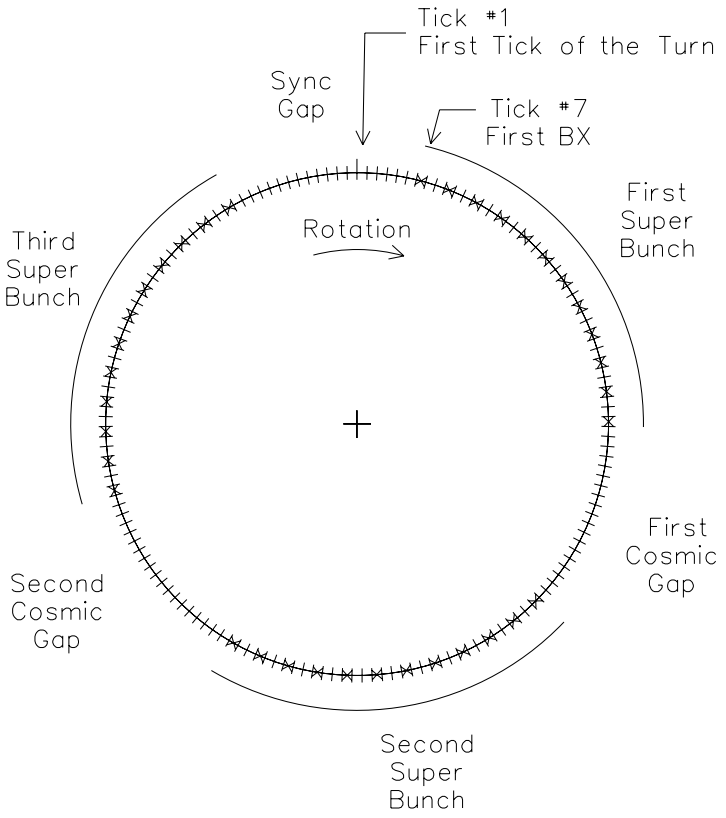


Figure 3.2. The tick structure of the Tevatron beams. Only every third tick is filled with protons or antiprotons, where one tick is 132 ns.

points within the detector we use a coordinate system with its origin at the geometric center of the detector, where the +y direction is up and the +z direction is the direction the protons are traveling. The geometry of the detector lends itself to a cylindrical coordinate system, with ϕ the azimuthal direction, θ the polar angle and r the distance from the z-axis. Two types of pseudorapidity η are defined, the detector pseudorapidity η_{det} and

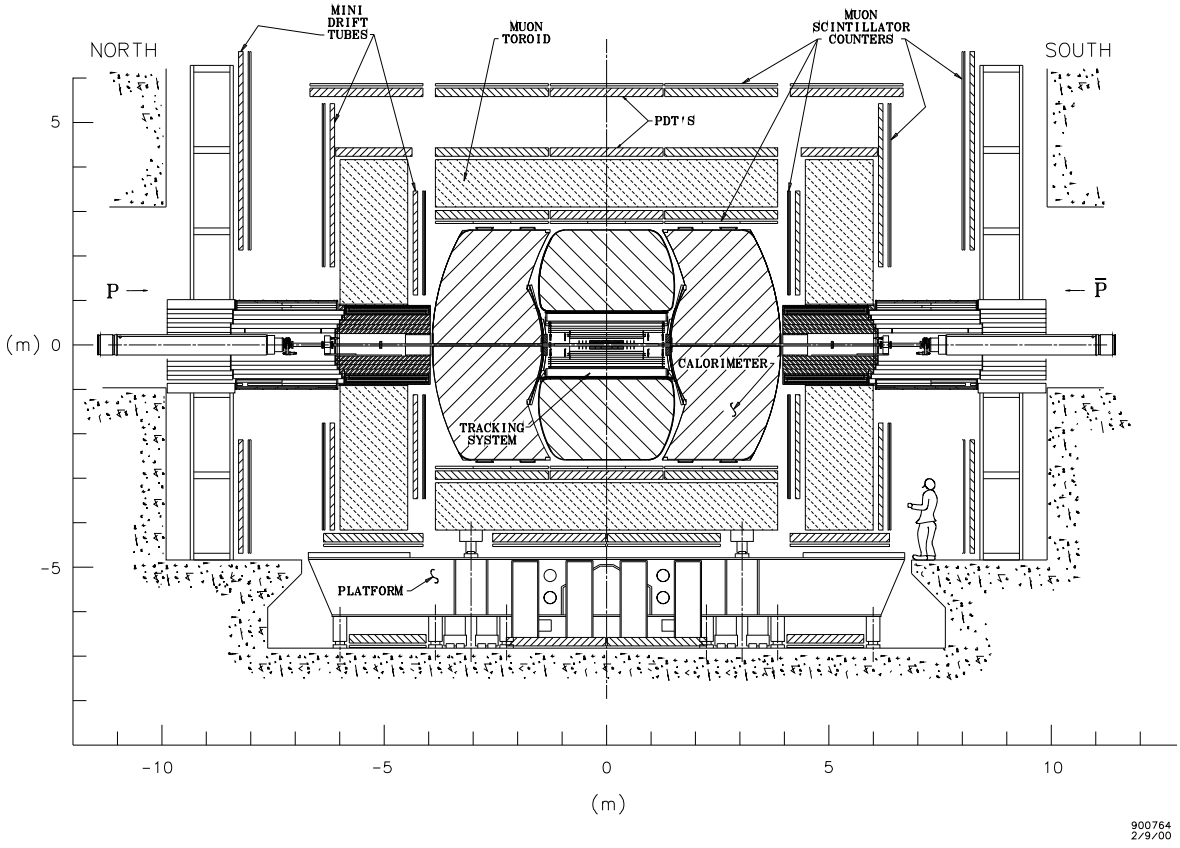


Figure 3.3. A side view of the DØ Detector. The interaction point is at the center.

physics pseudorapidity η_{phys}, where η is generally defined as

$$\eta = -\ln \tan \frac{\theta}{2} \tag{3.1}$$

For η_{det} the angle θ is measured from the origin, and for η_{phys} θ is measured from the vertex of the interaction. This vertex can be displaced along the z axis ± 60 cm making the distinction important.

We will examine the detector sections from the interaction point out. Just outside of the beryllium beam pipe are the tracking detectors. These detectors determine the trajectory of the charged decay particles, as well as the vertex position of the interaction. The tracking system is situated within a 2 T solenoidal magnetic field, which bends the particles with a radius proportional to the particle's p_T. The two tracking detectors can identify the primary vertex of an interaction with a resolution of 35 μm along the z direction. This resolution significantly improves the detectors ability to measure electron p_T and the $\not\!\!E_T$of an event.

In the following sections we follow [**58**] except where otherwise noted.

3.1.1. Tracking

The innermost tracking detector is the Silicon Microstrip Tracker (SMT). Generically, silicon detectors are $p-n$ junction diodes operated at reverse bias [**48**]. A mobile charge free region within an electric field is created in the sensitive region of the silicon. A charged particle ionizes the matter it passes through. This leaves a trail of ions in the sensitive region, which then drift to the substrate, creating a small electrical signal.

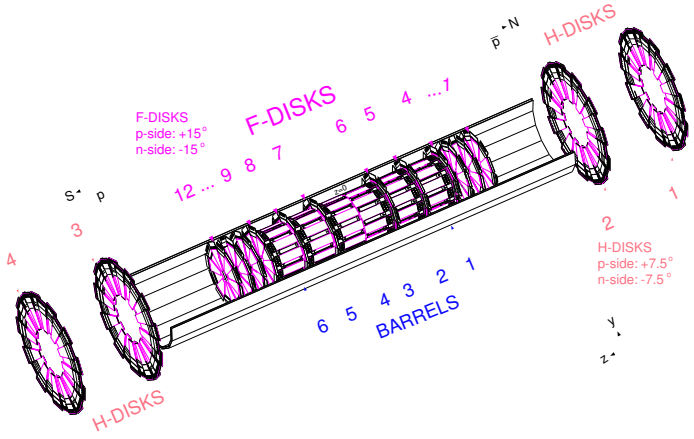


Figure 3.4. The SMT detector.

The large luminous region and the desire to have the detector perpendicular to the tracks motivates the design of the detector. As we see in figure 3.4, the detector is made up of six 12 cm long barrel detectors, combined with disks in the central region, and a collection of disks in the forward (high η) region. The barrels provide a measurement of the $r-\phi$ with a resolution of approximately 10 μm, the disks measure the $r-z$ and $r-\phi$. A barrel consists of four silicon layers arranged at a slight angle to one anther to improve the vertexing and tracking efficiency. Combining the barrels and disks there are approximately 793,000 channels read out.

Outside the SMT is the Central Fiber Tracker (CFT) extending 20 to 52 cm from the beam-pipe and providing full coverage up to $|\eta_{det}| < 1.7$ (figure 3.5). When the charged particles pass through the scintillating material they ionize, creating photons. These photons are guided to a Visible Light Photon Counter (VLPC), which is high-efficiency photodetector. The CFT contains 76,800 scintillating fibers grouped into doublet layers. For each layer oriented along the beam axis there is another at stereo angles of $\pm 3^o$. This allows for 3D track reconstruction, with a resolution of $\sim 100\mu$m.

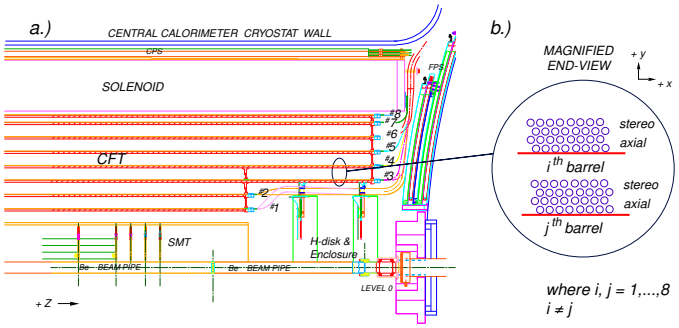


Figure 3.5. The CFT detector.

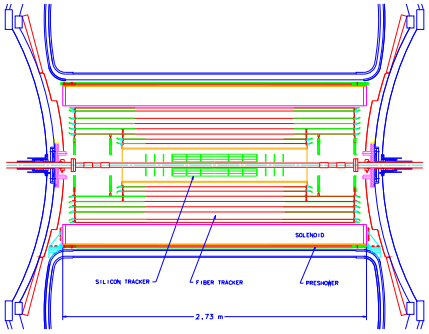


Figure 3.6. Overview of the innermost subsystems.

3.1.2. Solenoid and Preshower

The solenoid magnet is located just outside the tracking volume (figure 3.6). It is a 2 T superconducting magnet operating at 4 K. The magnet is 2.7 m long and has an outer diameter of 1.4 m, with a thickness, measured in radiation lengths (denoted X_0) of ~ 0.9 at normal incidence. This is followed by a preshower detector.

The preshower detector was designed to help identify electrons and photons in triggering and reconstruction. It combines the features of a tracking detector and a calorimeter, and can be used to spatially match the tracks and the calorimeter showers. The central preshower detector (CPS) covers the region $|\eta_{det}| < 1.3$ while the forward detectors (FPS)

covers $1.5 < |\eta_{det}| < 2.5$. The CPS uses three layers of triangular scintillator strips with an axial u-v geometry, where the stereo angles are $\pm 22.5^o$. In front of the strips is a lead radiator which at normal incidence is 1 X_0 thick (the combined solenoid+CPS is 2 X_0 thick at normal incidence to 4 X_0 thick for higher angles). Electromagnetic particles will shower in the radiator, while particles such as muons or charged pions will only ionize in the scintillator. The solenoid and preshower detectors are significant additions to the Run I detector design [**59**] for the Run II DØ upgrade. However, because the of the high instantaneous luminosities, the preshower detector electronics were saturated for the period of data taking covered in this analysis, rendering it useless for this thesis.

3.1.3. Calorimeter

The calorimeter is the most important subdetector for the measurement of M_W. A calorimeter is used to collect and measure the energy of particles. In this sense calorimetry is a destructive measurement, as the particles measured are "absorbed" by the device. DØ consists of three cylindrical Ur-LAr sampling calorimeters of approximately the same size, as shown in figure 3.7. One is centered on the interaction region (the Central Calorimeter or CC) and the other two are mirror images in the forward region (the North and South End Caps or EC). This combination of three calorimeters provides nearly hermetic coverage up to $\eta_{det} < 4$. Additionally, the calorimeter is split into two systems optimized for measuring the energy of two types of particles: the Electromagnetic (EM) Calorimeter and the Hadronic (HAD) Calorimeter. The longitudinal development of electromagnetic showers scales with X_0, the radiation length, while for hadronic showers the scaling goes as λ, the nuclear interaction length. In uranium the interaction length is more than

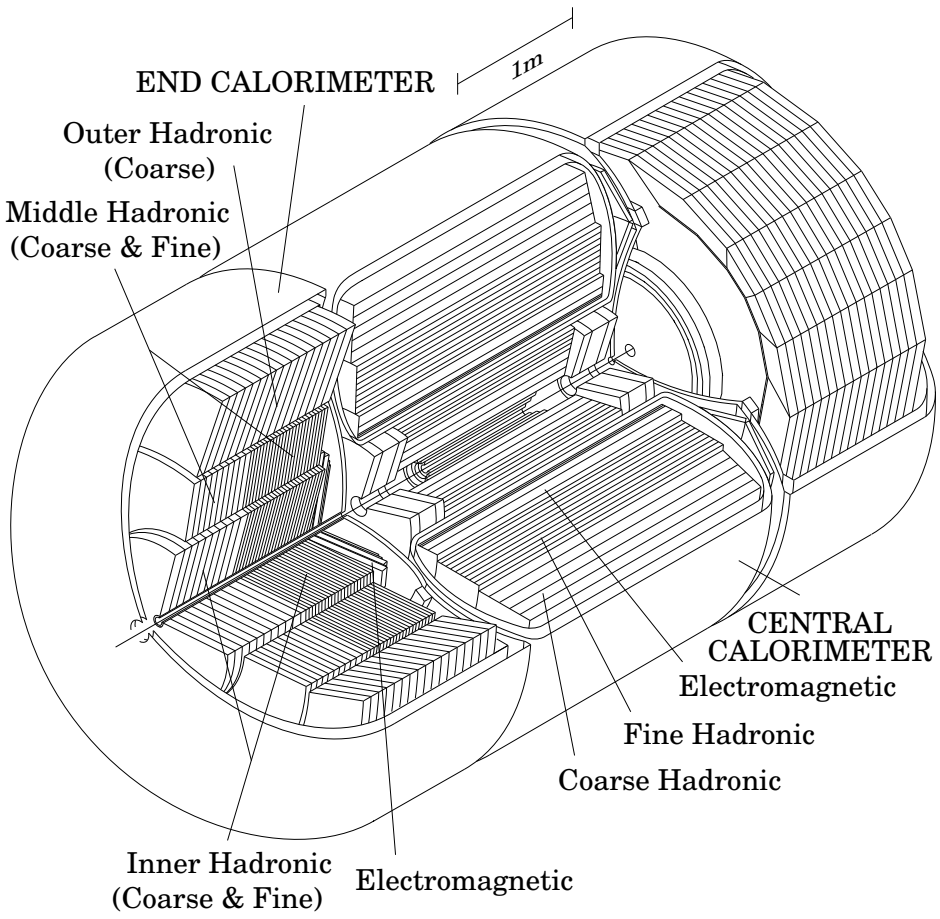


Figure 3.7. A cutaway view of the Central and End Cap Calorimeters.

30 times the radiation length and therefore electromagnetic showers deposit their energy much earlier than the hadronic showers. As a result the EM Calorimeter is situated before the Hadronic calorimeter. In the measurement of M_W with the electron p_T spectrum the calibration of the EM Calorimeter is most critical.

3.1.3.1. Calorimetry Basics. In order to cause a particle to deposit all of its energy in the calorimeter a dense material is needed to increase the likelihood of interaction. The interaction causes the particle to shower. In a particle shower, for example in the

case of electrons, the initial high energy electron decays into a sequence of lower energy photons and electrons. It is difficult to instrument a very dense, continuous material, so a compromise is made in which dense layers, causing the shower, are interspersed with active regions, in our case Liquid Argon cells, to collect and measure the charge deposited by the charged particles. In this way we *sample* a part of the shower. The fraction of the shower we actually sample is subject to statistical fluctuations, which is described by a contribution to energy resolution.

High energy electron and photon showers are the result of the phenomena of pair production and bremsstrahlung. (This discussion follows [**60**], [**61**] and the review of particle detectors in [**48**]. A most extensive overview of calorimetry in high energy physics is found in [**62**].) An electron with energy E_0 (where E_0 is many GeV) produced by, for example the decay of a W or Z boson, will radiate photons through bremsstrahlung. The high energy photons will then convert into electron pairs, which will in turn radiate more photons. In this way the number of particles increases exponentially with the depth of the shower. In the simplest case, we say that the initial electron traversed one radiation length and produced one bremsstrahlung photon with energy $E_0/2$. In the second radiation length the photon produces two electrons, each with energy $E_0/4$, while the initial electron again radiates a photon, now also with energy $E_0/4$. This continues until the particles' energy is reduced to a critical energy E_c (approximately 100 MeV) where ionization loses become important and the shower stops. In this simple model after n radiation lengths there are 2^n particles, with energy $E_0/2^n$. It follows directly that the

shower reaches the maximum number of particles after n_{max} radiation lengths:

$$n_{max} = \frac{\ln(E_0/E_c)}{\ln 2} \tag{3.2}$$

where n is the number of radiation lengths (X_0), and the number of particles at the maximum is $N_{max} = E_0/E_c$. Typically X_0 depends on the density of the material the electron is traversing and is approximately

$$X_0 = \frac{180A}{Z^2}\text{g/cm}^2. \tag{3.3}$$

In more complete models the general features remain the same: the shower maximum increases logarithmically with the energy of the initial electron, and the number of particles in the shower at the maximum is proportional to E_0. This brings us to one of the advantages of using a calorimeter over a tracking system to measure the energy. For a particle with energy E_0 the size of the calorimeter needed scales like $\ln E_0$, whereas tracking systems reliant on the particles deflection in a magnetic field scale as $\sqrt{E_0}$.

The fractional energy resolution of a sampling calorimeter is generally proportional to $\Delta E/E \propto E^{-1/2}$. This is the result of fluctuations of the order $\sqrt{N}$ in the N particles sampled.

The lateral development of the shower is caused by the Coulomb scattering. The Moliere radius is the radial spread of the particle and depends on the X_0 of a material and the angular deflection per radiation length at the critical energy. The Moliere radius is an important consideration when determining the segmentation of the calorimeter.

3.1.3.2. Calorimeter Calibration. The cell level configuration is shown in figure 3.8. There are the 47,032 cells that make up the calorimeter. In the EM CC each module

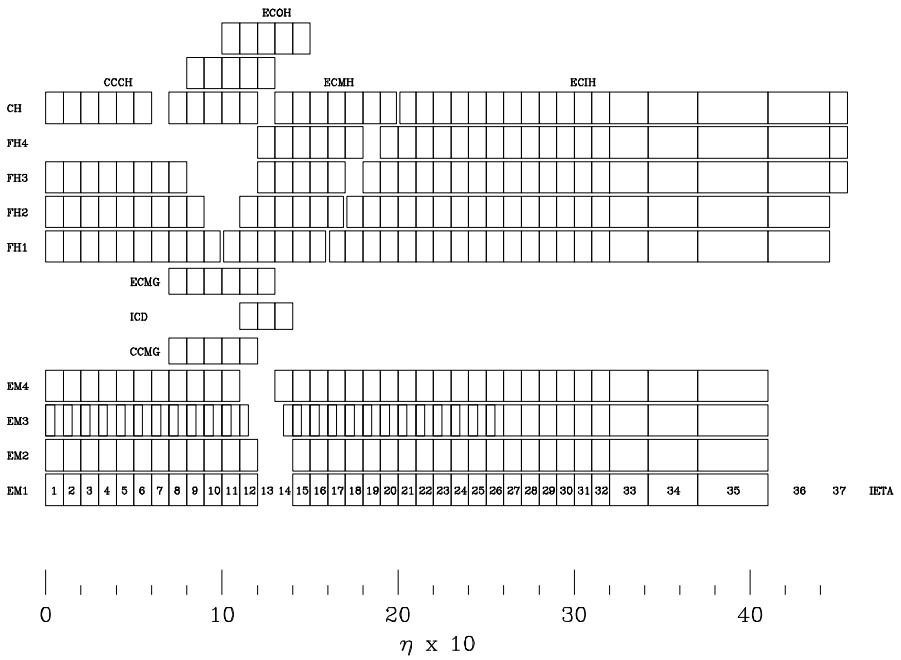


Figure 3.8. Cell-level view of calorimeter.

consists of two cells, each with a depleted uranium absorber plate and an electronic signal board surrounded by liquid argon (figure 3.10). The calorimeter is made up of layers, the first four making up the EM calorimeter, the next three forming the fine hadronic calorimeter (FH) and the last two forming the coarse hadronic (CH) calorimeter as seen in figure 3.9. In the EM layers the cells are formed into nearly projective towers in η_{det} (however the cell boundaries are perpendicular to the absorber plates). The cells are 0.1×0.1 wide in $\eta_{det} \times \phi$, except in the third layer where they are 0.05×0.05. This third layer was designed to be the location of the shower maximum and is instrumented four times as finely as the other layers.

The energy deposited is first measured and calibrated at the cell level. Cells with less than a certain amount of energy are not read out (this is referred to as zero-suppression).

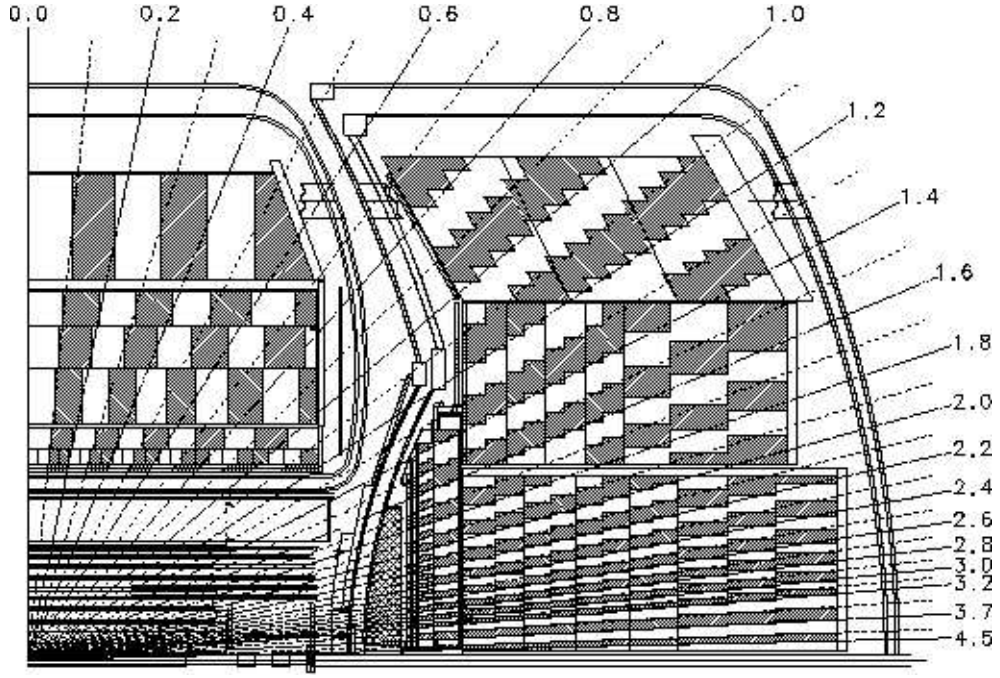


Figure 3.9. A projective view of one quadrant of the calorimeter. The lines are labeled with η_{det}.

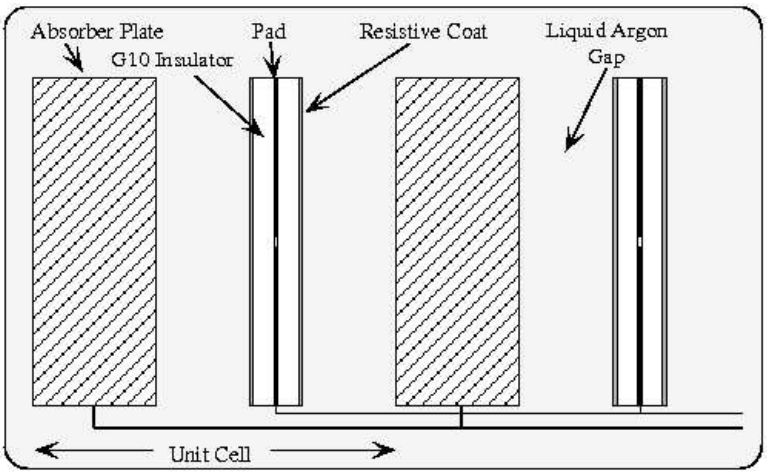


Figure 3.10. One calorimeter module. [**67**]

Pulser and gain calibrations for the readout electronics are applied per cell [**63**], followed by an interphi calibration using "minimum bias" events which deposited at least $E_T > 10$ GeV in the EM calorimeter [**63**]. These calibrated cells are then clustered by the DØ event reconstruction algorithm into EM physics objects. An electron is identified using the simple cone clustering algorithm. This algorithm uses a cone of radius $\Delta R = \sqrt{(\Delta\eta)^2 + (\Delta\phi)^2} < 0.2$, initiated by seeds of $E_T > 500$ MeV. The cluster is required to have $E_T > 1.5$ GeV, to have greater than 90% of its energy deposited in the EM calorimeter (vs. the HAD calorimeter), and to be isolated from other events in the calorimeter. With the individual electrons the calorimeter layer weights are determined.

3.1.3.3. Material Corrections. Ideally there is very little material in front of a calorimeter. This is because the energy measurement depends on collecting all of the particle's energy in the calorimeter. If the shower begins before the front of the calorimeter some of the energy will not be measured. The calorimeter used in this measurement unfortunately has a significant amount of material in front (upstream), which was not planned for in the original design of the calorimeter. The calorimeter in the DØ Run II experiment is structurally the same one that was used in the Run I experiment. The Run I design had very little upstream material compared to Run II. In Run II the addition of a solenoidal magnet to enable a momentum measurement using tracking detectors added a large about of material. To compensate for this a preshower detector, necessarily massive, was added. However, the preshower detector was unusable at the time the data in this analysis was collected. Finally, the amount of time between beam crossings at the Tevatron was decreased between Run I and Run II from 3.5 μs to 396 ns. This greatly increased the luminosity, but reduced the signal integration time for the calorimeter electronics.

There is approximately 2-4 X_0 of material in front of the calorimeter, varying with η_{det}. This significant amount of material is found to move the shower maximum from the middle of the third layer to the front of the third layer (figure 3.11). Any material in front of the calorimeter degrades its energy resolution and affects the calibration. The material distribution is known roughly from the detector construction drawings. Additionally, it is possible to determine the amount of material by using the longitudinal segmentation of the calorimeter readout.

The EM CC is separated into four layers. The electronic readout of the calorimeter is segmented by layers so that it is possible to measure the energy deposited in each layer separately. In particular, we look at the energy deposited in each layer as a fraction of the total EM energy deposition (EM fraction). The EM fraction is sensitive to the amount of material in front of the calorimeter. If there is more material, then more particles will begin to shower earlier, or even in front of the detector, so one will observe a higher fraction of the energy being deposited in the first layer. Less material will result in the later layers having more energy.

We use GFLASH, a parameterized shower simulation [**64**], to study the average electron shower development as a function of depth within the calorimeter. In figure 3.11 it is clear that the upstream (or "dead") material absorbs a significant amount of the energy at the beginning of the shower. Contrary to the original design of the calorimeter, the shower maximum is not contained within the third layer. We next examine the shower development as a function of η_{phys}[2]. Figure 3.12 shows the shower development of ten showers, first at normal incidence and then at $\eta_{phys} = 1.0$. The differences between the

[2] η_{phys} depends on the angle of incidence.

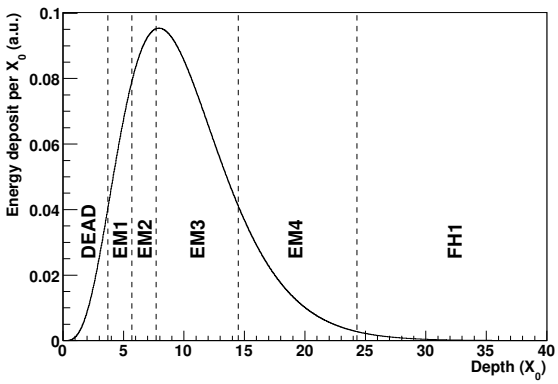


Figure 3.11. Longitudinal shower development for a 45 GeV electron at normal incidence in the DØ detector.

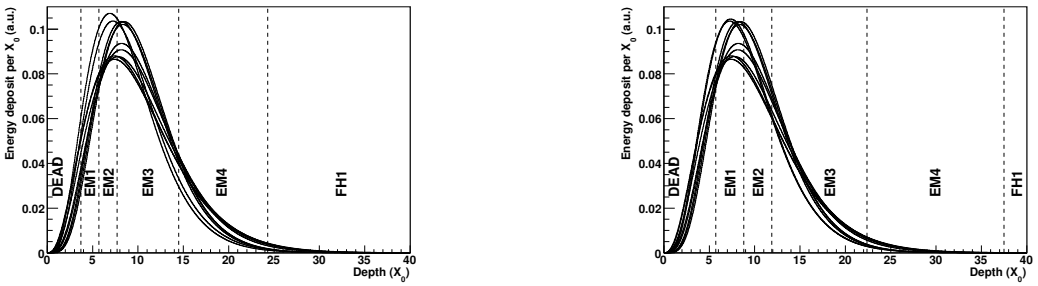


Figure 3.12. Comparing the development of ten 45 GeV electron showers. On right at normal incidence and on left at $\eta_{phys} = 1.0$.

ten curves illustrates the event-by-event fluctuations and change between the sets of ten indicates the overall change in the shower development as a function of η_{phys}. The energy dependence of the shower development is shown in 3.13. Again we see a significant dependence, particularly in the location of the peak. From these simulations we conclude that it is possible to understand the upstream material as a function of both electron energy and η_{phys} by studying the longitudinal shower development.

We cannot change the material in front of the detector *in situ*, threfore it is necessary to measure this with the aid of our Monte Carlo simulation. Single electron Monte Carlo was generated for three different amounts of upstream material and many different electron

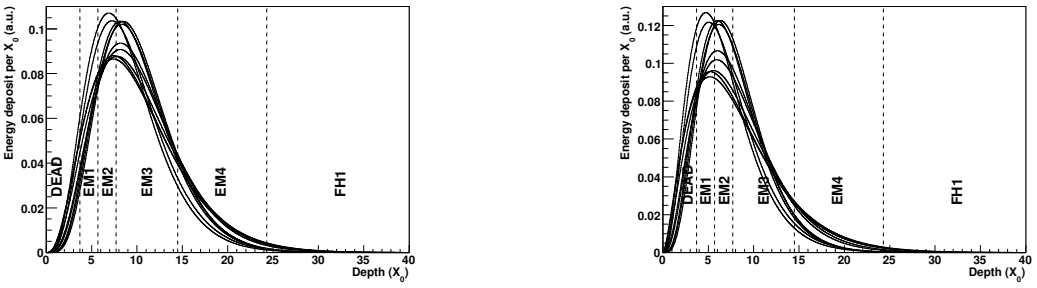


Figure 3.13. Comparing the development of ten 45 GeV electron showers (on right) and ten 3 GeV showers (on left).

energies and angles of incidence (η_{phys}) using the DØ Geant detector simulation [**65**]. The additional material is added uniformly and is described as the difference between the nominal material (from construction drawings) and the simulation and is defined as ΔnX_0. These samples are used to create a parameterized model of the EM fraction as a function of the upstream material (ΔnX_0), energy and η_{phys}. This model is then used in the fast detector simulation and $Z \rightarrow ee$ events are generated. The ratio between data Z events and the parameterized Monte Carlo events of the per layer EM fractions are plotted in figure 3.14 as a function of the combination of the binned η_{phys} categories of both electrons (defined in table 3.1.3.3). The ΔnX_0 is varied and a χ^2 fit is used to determine the best value of X_0 (figure 3.15). Here the χ^2 is defined as the sum of the χ^2 for the individual layer ratios fit to a flat line for each of the three EM layers (the fourth is excluded because very little energy reaches that layer). The result of $\Delta nX_0 = 0.16 \pm 0.01$ is consistent with our knowledge of the detector design. The weights for each layer are applied in the event reconstruction of the data, where the overall weight has been fixed so that the detector has the best energy resolution for 50 GeV electrons.

Category	Electron 1	Electron 2
10	$0.0 < \|\eta_{phys}\| < 0.2$	$0.0 < \|\eta_{phys}\| < 0.2$
11	$0.0 < \|\eta_{phys}\| < 0.2$	$0.2 < \|\eta_{phys}\| < 0.4$
12	$0.0 < \|\eta_{phys}\| < 0.2$	$0.4 < \|\eta_{phys}\| < 0.6$
13	$0.0 < \|\eta_{phys}\| < 0.2$	$0.6 < \|\eta_{phys}\| < 0.8$
14	$0.0 < \|\eta_{phys}\| < 0.2$	$0.8 < \|\eta_{phys}\|$
15	$0.2 < \|\eta_{phys}\| < 0.4$	$0.2 < \|\eta_{phys}\| < 0.4$
16	$0.2 < \|\eta_{phys}\| < 0.4$	$0.4 < \|\eta_{phys}\| < 0.6$
17	$0.2 < \|\eta_{phys}\| < 0.4$	$0.6 < \|\eta_{phys}\| < 0.8$
18	$0.2 < \|\eta_{phys}\| < 0.4$	$0.8 < \|\eta_{phys}\|$
19	$0.4 < \|\eta_{phys}\| < 0.6$	$0.4 < \|\eta_{phys}\| < 0.6$
20	$0.4 < \|\eta_{phys}\| < 0.6$	$0.6 < \|\eta_{phys}\| < 0.8$
21	$0.4 < \|\eta_{phys}\| < 0.6$	$0.8 < \|\eta_{phys}\|$
22	$0.6 < \|\eta_{phys}\| < 0.8$	$0.6 < \|\eta_{phys}\| < 0.8$
23	$0.6 < \|\eta_{phys}\| < 0.8$	$0.8 < \|\eta_{phys}\|$
24	$0.8 < \|\eta_{phys}\|$	$0.8 < \|\eta_{phys}\|$

Table 3.1. The definition of Z event η_{phys} categories. 10 is the most central category while 24 is the most forward.

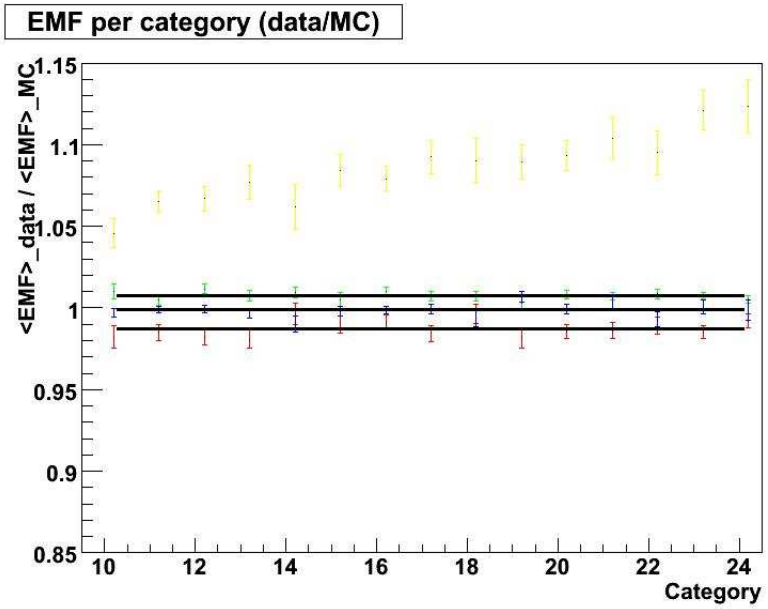


Figure 3.14. EM fraction per category. The categories are a combination of both electron's η_{phys} (see table 3.1.3.3). The yellow points indicate the fourth layer of the EM calorimeter. Little energy is deposited in the fourth layer so it is excluded from the fit.

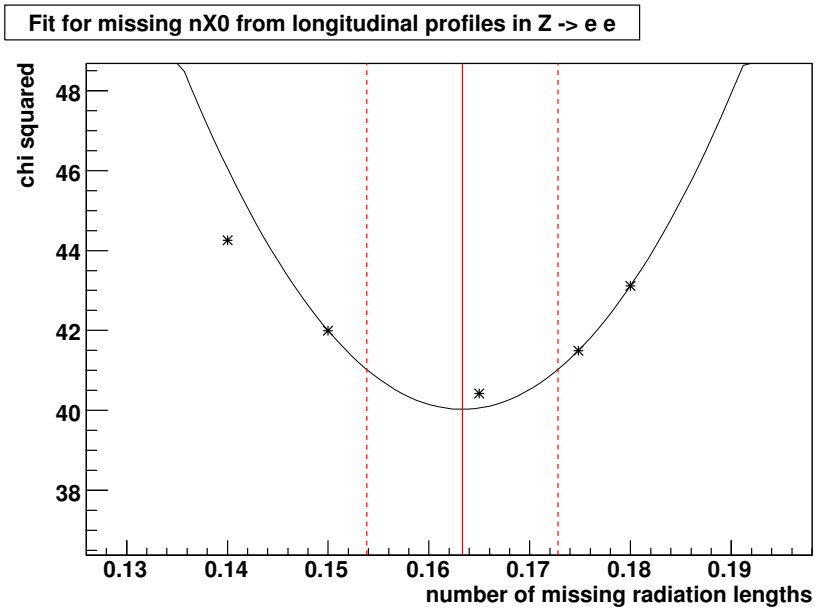


Figure 3.15. Fit for $\Delta n X_0$, where "missing" means material not included in the construction diagrams.

3.1.3.4. Energy Loss. Next it is necessary to account for the actual energy lost due to the zero suppression of the readout and in material in front of the detector. Zero suppression is used to reduce the number of calorimeter cells read out by excluding those cells with little energy, or energy consistent with incoherent noise. However, the underlying event and multiple interactions add energy to the calorimeter isotropically, increasing with the instantaneous luminosity. A faction of this energy is deposited within the electron window, which then reduces the number of zero suppressed cells and artificially increases the observed energy. To account for this effect we again use single electron Monte Carlo samples generated with the Geant simulation of the DØ detector. By comparing the generator level or "true" electron energy with the reconstructed energy after the simulation of zero suppression and the passage through the detector material, a parameterized model

was developed to determine the energy correction as a function of reconstructed energy and η_{phys}. This is also applied in the event reconstruction of the data [**66**].

Finally, multiplicative calibration constants are determined as a function of η_{phys} by fixing the $Z \rightarrow ee$ mass distribution separately in bins of η_{phys} to the LEP determination of the Z mass [**19**].

3.1.3.5. The Hadronic Calorimeter. The above discussion focuses almost exclusively on the EM calorimeter. The calibration of the hadronic calorimeter is less important for the measurement of M_W, and we briefly note that many of the same methods are used (such as the interphi and intereta calibration). A very complete discussion is found in [**94**].

3.1.4. Muon System

As the outermost detector system the muon detector surrounds the calorimeter. Muons are the only particles likely to penetrate the calorimeter. The muon system is a second tracking detector consisting of three layers, with a toroidal magnet between the first and second. The first two layers are proportional drift chambers. These gas filled chambers collect the charge ionized by the passage of a muon. The magnetic field deflects the muon after it has passed the first layer, and the combination of the position measurements in the first and second layer can be used to determine the angle of deflection, and hence the muon p_T. The drift chambers have a position resolution along the z-axis of ~ 1 mm. The third layer is consists of scintillating material arranged in pixels. This improves the measurement of the ϕ position. The muon system is not used directly in this measurement of M_W, but the study of cosmic-ray muons was used in the calibration of the inner tracking

system, which is used to determine the position of the electrons. Though the energy resolution of the muon system is less than that of the calorimeter, it may be possible to use the $W \rightarrow \mu\nu$ channel to measure the W mass in the future.

3.1.5. Luminosity monitor

The luminosity monitor is used to detect inelastic $p\bar{p}$ interactions at DØ . It is two collections of 24 plastic scintillating wedges at $z = \pm 140$ cm from the center of the detector. The 24 wedges are arranged radially around the beam-pipe, as shown in figure 3.16, covering $2.7 < \eta_{det} < 4.4$. PMTs are mounted directly on the wedges to readout the detector. An inelastic interaction has occurred when both the north and south detectors see a signal in time with the tick structure of the beam. The instantaneous luminosity is then determined over approximately one minute. For further details concerning the readout of the luminosity detector see reference [**69**].

In the measurement of M_W the instantaneous luminosity is used in the parametrization of the underlying event. Higher instantaneous luminosity generally corresponds to multiple $p\bar{p}$ interactions, which effects the detection efficiency and energy measurement of electrons, and the calculation of the $\not\!\!E_T$. The measurement of M_W is insensitive to the overall normalization of the distribution, so the integrated luminosity is not used except as a general accounting of the data. This analysis uses ~ 770 pb^{-1} of recorded luminosity.

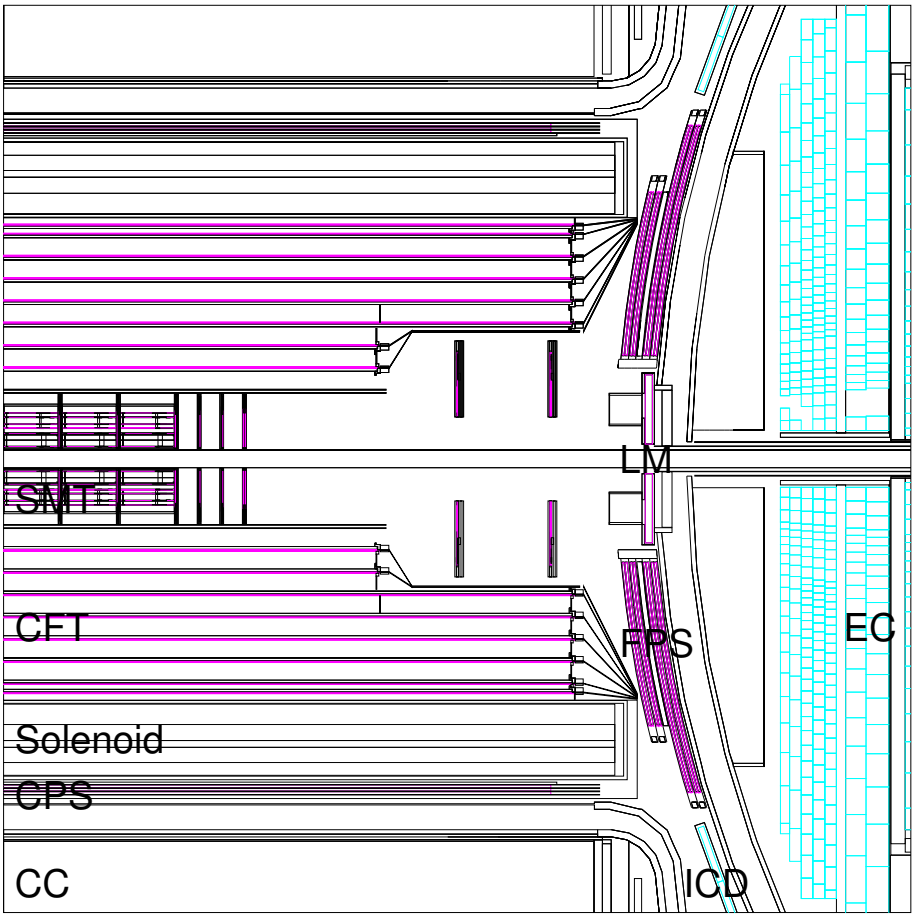


Figure 3.16. The luminosity monitor is located in the far forward region labeled LM and consists of 24 plastic scintillating wedges arranged radially around the beam-pipe.

CHAPTER 4

Data Samples

The data used in this measurement of M_W were collected at the DØ Experiment during Run II of the Tevatron between July 26th, 2002 and February 22nd, 2006. This period is generally referred to as Run IIa in order to distinguish it from the additional data that is still being accumulated. The collection of data is subdivided into runs, each lasting four hours on average. The data were collected between runs 160582 and 215670, for which there was 0.77 fb^{-1} of luminosity recorded at DØ which passed the tight selection criteria for the W mass analysis[1].

4.1. W and Z Selection

This analysis uses the electron decay channel to measure the W mass because of its clean signal with little background. The goal is to obtain a sample of events with a single hard electron that also have large $\not\!\!E_T$, the signature of a neutrino. An additional cut is placed on W boson's transverse momentum, which is observed as a soft hadronic shower from the gluon which the boson recoiled against.

In our detector calibration and simulation tuning we use $Z \rightarrow ee$ events extensively. These events are particularly helpful because all decay products are observable so the Z boson can be completely reconstructed. The electrons from either W or Z bosons are observed and reconstructed through identical paths and have similar spectra. Additionally

[1]The delivered luminosity for this time period was ~ 1.3 fb^{-1}.

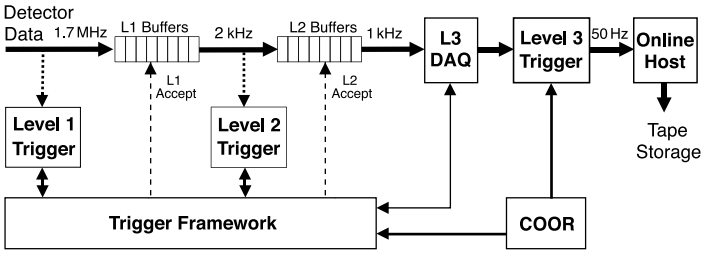


Figure 4.1. A schematic view of the DØ trigger and DAQ.

the transverse momentum distribution of the bosons themselves is very similar, and as a result so are the hadronic recoil systems. Therefore, the goal in collecting Z boson events is to make the detection and reconstruction as similar as possible to the events in the W boson sample.

4.1.1. Online Selection: Triggering

The rate of collisions at DØ, ~ 2.5 MHz, is much to fast to record every event for analysis. As a result a 3-tier trigger system is used to reduce the rate. The first level (L1) consists of hardware trigger elements physically on the detector. Because of time constraints the L1 elements only use signals from a single subdetector. This selection reduces the rate to 2 kHz. The second level (L2) uses a combination of hardware and software elements to reduce the rate to 1 kHz. The final level (L3) is entirely software based and runs on a local farm of CPU's. It utilizes sophisticated algorithms to partially reconstruct each input event. The output rate is 50 Hz which is written to tape and completely reconstructed offline. Figure 4.1 summarizes in a schematic overview the trigger and DAQ system at DØ.

Trigger List Version	L1 Requirements
v8 to v10	one EM trigger tower having $E_T > 10$ GeV
v11	not Cal unsuppressed readout and one EM trigger tower having $E_T > 10$ GeV
v12	Require one calorimeter EM object with $E_T > 11$ GeV and not Calorimeter unsuppressed readout.
v13	One calorimeter EM trigger tower with $E_T > 11$ GeV. Veto on cal_unsuppressed condition.
v14	Calorimeter EM objects with $E_T > 12$ GeV. Veto on cal_unsuppressed condition.

Table 4.1. Level 1 Trigger criteria for electron candidates in $Z \rightarrow ee$ or $W \rightarrow e\nu$.

The trigger scheme used to collect the W and Z boson samples remained consistent throughout Run IIa with only minor changes. In order to make the W and Z samples as similar as possible we only trigger on a single electron (as opposed to a di-electron trigger for Z bosons or an electron plus $\not\!\!E_T$trigger for W bosons). Over the course of Run IIa the instantaneous luminosity increased substantially, and as a result the trigger definitions were slightly tightened to accommodate the increased data taking rate. The different trigger definitions are summarised in tables 4.1, 4.2 and 4.3. In general, at Level 1 we require a single EM calorimeter tower with $p_T > 10$ GeV and at Level 3 an electron with minimal shape requirements and $p_T > 20$ GeV. Shape requirements refer to the characteristic longitudinal distribution of energy in the EM calorimeter from an electron shower.

4.1.2. Offline Reconstruction and Selection

Once an event has been written to tape the full reconstruction takes place offline. The reconstruction software combines the raw detector electronics signals into "physics" objects, such as electrons and the recoil, that are used in the analysis. From the recoil

Trigger List Version	L2 Requirements
v8 to v10	-
v11	One EM candidate with $E_T > 12$ GeV
v12	-
v13	Requires a L2 EM cluster with a threshold ≥ 15 GeV
v14	requires the sum of the two highest EM towers to be ≥ 15 GeV.

Table 4.2. Level 2 Trigger criteria for electron candidates in $Z \rightarrow ee$ or $W \rightarrow e\nu$.

Trigger List Version	L3 Requirements
v8 to v10	$\lvert\eta_d\rvert < 3$ electron is found with $E_T > 20$ GeV meeting loose criteria including a transverse shower shape requirement.
v11	$\lvert\eta_d\rvert < 3$ electron is found with $E_T > 20$ GeV meeting a loose criteria including a transverse shower shape requirement.
v12	Requires an electron satisfying tight shower shape requirements with $E_T > 20.$ GeV
v13	electron found satisfying tight shower shape requirements with $E_T > 22.$ GeV
v14	an electron is found satisfying tight shower shape requirements with $E_T > 25.$ GeV

Table 4.3. Level 3 Trigger criteria for electron candidates in $Z \rightarrow ee$ or $W \rightarrow e\nu$.

and electrons the $\not\!\!E_T$is calculated from the x and y components of the visible transverse momentum:

$$\not\!\!E_x = -p_x^{meas} \text{ and } \not\!\!E_y = -p_y^{meas} \tag{4.1}$$

where p_i^{meas} is the sum of the energy in the unzero-suppressed calorimeter cells (excluding the coarse hadronic calorimeter:

$$\not\!\!E_x = p_{x,y}^{meas} = \sum_{cells} p_{x,y\text{i}}. \tag{4.2}$$

The missing energy is then adjusted for the energy scale corrections to the electrons.

4.1.2.1. Track and Vertex Reconstruction. Hits in the SMT and CFT detectors are used to reconstructed the tracks of charged particles. The track finding algorithm is is first applied to each layer to create track segments, and then the segments are matched to make global tracks. The quality of the track is defined by a χ^2 fit of the track and nearby SMT and CFT hits.

The primary event vertex is the location within the detector where the partons collided. It is found by selecting the global tracks that had at least one hit in the SMT detector and fitting for the vertex position. At least three tracks are required to make a primary vertex and the vertex fitting is done with the different track combinations until the best fit is found. The position of the vertex in the $x-y$ plane is nearly at the origin, in the z direction the position is described by a Gaussian convoluted with a Lorentzian as shown in figure 4.2. Secondary vertexes, caused by the decay of long-lived mesons (such as B, K_S or D), are also found. In this case only two tracks which are not part of the primary vertex are required in the fit. In this analysis of Z and W events secondary vertexes are not used. An overview of tracking at DØ can be found in [**70**], [**71**], [**72**], [**73**], [**74**], [**75**], [**76**], [**77**].

4.1.3. EM Reconstruction

Electron reconstruction begins with the identification of the highest energy cell in the event. This cell is used as the seed of a simple cone clustering algorithm which combines the surrounding cells in groups of calorimeter towers in a cone of $\Delta R = \sqrt{\Delta\eta^2 + \Delta R^2} < 0.3$ centered on the highest energy cell. To distinguish this cluster of EM energy as a true

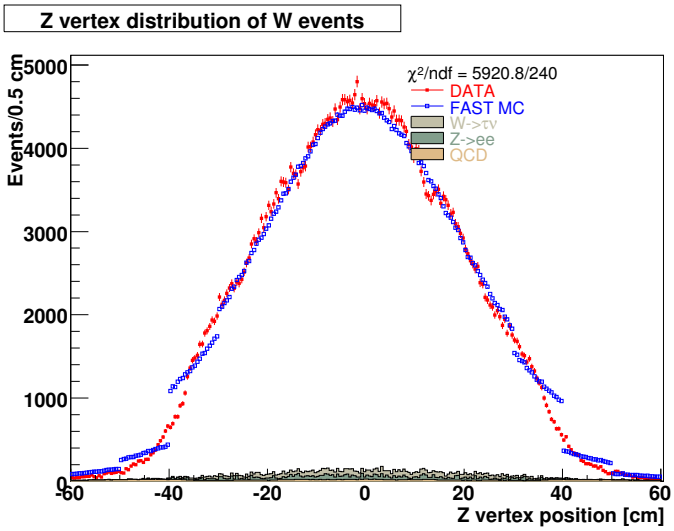


Figure 4.2. The W vertex distribution in data (red) and PMCS (blue). The fast MC prediction is derived from a Gaussian convoluted with a Lorentezian. The "steps" in the predicted distribution are due to the binning of the tracking efficiency.

electron four parameters are useful: the EM Fraction, the isolation, the HMatrix and the track match probability.

4.1.3.1. EM Fraction. A true electron will deposit nearly all of its energy in the EM layers of the calorimeter. Therefore, the fraction $f_{EM} = E_{EM}/E_{tot}$, where E_{EM} is the energy of the cluster deposited in the EM calorimeter and E_{tot} is the total energy deposited, is expected to be large.

4.1.3.2. Isolation. In an electron shower most of the energy is deposited inside a tight cone with little energy around it. We define the isolation of an electron to be

$$f_{iso} = \frac{E_{tot}(R < 0.4) + E_{EM}(R < 0.2)}{E_{EM}(R < 0.2)} \tag{4.3}$$

where if E_{tot} is much large than E_{EM} it is unlikely that the object was a true electron.

4.1.3.3. HMatrix. The shape of an electron shower is well described by Monte Carlo simulations. Therefore it is possible to compare the shape of the EM cluster to that of an electron in Monte Carlo using eight parameters to create a covariance matrix. The inverse of this matrix is used to determine a χ^2 value. This called the HMatrix parameter. The lower the HMatrix parameter, the more electron-like a shower is.

4.1.3.4. Track Match. A track is reconstructed from SMT and CFT hits and is required to have a $p_T > 10$GeV. It is considered to be aligned with an EM cluster, or matched, if it is within 0.05 in η and ϕ. The quality of the match is determined by

$$\chi^2 = \left(\frac{\Delta\phi}{\sigma_\phi}\right)^2 + \left(\frac{\Delta z}{\sigma_z}\right)^2 \tag{4.4}$$

where ϕ and z are found by extrapolating the track to the third EM layer of the matched cluster. The σ_ϕ and σ_z are the measured RMS resolutions of ϕ and z.

4.1.3.5. Recoil Reconstruction. The recoil of the boson is observed in the detector as the jet-like hadronic decay of soft gluons. The hadronic vector $\vec{u}_T$ is made by simply summing the transverse momentum of all the cells in the calorimeter, except the cells that are identified as the electron. The p_T of muons is excluded. Only the transverse component, $\vec{u}_T$, of the hadronic recoil momentum is measured as particles with $\eta_d > 4.0$ escape the calorimeter undetected. All non-zero suppressed cells which are not in the electron cone are summed into the $\vec{u}_T$. As a result the $\vec{u}_T$ includes more than just the effect of the true recoil of the boson, but also effects of multiple interactions, spectator quark interactions and zero suppression.

4.1.3.6. Selection. The selection requirements for electrons are given in table 4.4. This includes the acceptance cuts which restrict the electrons to the fiducial volume of the

EM Cluster Requirements:

- $p_T > 1.5$ GeV,
- EM fraction > 0.9,
- Isolation < 0.2.

Electron Requirements:

- $|\mathrm{ID}| \leq 11$ (*i.e.* we use the simple cone algorithm),
- in fiducial area of calorimeter ,
- EM fraction > 0.90 ,
- isolation < 0.15 ,
- $p_{\mathrm{T}} > 25$ GeV ,
- CC: $|\eta_{\mathrm{det}}| < 1.05$,
- HMx7 < 12 ,
- spatial track match with $P(\chi^2) > 0.01$,

where $|\eta_{\mathrm{det}}|$ is evaluated in EM3.

Z Requirements:

- 2 electrons
- trigger fired
- $p_T(recoil) < 15$ GeV
- 70 GeV $< M_Z <$ 110 GeV

W Requirements:

- 1 electron
- trigger fired
- Missing $E_T > 25$ GeV
- $p_T(recoil) < 15$ GeV
- 50 GeV $< M_T <$ 200 GeV

Table 4.4. Selection criteria for electron candidates in $Z \rightarrow ee$ or $W \rightarrow e\nu$ reconstruction.

CC, in addition to the requirement that the bosons were created with a small transverse momentum.

4.2. W and Z Events

After reconstruction and selection we are left with 17,880 Z boson and 478,669 W boson candidates for the analysis. This represents a significant increase in the amount of data available over previous analyses at the Tevatron.

CHAPTER 5

Simulation and Fitting

In this chapter we first explain the strategy used to fit for the mass using the templates generated with our parameterized MC simulation (PMCS). In the second part the description of the electron energy in the simulation is explicated. The recoil simulation will be discussed in chapter six.

5.1. Fit Method

The W mass is measured indirectly through the electron transverse momentum and the transverse mass distributions because the invariant mass cannot be reconstruction. These distributions cannot be predicted analytically so a Monte Carlo simulation is used to generate the distributions for 100 different mass hypotheses. To determine the mass a negative log likelihood fit is done comparing the high-statistics predictions from the Monte Carlo to the data. In order not to be limited to the 100 template values we interpolate between neighboring Monte Carlo predictions. Statistically it is necessary for the Monte Carlo predictions to contain at least an order of magnitude more events than the data; that is, statistical fluctuations in the Monte Carlo distributions must be negligible when compared to the fluctuations in the data. It is not feasible to simulate the tens of million of events necessary for this with the DØ Geant detector simulation. Therefore, a much faster simulation was developed that parametrizes the most important detector effects.

The speed of the simulation also allows for the study of many different detector scenarios which becomes particularly important in understanding the systematic uncertainty.

The tuning of the electron energy is done in several steps. First we study and parameterize the energy in the electron window that does not come from the electron. This is the underlying event energy and any energy from the recoil that leaked into the electron window. In figure 5.1 we see the generator level electron energy in red. This energy is determined by the event generator and then scaled and smeared by PMCS. The hard recoil is shown in green. We study the contribution of the recoil that is parallel to the electron the full detector simulation and data. The black circle represents the isotropic soft recoil. This is also studied using full detector simulation and data and the amount that is underneath the electron is parameterized and added to the electron. The full detector simulation uses the Pythia [**78**] event generator, discussed below. The complete electron energy parametrization is compared to the Z data. The strategy is to alter the PMCS predictions so that they describe the data as exactly as possible.Then we scale this tuning down the energies of the W boson events. We introduced a linear parametrization of the energy in order to set the Z mass distribution observed in the data to the precisely know mass value. In this case Resbos+Photos is used to generate events [**79**], [**80**], [**51**], [**81**]. To fit for the W mass we again use Resbos+Photos and the tuned PMCS.

In summary, the parameterized Monte Carlo simulation is used to generate $Z \rightarrow ee$ events and $W \rightarrow e\nu$ events. The distributions from $Z \rightarrow ee$ events were tuned to the distributions in the data, and this tuning is scaled down to the W event energies.

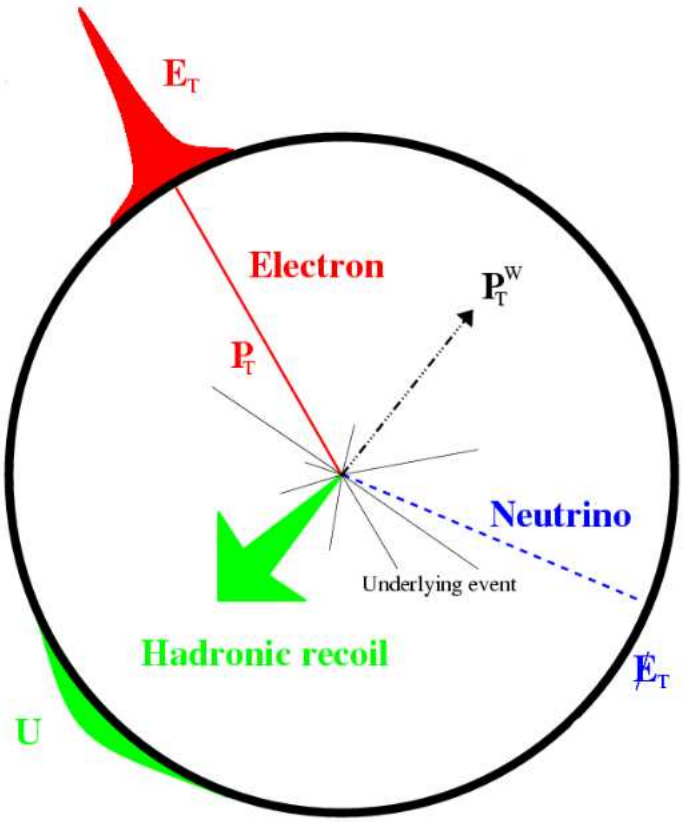


Figure 5.1. A schematic illustration of a W event as simulated in the parameterized MC. In red is the electron energy and green shows the hard recoil. The black circle indicates the isotropic soft recoil. We infer the neutrino momentum after simulating the electron and recoil.

5.2. Event Generation

As input into the fast Monte Carlo simulation two event generators were used: a combination of Resbos and Photos and Pythia [**78**]. Resbos stands for RESummed BOSon production and decay. It computes a fully differential cross section at next-to-leading order (NLO) for the general process $p\bar{p} \rightarrow B(\rightarrow ll)X$, where B is a boson which decays into two leptons l, and X represents the QCD radiation. Photos is added to Resbos to include QED effects such as the radiation of a photon from an electron, or final state

radiation (FSR). The Resbos and Photos combination has proven to be successful in previous analyses from the DØ experiment, notably in the prediction of the Z boson p_T spectrum [**52**]. The Pythia generator is a leading order event generator with parton showering and hadronization. It is used also to generate input for PMCS when we need to compare PMCS to the DØ detector Geant simulation, which also relies on Pythia. Pythia also includes a detailed simulation of the interactions between spectator quarks. These are the remnants of the proton and anti-proton pair that collided but were not part of the hard interaction that produced the boson. These spectator interactions result in energy in the calorimeter that is necessary to model.

The general strategy is to simulate the electron and recoil as observed in the detector and then calculate the $\not\!\!E_T$using equation 5.1.

$$\not\!\!E_T = -\vec{p}_T(e) - \vec{u}_T(recoil) \tag{5.1}$$

Schematically, a typical W event is shown in figure 5.2. A typical $Z \rightarrow ee$ event observed in data is shown in figure 5.3 in the traverse view (looking down the beam-pipe). In red we can clearly see two high p_T electron towers in the calorimeter, both with a matched track (the black lines). A typical $W \rightarrow e\nu$ event is shown in figure 5.4. This is a "lego" view in which we have un-rolled the cylindrical calorimeter onto a flat surface. The red tower is the electron energy observed in the calorimeter, while the yellow tower is the inferred $\not\!\!E_T$. Labeled "16" is part of the hadronic recoil.

Finally, before proceeding to the discussion of the electron energy, we note that the form of the parametrization and the techniques used to derive the parameters were tested first using the DØ detector simulation. The entire analysis was prepared and run treating

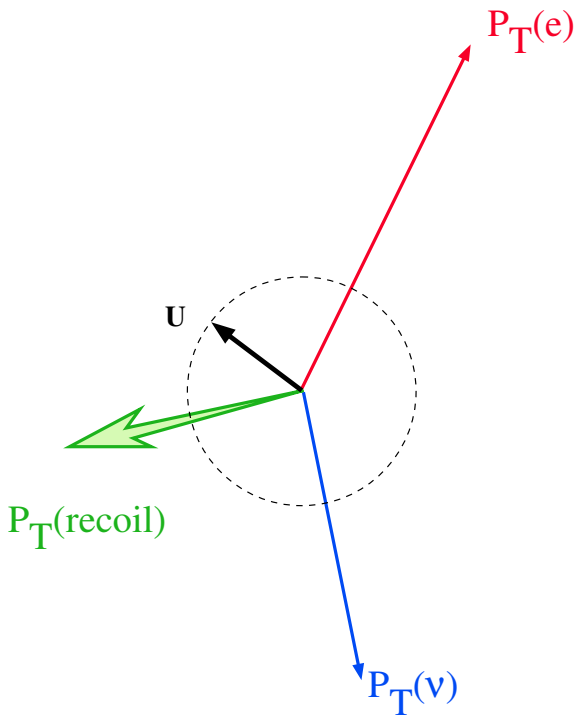


Figure 5.2. A schematic view of the momentum of the particles in a typical W event.

the DØ detector simulation MC as if it were data. Before the result was unblinded it was crucial that the correct mass was found in this "clousre" test of the analysis. In the following sections we focus our discussion on the data parametrization, but a complete second parametrization tuning was done for the closure test as described in [**82**].

5.3. Electron Simulation

All aspects of the measured electron must be described by PMCS. The exact information about the electron the event generator provides must be "smeared" to match the resolution of the detector. Additionally, the detector acceptance and efficiency must be reflected in the final distributions from PMCS. The procedure described below follows the general steps of: combining the electrons with the FSR photons, applying the position

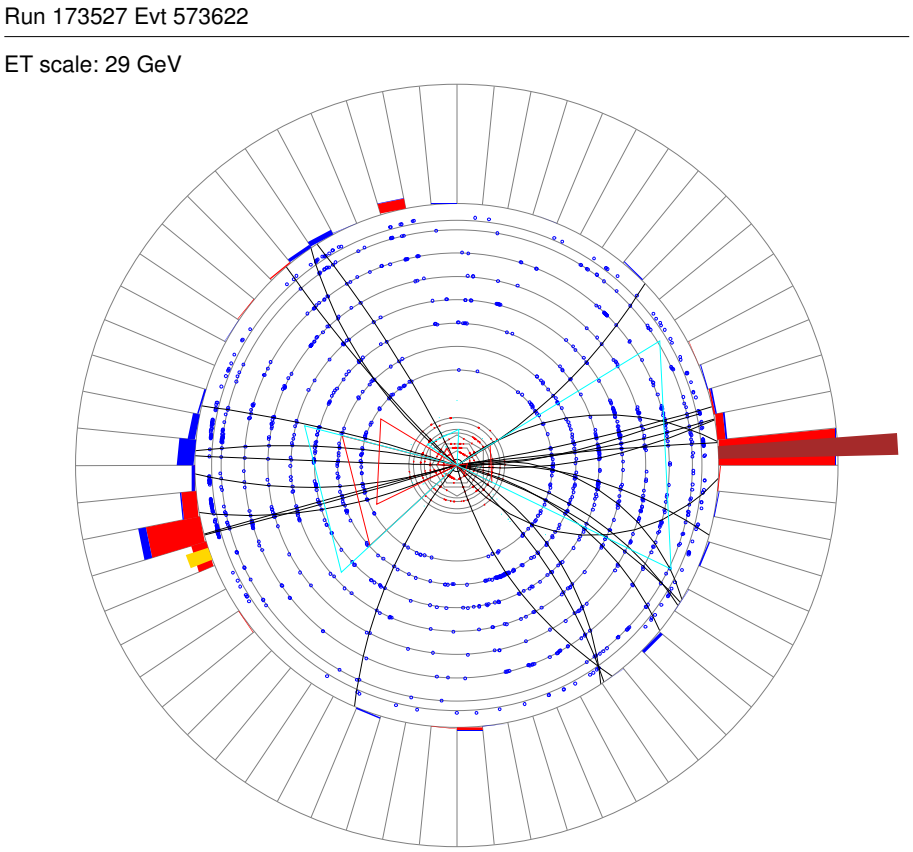


Figure 5.3. A typical $Z \rightarrow ee$ event shown in an end view. The red towers are electrons in the calorimeter, the black lines are tracks, two of which are matched with the electrons.

resolution, correcting the energy, applying the energy resolution, and finally applying the detector efficiency and acceptance.

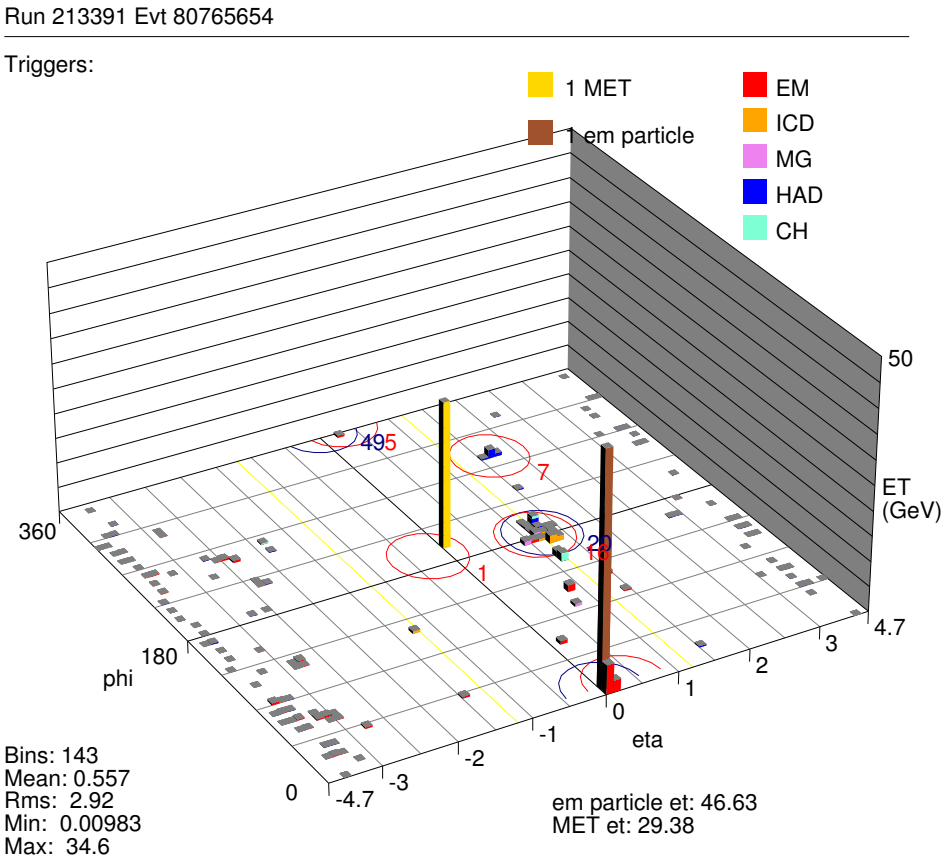


Figure 5.4. A typical $W \rightarrow e\nu$ event, shown in a "lego" view. The red tower is the electron and the yellow tower is the calculated $\not\!\!E_T$.

5.3.1. Electron Photon combination

The first step in the electron simulation is to add the FSR photons to the electron if they are within $\Delta R < 0.30$. In the detector energy from photons closer than this to the electron is indistinguishable from the electron energy. We parameterize the efficiency with which the photon will be seen by the detector as a function of the photon p_T. The

σ	
η_{phys}	0.002
η_{det}	0.007
ϕ_{phys}	0.0004

Table 5.1. The angular resolution of an electron is simulated with a Gaussian function with a mean of zero and the width given by the table.

response of the calorimeter to photons within an electron cone is also parameterized based on the photon p_T and the η_{phys}. These parametrization are determined by studying single photon events in the Geant DØ detector simulation [**55**].

5.3.2. Electron Position Resolution

The position of the electron in the detector is found by using the simulated z vertex of the event and the simulated η_{phys} and ϕ_{phys}, and calculating the η_{det} of the simulated electron at the third EM layer of the calorimeter. The z vertex distribution is simulated by a double Gaussian and the beta function whose parameters were tuned for different run periods and instantaneous luminosity. To simulate ϕ_{det} the bend due to the solenoidal magnetic field that the electron passes through on the way to the calorimeter is calculated. We assume that the 2 T field is uniform and extrapolate the ϕ_{det} at the third EM layer using the charge and p_T of the electron.

The angular resolution for η_{phys}, η_{det} and ϕ_{phys} is simulated with a Gaussian function centered at zero with a width shown in table 5.3.2. The ϕ_{det} resolution is complicated by the "phimod" efficiency and bias. By examining one calorimeter module boundary in detail we can understand the source of the phimod efficiency. Figure 5.5 is a view of a CC EM near the region of a module boundary.

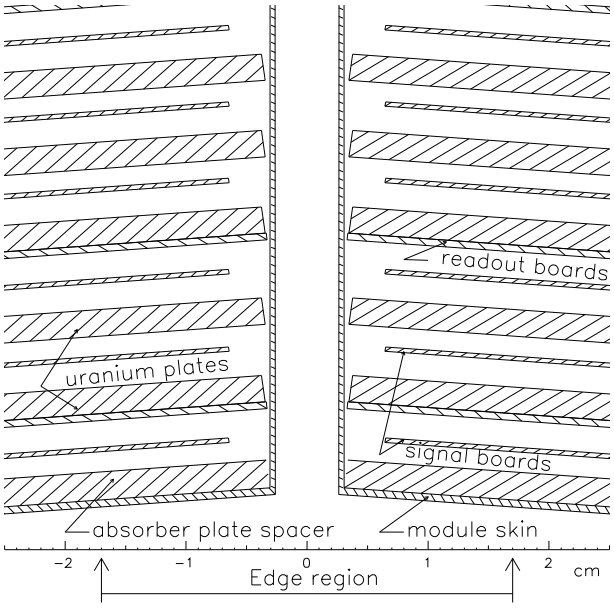


Figure 5.5. The boundary between two EM calorimeter modules. The edge effects here result in ϕ-dependant efficiency within each module.

The positioning of the signal boards, combined with the non-uniform electric field, cause the efficiency of finding an electron to decrease near the edge of the module. This effect is enhanced by the shorter (compared to the original design) signal integration time between collisions with the upgraded Tevatron collider. We measure the efficiency as a function of an electron's ϕ position within a module (phimod) which is defined as

$$\phi_{mod} = \quad \text{mod } 16\phi/\pi. \tag{5.2}$$

In figure 5.6 the efficiency is nearly flat in the central region and drops quickly toward the edges as expected.

Finally, the energy clustering algorithms used to find electrons are found to be biased toward the center of the module. This is studied in data by comparing the ϕ position as determined by the tracking detectors with the position determined by the calorimeter

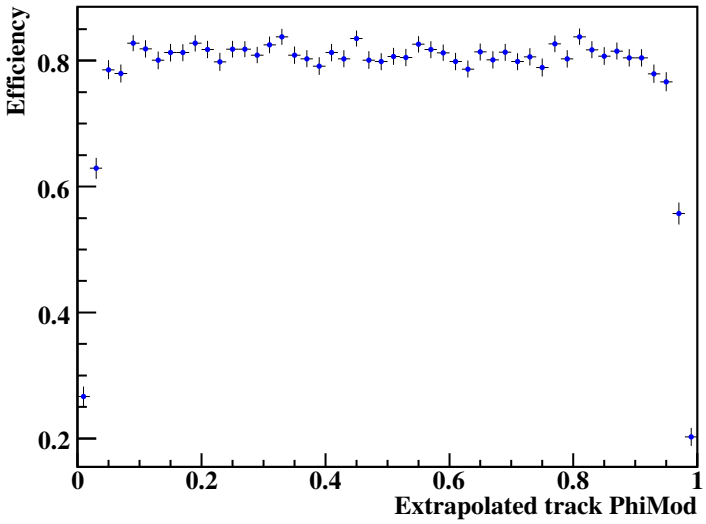


Figure 5.6. Electron efficiency vs ϕ position in detector module.

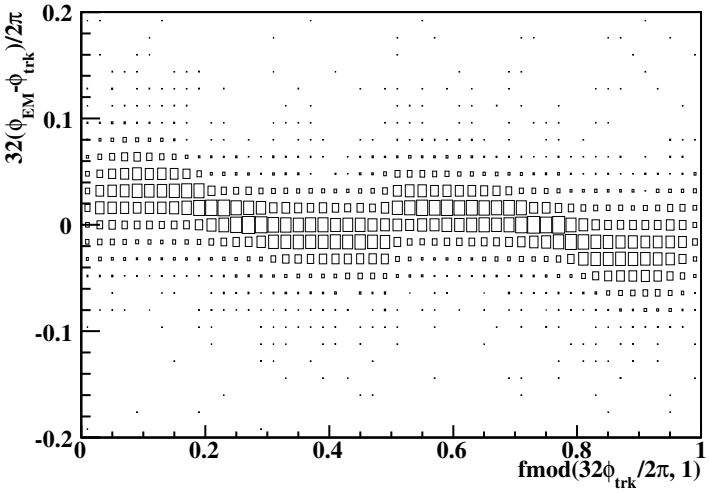


Figure 5.7. Difference between ϕ position from tracking and calorimeter.

energy clustering algorithm (fig. 5.7). In PMCS if the electron has passed the phimod efficiency then the bias is determined by randomly choosing an offset described by the distribution for a particular track ϕ [**83**].

5.3.3. Electron Energy

In the detector the energy within an electron cone is polluted by energy from a variety of other sources. This includes energy from the hard recoil, the underlying event, detector pileup and zero-suppression effects. The electron energy from the event generator is essentially uncorrelated with this additional event energy. In PMCS we apply the following parametrization for the electron energy:

$$E(e) = R_{EM}(E_0) \otimes \sigma_{EM}(E_0) + \Delta E(\mathcal{L}, u_{\parallel}) \tag{5.3}$$

where $R_{EM}(E_0)$ is the response and σ_{EM} the energy resolution of the electromagnetic calorimeter. ΔE is the additional energy within the electron window, and is parametrized as a function of luminosity $\mathcal{L}$ and $u_{\parallel}$. The $u_{\parallel}$ is defined as the amount of energy from the recoil system that is parallel to the electron direction (and figure 5.8):

$$u_{\parallel} = \vec{u}_T \cdot \hat{p}_T(elec). \tag{5.4}$$

The energy response of the EM calorimeter is then modelled using the linear function

$$R_{EM}(E_0) = \alpha \times E_0 + \beta \tag{5.5}$$

where α is the linear response of the calorimeter to electrons, or scale, and β is an offset. The scale and offset are measured using $Z \rightarrow ee$ data after correcting for the additional energy, discussed below.

5.3.3.1. Additional energy. The electron energy correction ΔE primarily consists of four components.

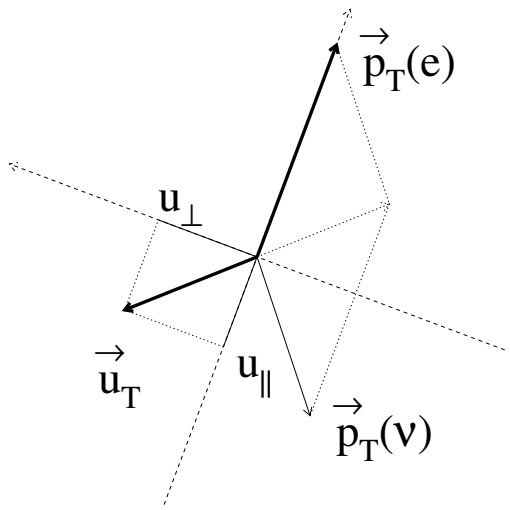


Figure 5.8. The $u_\parallel$ is the recoil energy along the direction of the electron momentum.

- the underlying event which includes the spectator quark interactions, other $p\bar{p}$ interactions, and electronics noise.
- The effect of zero suppression of the calorimeter readout. Cells with energy within 1.5σ of the pedestal level (2.5σ offline) are not included in the readout or reconstruction. As a consequence some the tail of the electron energy distribution is cut off and real energy is lost.
- With an electron cone size in the reconstruction of 0.3 in $\eta \times \phi$ some energy can "leak" out.

It is possible to measure the underlying event contribution with the W events in data. The electron cone size of 0.3 means that there are 13 calorimeter towers in an electron. We rotate away from the actual electron cone in ϕ and measure the energy within a rotated 13 tower cone. To exclude regions where there is hadronic activity we require that the energy in the rotated cone be less than 0.15 times the electron energy. Figure 5.9 shows

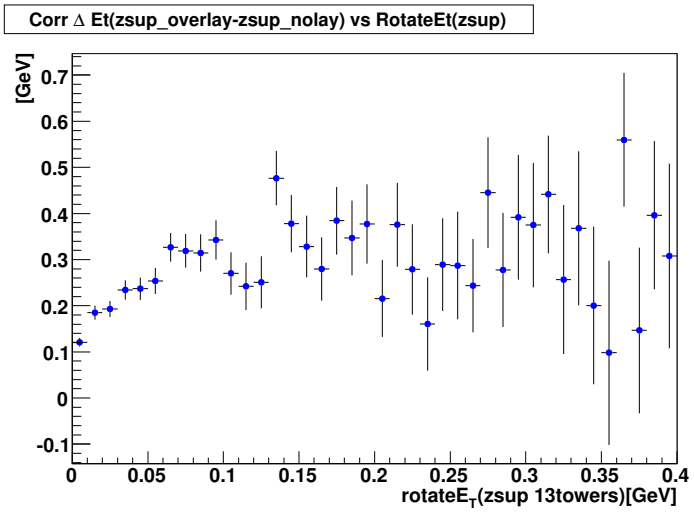


Figure 5.9. Energy in an electron cone rotated away from the true electron window in $W \rightarrow e\nu$ events.

the average energy in a 13 tower window rotated away from the electron cone with an average of 126 MeV [**84**].

This correction depends on the luminosity of the event and $u_{\parallel}$. The luminosity dependence is show in figure 5.10. This strong, linear dependence of 35×10^{31} MeV cm^{-2} s^{-2} is due to additional interactions in the event. Instantaneous luminosity is highly correlated with additional $p\bar{p}$ interactions. The $u_{\parallel}$ dependence is shown in figure 5.11, increasing at high $u_{\parallel}$, where the recoil is more nearly in the same direction as the electron. The data is binned in luminosity and $u_{\parallel}$ and the energy of a rotated cone is measured in each bin. These binned distributions are read by PMCS in the parametrization of the electron energy [**85**].

The correction above is not added directly to the electron energy in PMCS. It has the advantage of being measured in the data, but the energy in a cone rotated away from the electron does not exactly correspond to the additional energy under the electron itself.

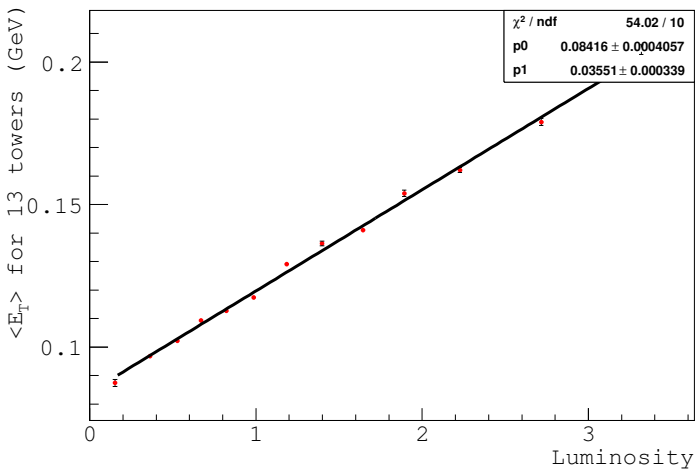


Figure 5.10. Energy in rotated cone as a function of instantaneous luminosity.

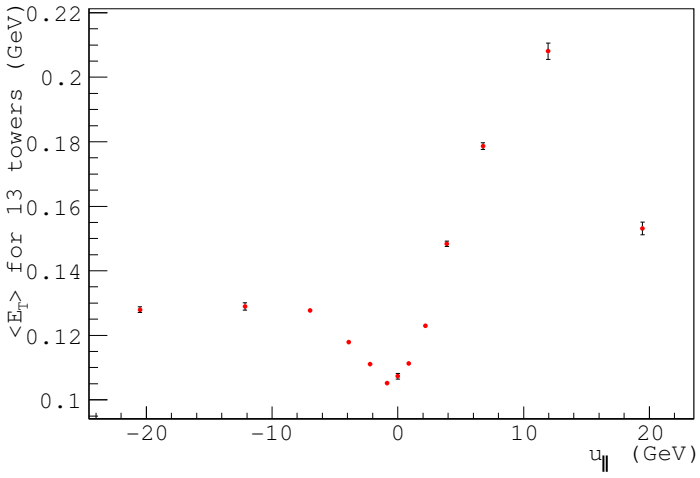


Figure 5.11. Energy in rotated cone as a function of $u_{\parallel}$.

The difference in the energy is due to the zero suppression. The effect of zero suppression has already partially been taken into account. In the calibration of the calorimeter energy loss corrections were determined (see chapter four) with single electron Monte Carlo from the DØ Geant detector simulation. This Monte Carlo does not include a description of

	Sample A [GeV]	Sample B [GeV]	Sample C [GeV]	Sample D [GeV]
E_T^{clus}	38.427	39.085	38.647	39.192
E^{clus}	43.341	44.074	43.576	44.177

Table 5.2. The effect of the underlying event. The values are the averaged reconstructed energies for single energy electrons generated at $E_T = 40$ GeV. Samples A and B do not have the zerobias overlay. Samples C and D have the overlay. Samples A and C have zero suppression applied, while samples B and D do not. Adapted from [**85**].

the energy from the spectator quarks, other $p\bar{p}$ collisions or noise, all of which affect the zero suppression in the data.

It is necessary to account for the partial calibration from the electron reconstruction as well as the additional effects not included there. This is done using three additional samples of single electron Monte Carlo all similar to the one sample used to determine the energy loss correction. The samples, and the effect on the reconstructed energy of a 40 GeV electron, are summarized in table 5.3.3.1. The zero suppression is either applied or not, for samples with or without an underlying event overlay. The difference between the the zero suppressed sample with and without overlay is parameterized as a function of the energy in the rotated cone (and η_{det}), correcting the energy measured in the rotated cone for the observed non-electron energy in the electron cone.

5.3.3.2. Energy Response. The calibration of the calorimeter and the tuning of PMCS by adding in the additional energy ΔE results in a highly accurate description of electron energy to within 1 GeV. To measure the W mass to within a systematic uncertainty of < 50 MeV using the electron p_T distribution additional precision is needed. This is obtained by comparing the Z events in data to the Z mass measured at LEP and determining an energy scale and offset that is applied in PMCS.

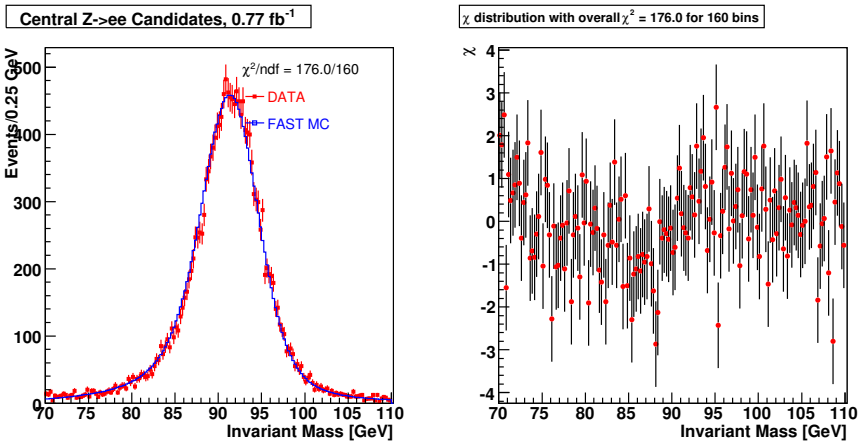


Figure 5.12. The $Z \rightarrow ee$ invariant mass distribution, data (in red) compared to PMCS (blue) after tuning. A fit is done in order to check the validity of the tuning and the mass is found to be $M_Z = 91196 \pm 32$MeV.

The scale and offset cannot be distinguished from one another to the precision required using only the M_Z distribution (Fig. 5.3.3.2). However, the fact that electrons from Z decays are not monochromatic can be exploited as an additional constraint. In the case where the offset $\beta \ll E(e_1) + E(e_2)$, Eqn. 5.5 can be substituted into Eqn. 2.49 and expanded to find:

$$M_{obs.}(Z) = \alpha M_{true}(Z) + \beta f_Z + \mathcal{O}(\beta^2), \tag{5.6}$$

where f_Z is a kinematic variable defined as:

$$f_Z = \frac{E_{true}(e_1) + E_{true}(e_2)}{M_{true}(Z)}(1 - \cos\theta), \tag{5.7}$$

and where $E(e_1)$ and $E(e_2)$ are the observed energies of the the electrons, $M(Z)$ is the Z mass, and θ is the opening angle between the electrons. This relates the observed mass to the scale, offset and the true energies of the electrons. It is then possible to extract

the scale and offset from the M_Z vs. f_Z distribution (Fig 5.13). One can think of f_Z as providing access to the energy spread of the electrons from Z decay.

There are several ways to proceed in determining the scale and offset. The simplest choice would be to fit a linear function to the profile of the M_Z vs. f_Z distribution from the data, binned in f_Z (Fig 5.14). In this case it is useful to think of f_Z as the derivative of the observed mass with respect to β.

$$\partial_\beta M_{obs.}(Z) \approx f_Z \tag{5.8}$$

Unfortunately, this method cannot distinguish between the scale and offset that we are trying to measure and the underlying event and other effects. Just as the underlying event and other effects are measured and simulated independently of the scale and offset, it is necessary to measure the scale and offset independent of other effects. Therefore, the M_Z vs. f_Z distribution is simulated in parameterized MC where all the effects can be separately included. By varying only the scale and offset, generating the M_Z vs. f_Z distribution, and then comparing this to the distribution in data, the confounding influence of the underlying event and other effects is removed.

In order to use all the information in the M_Z vs. f_Z distribution, as opposed to reducing this histogram to the profile, a binned likelihood fit to 2D templates is used. This method is computationally intensive.

A binned negative-log-likelihood method was used to find the best values of the parameters. The negative-log-likelihood is defined as follows:

$$\mathcal{L}(\alpha, \beta) = -\sum_i (D_i \log[N_i(\alpha, \beta)] - N_i(\alpha, \beta)) \tag{5.9}$$

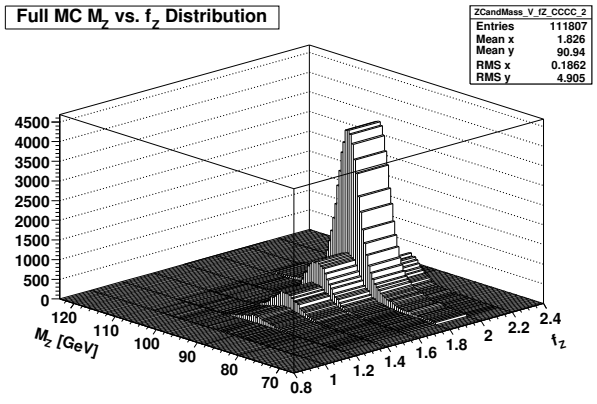


Figure 5.13. An example of the f_Z vs. M_Z distribution.

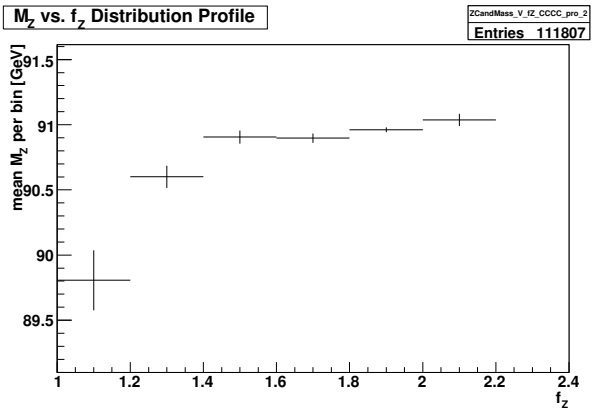


Figure 5.14. The profile of the f_Z vs. M_Z distribution.

where the sum is over all bins i and D_i and N_i are the bin values in the data and MC distributions respectively. Minuit [**68**] provides the minimization within the DØ wzfitter program [**87**].

To ensure this fitting technique is not biased, eight hundred PMCS experiments were generated with randomly chosen (within the template range) scales and offsets. These pseudo-experiments were generated to simulate the $\sim$ 1 fb^{-1} sample. The PMCS templates were generated in α from 0.990 to 1.010 and -1.0 GeV to 1.0 GeV in β. The event selection was chosen to match the selection in data (as described in table 4.4). Recall the most important requirements are two electrons which have $p_T(e) > 25.0$ GeV, p_T(recoil) < 15.0 GeV and both electrons in the central calorimeter ($|\eta| < 1.05$) with a good spatial track match. The template distributions contained approximately fifty million events. The fit was done for each pseudo-experiment and the resulting parameters were compared to the true parameters by plotting the pull distributions. The pull is defined as:

$$P = \frac{X_{true} - X_{fit}}{\sigma_{fit}(X)} \tag{5.10}$$

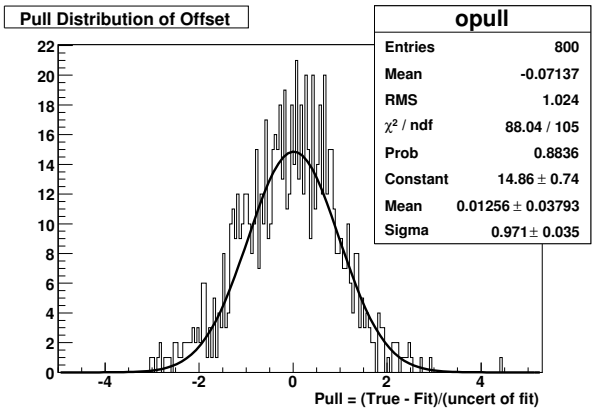


Figure 5.15. The EM energy offset pull distribution. The mean of ~ 0 and width of ~ 1 indicate the fit is unbiased.

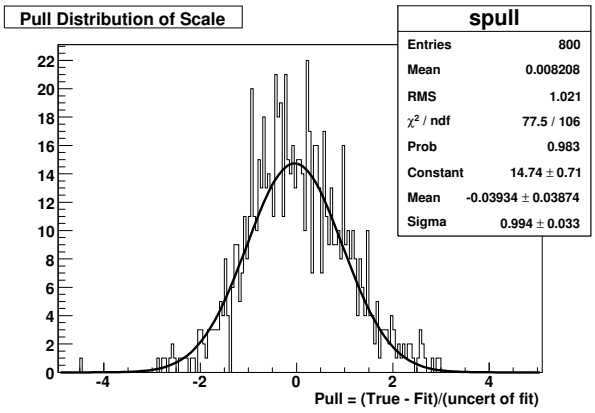


Figure 5.16. The EM energy scale pull distribution. The mean of ~ 0 and width of ~ 1 indicate the fit is unbiased.

where X is either the scale or the offset and σ is the uncertainty on parameter X found by the fit. This uncertainty is statistical in that it is related to the finite number of $Z \rightarrow ee$ events in data. If the fit is unbiased and the error estimates accurate then the two pull distributions will be described by a Gaussian distribution with a width of one and a mean of zero. Within the uncertainty on the mean and width due to the finite number of pseudo-experiments, the fit is unbiased (figures 5.15 and 5.16). This confirms that the fit behaves as expected and the uncertainties are accurately described.

The result of the fit to the data is a scale of $\alpha = 1.010 \pm 0.004$ and an offset of $\beta = -0.360 \pm 0.174$GeV with a correlation coefficient of -0.9949 (figure 5.3.3.2) [**86**]. It is important to note that though the uncertainties on the scale and offset are significant compared to the desired systematic uncertainty on the W mass the strong anti-correlation allows for a precise measurement.

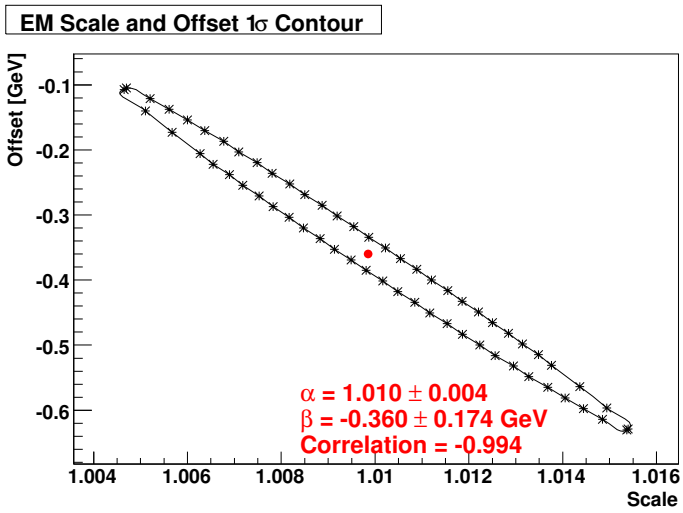


Figure 5.17. The 1σ contour of the EM scale and offset fit. Note the high degree of correlation.

5.3.4. Electron Energy Resolution

For an ideal calorimeter the fractional energy resolution can be parametrized by the following formula:

$$\frac{\sigma_{EM}(E)}{E} = \sqrt{C_{EM}^2 + \frac{S_{EM}^2}{E} + \frac{N_{EM}^2}{E^2}} \tag{5.11}$$

where C_{EM} is the constant term, N_{EM} the noise term and S_{EM} the sampling term for the EM calorimeter. The noise term accounts for resolution due to electronics noise, the small amount of latent radioactivity from the Uranium absorber plates, and the underlying event. The constant term accounts for the smearing introduced by the small mis-calibrations between different $\eta - \phi$ segments. It is independent of the energy and is therefore the most important term at the large electron energies studied in the W mass measurement.

This parametrization does not include any dependence on η_{phys}. We know an η_{phys} dependence has been introduced by the upstream material. As we saw in chapter four this material changes the shape of an electron shower and its location in the calorimeter, and therefore the sampling resolution.

We parameterize the sampling term as:

$$S_{EM} = (S_1 + \frac{S_2}{\sqrt{E}}) \times \frac{e^{S_{exp}/\sin\theta}}{e^{S_{exp}}} \tag{5.12}$$

where

$$S_{exp} = S_3 - S_4/E - S_5^2/E^2. \tag{5.13}$$

It is interesting to compare the predicted fractional energy resolution using this energy and angle dependent sampling term to the DØ Geant detector simulation. Figure 5.18 is the resolution for 45 GeV electrons as a function of η_{phys}. Figure 5.19 is the resolution as a function of energy for an electron at normal incidence. By factorizing the two effects we see that the model reasonable describes the Monte Carlo. To confirm this in the data we use $J/\psi \rightarrow ee$ events [**88**].

The resolution of the lower energy electrons from J/ψ decay is dominated by the sampling term. This low energy also restricts us to a narrow region of energy, preventing a detailed study of the energy dependence of the sampling term. Therefore, in the actual study we do not fit for the parameters of the sampling term in equation 5.12 and 5.13. Instead this is done by the parameterized model of the upstream material. The J/ψ events are used to confirm the η_{phys} dependence. Again we combine the pairs of electrons from J/ψ decays into categories. After taking into account the trigger efficiency and

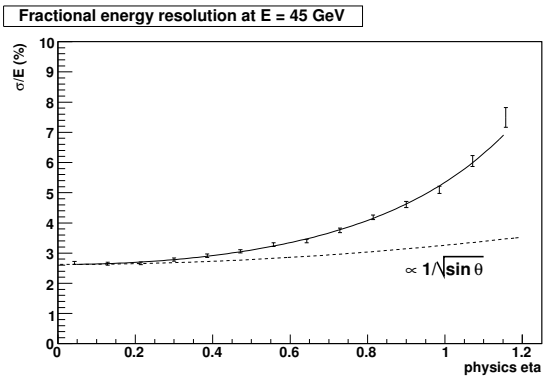


Figure 5.18. Fractional energy dependence as a function of electron η_{phys} for 45 GeV electrons.

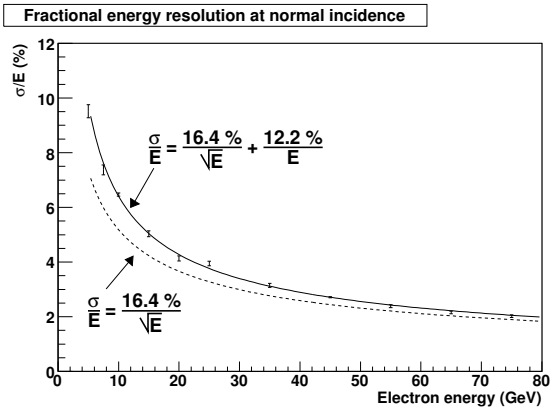


Figure 5.19. Fractional energy dependence as a function of electron energy, electrons at normal incidence.

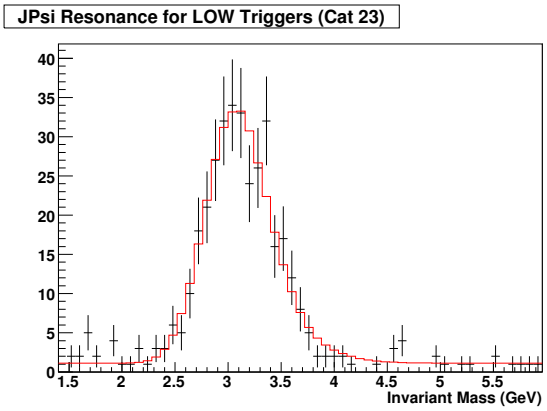


Figure 5.20. Mass of J/ψ in a particular electron η_{phys} category. "Trigger Low" refers to events selected by a trigger that required two towers with $E_T > 3$ GeV in the EM calorimeter.

the contribution of the noise term we compare the predicted and actual invariant mass distribution in the η_{phys} categories and fit for a non-energy dependent sampling term (as in figure 5.3.4). The good agreement across η_{phys} confirms that the model motivated by the investigations of the DØ Geant detector simulation is compatible with the data.

The constant term is measured using $Z \rightarrow ee$ events. We compare the invariant mass distribution predicted with PMCS for different hypotheses for the constant term to the data. We use a negative-log likelihood fit to determine the best value to be $2.35\% \pm 0.08\%$ [**89**].

5.3.5. Detector Efficiency

The measurement of M_W is relatively insensitive to absolute inefficiencies in the detector. The measurement depends only on the shape of the distributions, not on the absolute normalization. However, the efficiencies are not generally uniform over the kinematic distributions of interest and this will affect the measurement. There are several absolute efficiencies that we measure: The track matching efficiency, the Hmatrix (or electron ID) efficiency, the pre-selection efficiency and the trigger efficiency. In addition to this we also have three relative efficiencies. These are efficiencies that are related to the above selections, but studied as a function of parameters to which the mass measurement is particularly sensitive. These include the phimod efficiency (discussed previously), the scalar E_T (or SET) efficiency, and the $u_{\parallel}$ efficiency. We will address each of these in the following sections.

5.3.5.1. Trigger Efficiency. The single trigger per running period scheme selected in Chapter 4 simplifies the discussion of efficiencies. A tag-and-probe method is used with $Z \rightarrow ee$ events to measure the trigger efficiencies as a function of the electron p_T. In the tag-and-probe method we apply tight selection criteria to one electron in the $Z \rightarrow ee$ decay and then check if the other electron with only loose selection requirements passed the selection under investigation (in this case the trigger requirement). The efficiency is

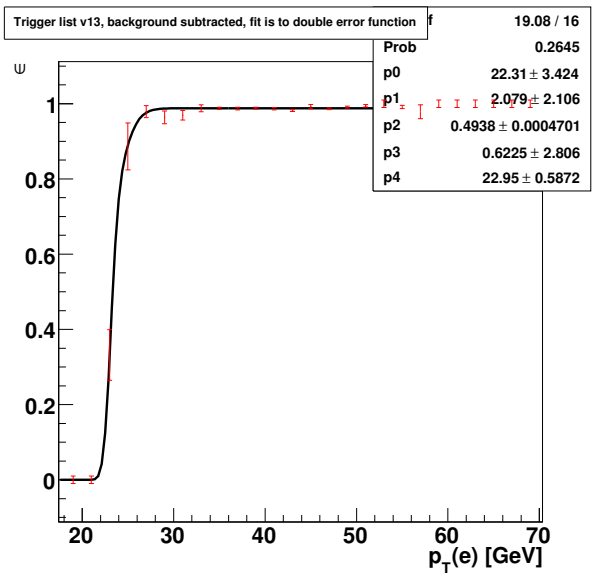


Figure 5.21. Trigger efficiency for the v13 trigger list. The histogram is fit to a double error function (black line).

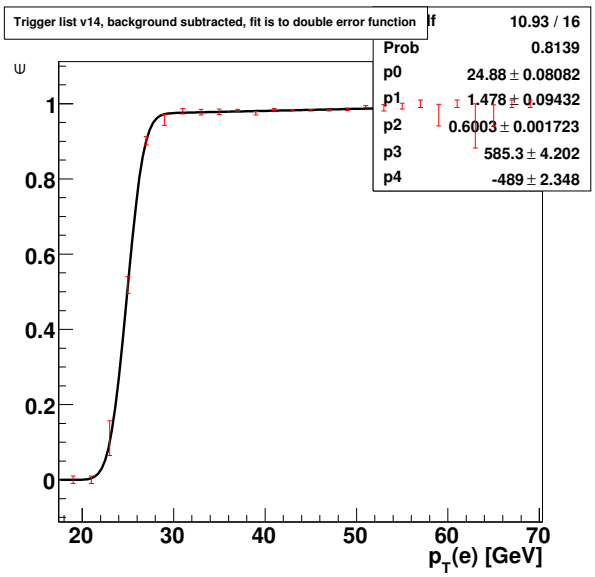


Figure 5.22. Trigger efficiency for the v14 trigger list. The histogram is fit to a double error function (black line).

shown in figures 5.21 and 5.22 with the background removed. A fit to a double error function is used to parameterize the efficiency.

5.3.5.2. Pre-selection Efficiency. The pre-selection is the efficiency for an electron to form an EM cluster which passes minimal criteria. This requires passing the isolation (> 0.15) and EM fraction (> 0.9) selection. Again we use a tag-and-probe method to study the efficiency, but because this efficiency would be biased by any calorimeter requirement we use an expanded sample definition that includes both calorimeter only and track only data. Here the tag electron passes the all the electron selection requirements, but the probe leg is only a track. In figure 5.23 we note that the efficiency is nearly flat over the CC region.

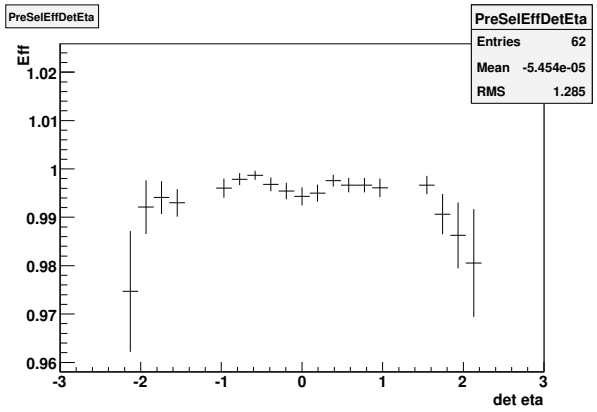


Figure 5.23. Pre-selection efficiency as a function of η_{det}.

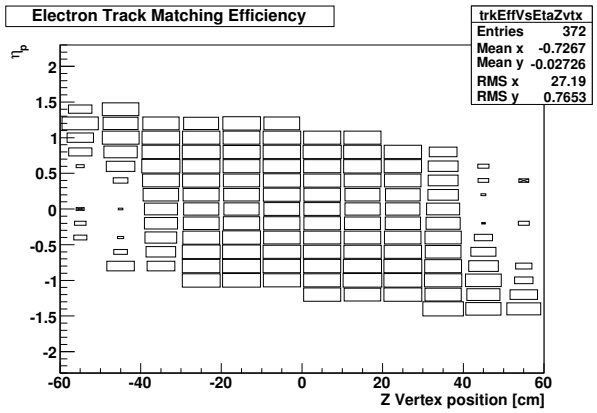


Figure 5.24. The track matching efficiency. The largest boxes indicated 100% efficiency.

5.3.5.3. Track Matching Efficiency. The track matching efficiency is determined as a function of η_{phys} and the vertex position. The nearly complete drop in efficiency after 40 cm is due to the requirement that all electrons have tracks that were observed by the SMT detector. The primary part of the SMT detector only extends to 40 cm. This efficiency is also measured using the basic tag-and-probe method. A correction as a function of the electron p_T, was found to be necessary and is included.

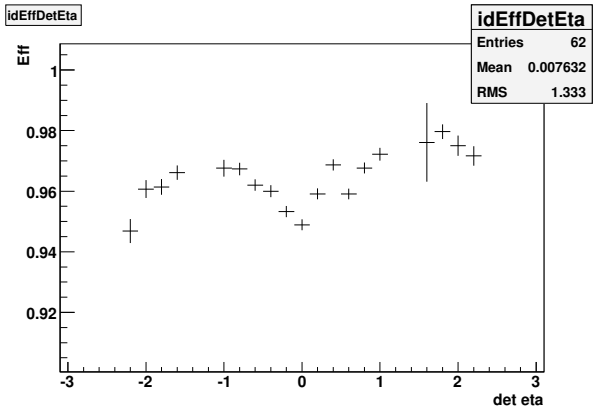


Figure 5.25. Hmatrix efficiency as a function of η_{det}.

5.3.5.4. Hmatrix Efficiency. The Hmatrix efficiency is also determined with the standard tag-and-probe method and background subtraction. It also has a p_T dependent correction.

5.3.5.5. $u_{\parallel}$ Efficiency. Our ability to identify electrons in the EM calorimeter is affected by the amount of recoil energy present in the calorimeter. The more hadronic recoil is in the same direction as the electron, the harder it will be to identify the electron. The components of the electron ID most affected are the track matching efficiency and the HMatrix and isolation efficiency. Our goal is to model this efficiency in the parameterized detector simulation. The usual strategy is to parameterize the shape of the efficiency as a function of $u_{\parallel}$. $u_{\parallel}$ is the recoil p_T parallel to the direction of the electron p_T. If $u_{\parallel} > 0$ GeV then the recoil is in the same direction as the electron, if $u_{\parallel} < 0$ GeV then the recoil is in the opposite direction of the electron. It is expected that for negative $u_{\parallel}$ the efficiency will be nearly constant, and that in the positive $u_{\parallel}$ region the efficiency will decrease as $u_{\parallel}$ becomes larger. In general, as $u_{\parallel}$ becomes more positive it becomes more challenging to model the electron and recoil systems.

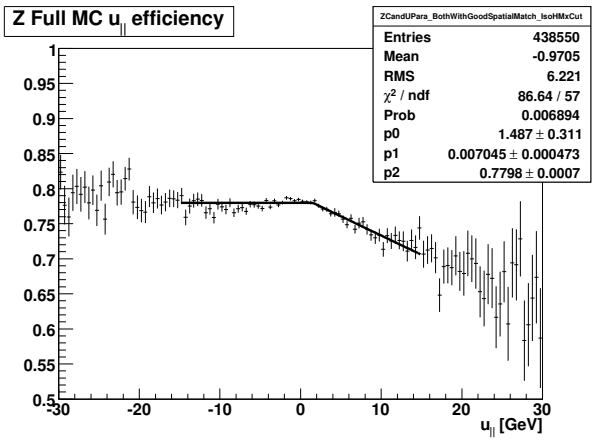


Figure 5.26. $u_{||}$ in Z events from the Geant detector simulation.

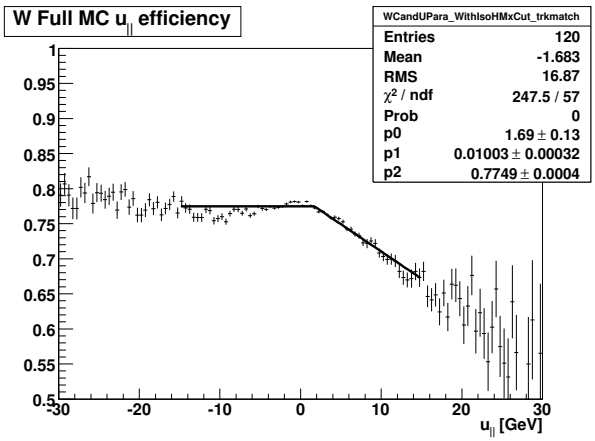


Figure 5.27. $u_{||}$ in W events from the Geant detector simulation.

We study the efficiency first with the DØ Geant detector simulation for both W and Z events. In the data we have the challenge of QCD background, so the strategy there is to use a tag-and-probe method with background subtraction in $Z \rightarrow ee$ events. However, in the detector the study is done by simply removing the HMatrix, isolation, and track matching selection, and then applying them and studying the change in efficiency as a function of $u_{\parallel}$. This is shown for Z and W events in figures 5.26 and 5.27. We require that the electrons be in the central calorimeter, and we accept CC-EC Z candidates. A function that is constant for $u_{\parallel} < 0$ GeV and linear for $u_{\parallel} > 0$ GeV is fit to the distributions. The key feature of the plot is the slope of the line for $u_{\parallel} > 0$ GeV. This tells us how quickly the efficiency is changing as a function of $u_{\parallel}$. For the Z and W events the slope is observed to be significantly different, and it is important to understand why.

It is useful to look at the $u_{\parallel}$ efficiency as a function of of η_{phys}. We select a range of $-1.4 < \eta_{phys} < 1.4$, with 0.1 wide bins. We find that, though different in Z and W events, the point where the the efficiency changes from flat to sloping is insensitive to η_{phys} and

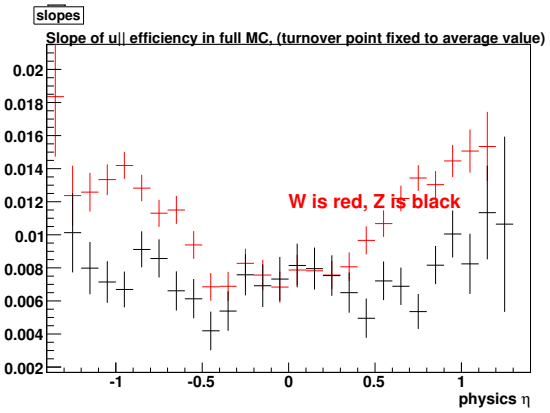


Figure 5.28. Geant MC W and Z $u_{\parallel}$ efficiency slope vs η_{phys}.

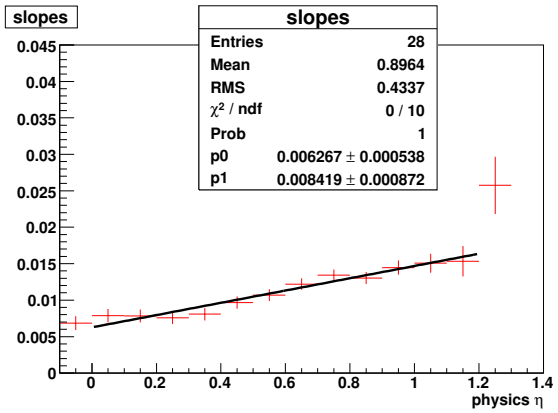


Figure 5.29. The W $u_{\parallel}$ efficiency slope for $\eta_{phys} > 0.0$ is fit to a line. The slope of the fitted line is non-zero.

so is fixed to the average value. It is the slope of the efficiency (and the overall efficiency) that changes as a function of η_{phys}. This is shown for W and Z events in Fig. 5.28. We note that in the most central region, $-0.3 < \eta_{phys} < 0.3$, the slope of the efficiency is nearly the same for both W and Z events. Versus η_{phys} the change in the slope of the $u_{\parallel}$ efficiency for Z events is consistent with zero. The change in the slope for the W events is found to depend significantly on the η_{phys}, the slope increasing with η_{phys}. This is fit to a line shown here in Fig. 5.29. We use this simple model, taken from the Geant MC, to describe the difference in PMCS.

The $u_{\parallel}$ efficiency is measured in data using the usual tag-and-probe technique with background subtraction. The efficiency is shown in figure 5.30. This is only a relative efficiency composed of the track matching HMatrix efficiency. The parametrization determined above is used in PMCS to shape those efficiencies as a function of $u_{\parallel}$.

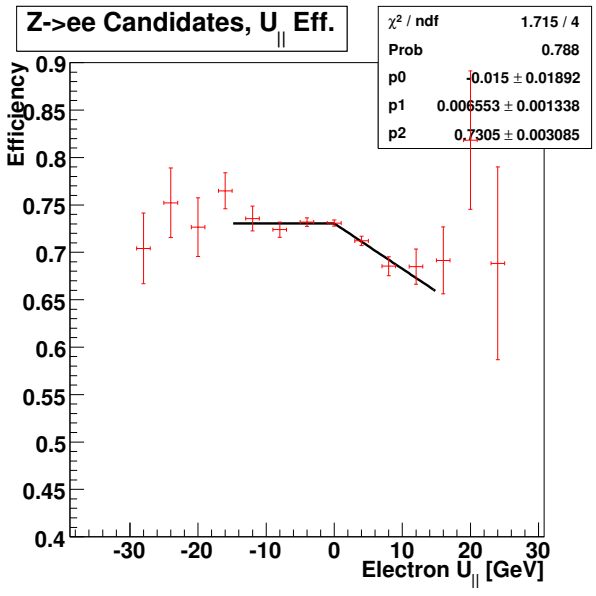


Figure 5.30. $u_{\parallel}$ in Z events in data after background subtraction.

5.4. Overview

After the above tuning several distributions are used as crosschecks with the $Z \rightarrow ee$ data. First is the invariant mass, already shown in figure 5.3.3.2. We preform a negative log likelihood fit to the data for the mass using templates created with PMCS, much as we will do with for the W mass. It is important to note that this is not a measurement of the Z mass; we rely on the precisely known value [**19**] throughout the calibration and tuning. We are simply checking to confirm the calibration and tuning preform as expected. We have used $M_Z = 91188$ MeV for calibration. Our value for the Z mass with $\mathcal{L} = 0.77$ fb^{-1} is $M_Z = 91196 \pm 32$ MeV, where the uncertainty is only the statistical uncertainty, confirming the success of the tuning.

To measure the W mass we will use the electron p_T distribution. Out tuning correctly describes Z p_T distribution, in figure 5.31. The description of the η efficiencies

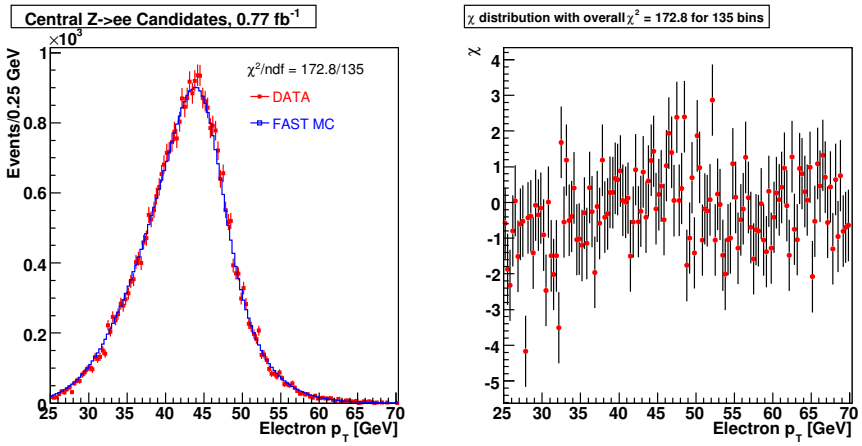


Figure 5.31. The electron p_T distribution in $Z \rightarrow ee$ events.

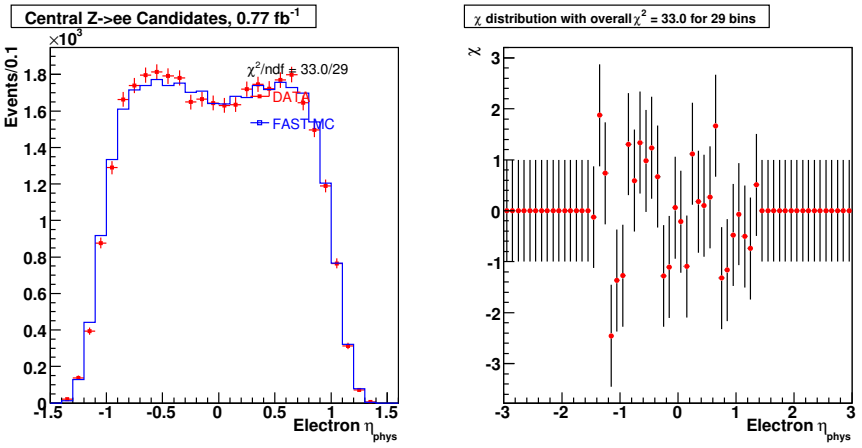


Figure 5.32. The electron η_{phys} distribution in $Z \rightarrow ee$ events.

directly affects the electron η_{phys} distribution, shown in figure 5.32, and the electron η_{det} distribution, shown in figure 5.33. The agreement with the data is good.

The $u_{\parallel}$ correction and efficiency affect the $u_{\parallel}$ and $u_{\perp}$ distributions. We see that PMCS describes this correctly in $Z \rightarrow ee$ events in figures 5.34 and 5.35.

We can conclude that the electron system is well-modeled. The final distribution of interest is the boson $p_T(ee)$ distribution, where the boson momentum has been determined

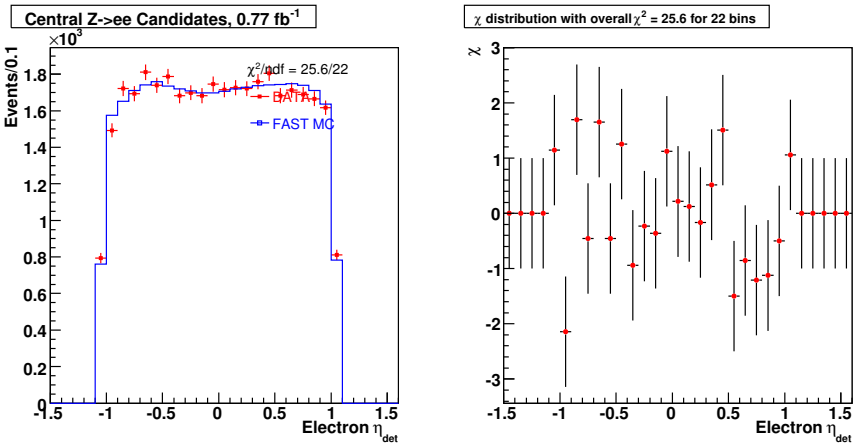


Figure 5.33. The electron η_{det} distribution in $Z \rightarrow ee$ events.

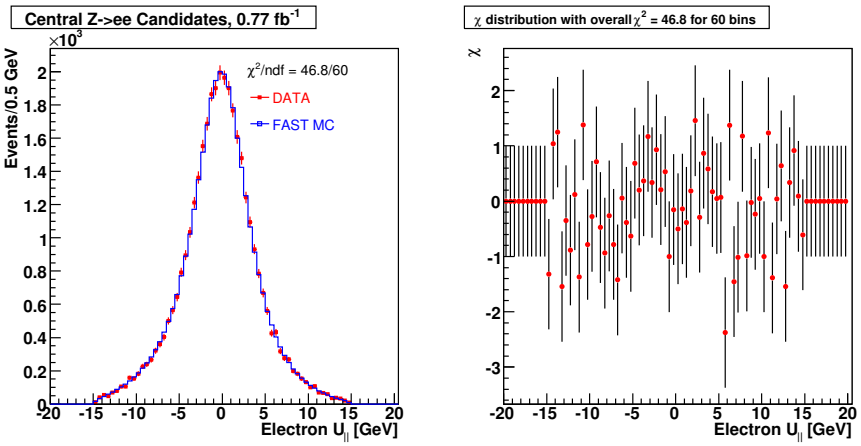


Figure 5.34. The $u_{\parallel}$ distribution in $Z \rightarrow ee$ events.

from the addition of the electrons. This cannot be measured in the $W \rightarrow e\nu$ events, but is used in $Z \rightarrow ee$ events to tune the recoil system by balancing the $p_T(ee)$ with the $p_T(rec)$. This is the focus of the next chapter.

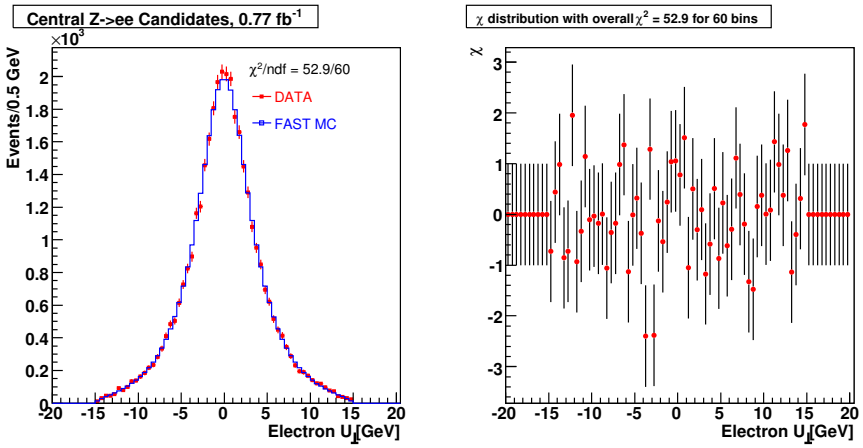


Figure 5.35. The $u_\perp$ distribution in $Z \to ee$ events.

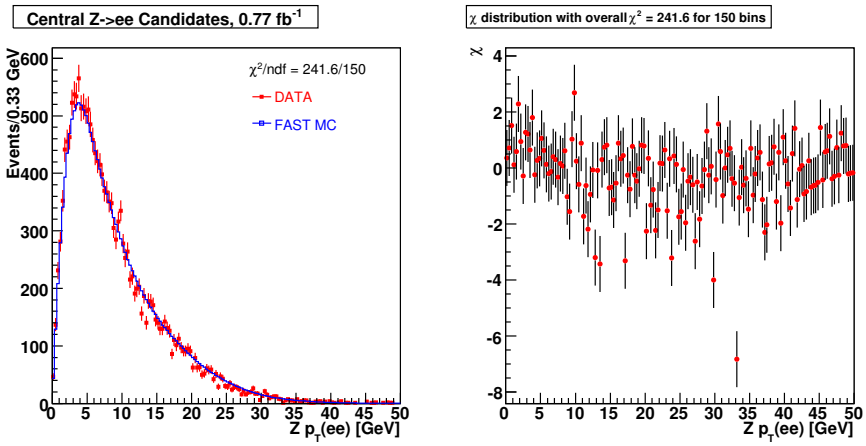


Figure 5.36. The $p_T(ee)$ distribution in $Z \to ee$ events.

CHAPTER 6

Recoil Measurement

In this chapter we discuss the measurement and simulation of the hadronic recoil.

6.1. Recoil Simulation

After the electron the other key observable in W boson decay is the recoil system. The interaction we observe is $p\bar{p} \rightarrow (W \rightarrow e\nu)X$ where X is the hadronic recoil. In practice the recoil contains all the energy in the event that was not the electron. The recoil model is assumed to be reducible to two independent parts: the hard, jet-like recoil of the boson off a soft gluon, generally localized in a specific region of the detector; and the soft, isotropic, recoil from the spectator quarks and other $p\bar{p}$ interactions in the event (multiple interactions). Here we describe the parameterized model of the recoil system implemented in PMCS. In the measurement of M_W using the electron transverse momentum the parametrisation of the recoil is of less importance than when using the M_T spectrum. Sensitivity to the recoil enters the analysis only indirectly through the selection requirement of $p_T(W) < 15$ GeV and the $u_\parallel$ correction to the electron energy and the $u_\parallel$ dependent efficiencies. Therefore this description is presented with less detail than the discussion of the electron model, and a much more comprehensive explication is contained in [**90**], which the discussion in this section is based upon.

It is necessary to describe the recoil energy response and resolution in the parameterized detector simulation. As mentioned, the two main contributions to the observed

recoil are:

a) The $p\bar{p}$ interaction that produced the W or Z boson.

b) Additional $p\bar{p}$ interactions associated with the same or with previous beam crossings, as well as detector noise.

We parameterize the transverse momentum of the hadronic recoil as :

$$\vec{u}_T = \vec{u}_T^{\,\mathrm{HARD}} + \vec{u}_T^{\,\mathrm{SOFT}} + \vec{u}_T^{\,\mathrm{UPARA}} + \vec{u}_T^{\,\mathrm{PHOTON}}$$

where

$$\begin{aligned}
\vec{u}_T^{\,\mathrm{HARD}} &= \vec{f}(\vec{q}_T) \\
\vec{u}_T^{\,\mathrm{SOFT}} &= \alpha_{mb} \cdot \vec{E}_T^{\,\mathrm{MB}} + \vec{E}_T^{\,\mathrm{ZB}} \\
\vec{u}_T^{\,\mathrm{UPARA}} &= -\sum_e \Delta u_{\parallel} \cdot \vec{p}_T(e) \\
\vec{u}_T^{\,\mathrm{PHOTON}} &= \sum_\gamma \vec{p}_T(\gamma)
\end{aligned}$$

and:

- $\vec{f}(\vec{q}_T)$ is a function which provides the smeared p_T vector for the hard component of the recoil.
- α_{mb} is a correction factor used for adjusting the soft component of the parameterized recoil.
- $\vec{E}_T^{\,\mathrm{MB}}$ is the transverse energy balance from the Minimum Bias (MB) events
- $\vec{E}_T^{\,\mathrm{ZB}}$ is the transverse energy balance from the Zero Bias (ZB) events
- $\Delta u_{\parallel}$ is the transverse energy flow of the recoil into the electron window

- $\vec{p}_T(\gamma)$ is the transverse momentum of an FSR photon

To summarize, the four components of the recoil parametrisation are:

a) The "hard" component representing parton-parton interaction that produced the boson. This component is most directly correlated with the true boson p_T.

b) The "soft" component representing the interaction of spectator partons from the $p\bar{p}$ collision that produced the boson (the underlying event), and any other soft $p\bar{p}$ collision in the event (multiple interactions), as well as detector noise.

c) The $u_{\parallel}$ component that accounts for the part of the recoil system that was deposited in the electron window and is measured as electron energy. The $\Delta u_{\parallel}$ correction is added back to the recoil.

d) The photon component that accounts for FSR photons which were emitted from the electron but radiated outside the electron cone and were reconstructed as recoil.

We will first discuss the parametrization of the hard and soft components separately, and then the tuning of the combined quantity $\vec{u}_T$ to the data.

6.1.1. Hard Recoil Simulation

The hard recoil cannot be studied separately from the rest of the event in data. To study this with the Geant detector simulation it is convenient to use $Z \rightarrow \nu\nu$ events. This decay has unobservable products, but the MC advantageously allows us to examine only the hadronic recoil of the boson in the absence of the electrons. The $Z \rightarrow \nu\nu$ events are reconstructed without any contribution from the underlying event or multiple interactions added. In order to make the sample as kinematically similar to $Z \rightarrow ee$ events we require the neutrinos to have $\eta_p < 1.3$.

A simple model of $\vec{u}_T$ that ignores the correlations between the azimuthal direction ϕ and magnitude of the recoil, and treats the ϕ and p_T resolutions as Gaussian functions, is not sufficient for the present data sample. The following variables are useful in describing the recoil system:

- $R = \dfrac{u_T - q_T}{q_T}$: the recoil p_T resolution ($R < 1$),
- $Resp = \dfrac{u_T}{q_T}$: the recoil response,
- $\Delta\phi = \phi(\vec{u}_T) - \phi(\vec{q}_T)$: the recoil angular resolution ($|\Delta\phi| < \pi$),
- $Resp_{prj} = \dfrac{\vec{u}_T \cdot \vec{q}_T}{q_T}$: the projected recoil response.

We separate the events into bins according to their true recoil p_T. In each bin a two-dimensional distribution of events is made by plotting the p_T resolution versus the ϕ resolution (figs. 6.1, 6.2).

This distribution is then fit to the following function:

$$pdf(x,y) = p_0 \exp\left[-\frac{1}{2}\left(\frac{x-\mu(y)}{\sigma_x(x,y)}\right)^2\right] \exp\left[-\frac{1}{2}\left(\frac{y}{\sigma_y(y)}\right)^2\right],$$

where: $x \equiv R$, $y \equiv \Delta\phi\,[rad]$, $\mu(y) = p_1 + p_2 \cdot y$,

$$\sigma_x(x,y) = \begin{cases} p_3, & x < \mu(y) \\ p_4, & x > \mu(y) \end{cases}, \; \sigma_y(y) = p_5 + p_2 \cdot y \text{ and}$$

$p_0 \ldots p_5$ are parameters of the fit.

Five parameters are used to describe the distribution of the R and $\Delta\phi$ for each bin of true recoil p_T, the sixth being only for normalization. Given a true recoil p_T and ϕ from the event generator PMCS uses this set of 32 functions to predict the p_T response and resolution and the ϕ resolution.

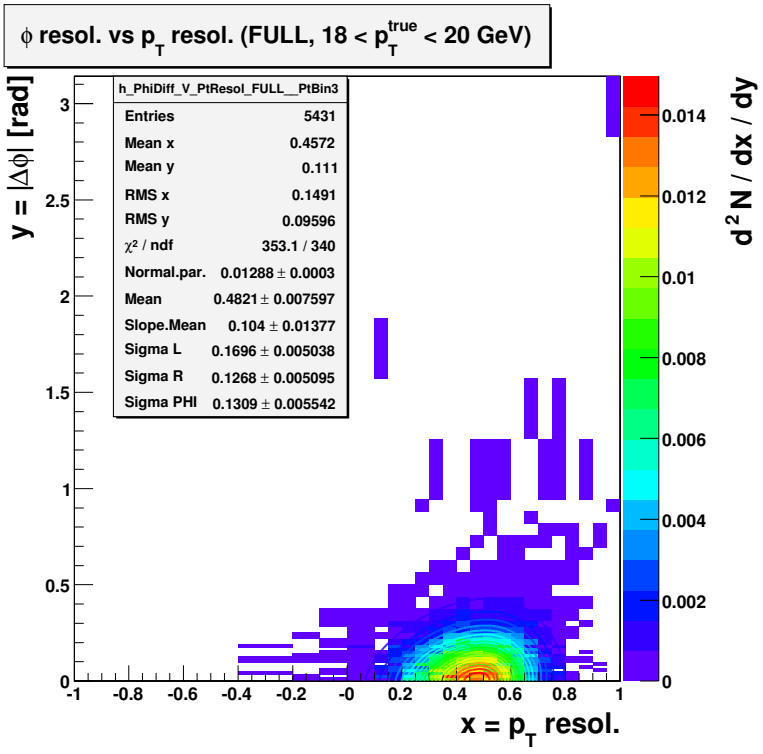


Figure 6.1. The 2D distribution of the recoil response resolution R and the ϕ resolution for a Z boson with 20 GeV p_T. The distribution of events is shown by the boxes and the lines are the contours of the function derived from the fit.

6.1.2. Soft Recoil Simulation

The soft recoil describes the energy in the calorimeter from the soft QCD interactions of the spectator partons (underlying event), additional $p\bar{p}$ interactions from the same or previous beam crossings (multiple interactions), detector noise and pileup. Here we consider detector noise in include electronics noise, uranium decays, cosmic rays and beam-related backgrounds. Pileup refers to residual energy in the detector from the previous beam crossing. In $Z \rightarrow ee$ events at the instantaneous luminosities in Run IIa the underlying event and multiple interactions have comparable scalar E_T. The scalar

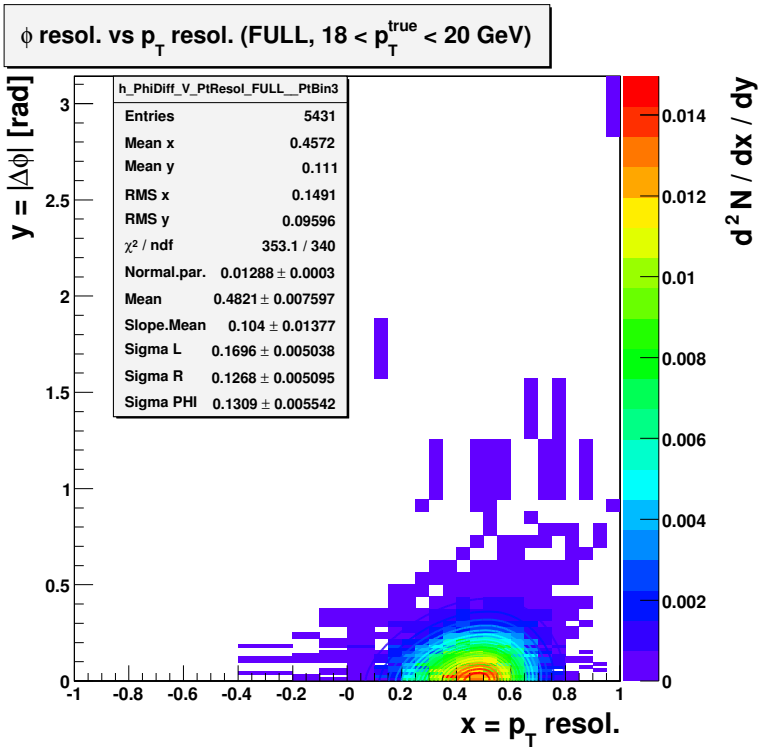


Figure 6.2. The 2D distribution of the recoil response resolution R and the ϕ resolution for a Z boson with 5 GeV p_T. The distribution of events is shown by the boxes and the lines are the contours of the function derived from the fit.

E_T (SET), shown in figure 6.4, is the scalar sum of all the energy in the calorimeter. We see in figure 6.3 the contribution of the underlying event and multiple interactions to the energy of the the Z event, as modeled in the DØ Geant detector simulation. In data we observe that Z events have an average of 1.9 vertexes [**90**], meaning there is slightly less than one spectator parton interaction or multiple interaction per event. From table 6.1.2 we can conclude that approximately 30 GeV of SET comes from the underlying event and 20 GeV per additional $p\bar{p}$ interaction.

The soft recoil is studied using two additional samples of events: the minimum bias and zero bias samples. The minimum bias sample is collected by a trigger that only

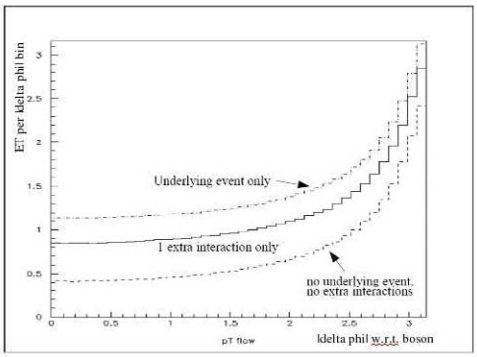


Figure 6.3. The contribution of the underlying event and addition $p\bar{p}$ interactions to the recoil of a Z boson event, as a function of $\Delta\phi$.

Table 6.1. Average SET for different primary vertices in a Z event

Number of primary vertices (excluding vertex of Z)	Mean SET [GeV] (excluding electron cones)
0	33
1	53
2	74
3	92

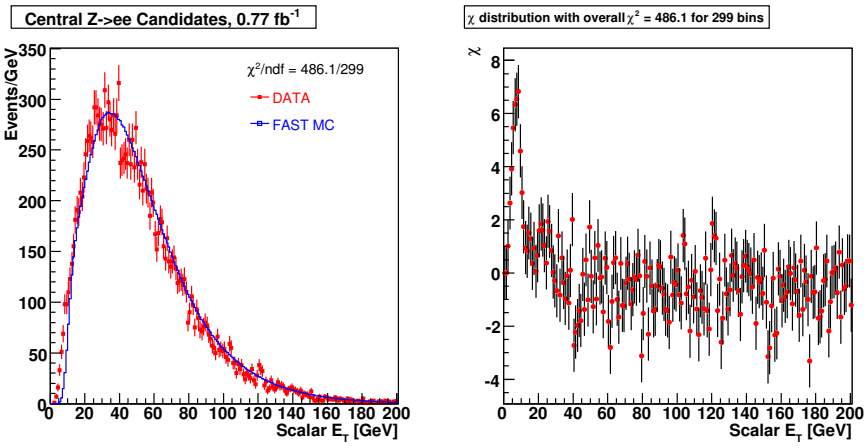


Figure 6.4. The Scalar E_T measured in $Z \rightarrow ee$ events with the standard selection.

requires an inelastic collision in the event. These events are used to study the underlying event since the inelastic collisions are essentially the result of the QCD interactions we must describe. However, because the effects involve different physical processes, we would like to separate the study of the underlying event and multiple interactions. As we have seen these effects have on average similar energies, so taken together it would be difficult to distinguish their effects. We therefore select minimum bias events with exactly one vertex, which eliminates additional interactions.

The environment of the minimum bias events is generally somewhat different from the actual underlying event. The minimum bias events generally are not associated with a hard scatter that produces a vector boson. The conditions that result in the production of a vector boson lead to a large spatial overlap between the proton and anti-proton. Therefore there is a higher probability for additional hard or "semi" hard scatters within the same event [**78**]. This difference between the underlying event and minimum bias events is accounted for by matching the SET spectrum in the minimum bias events and $Z \rightarrow ee$ events. We require $p_T(Z) < 3$ GeV to reduce the SET contribution of the hard recoil and we exclude the SET within the electron cone. Then the SET distribution of the minimum bias sample is weighted to match the data. This procedure is studied and tested using the Geant detector simulation and the SET distribution before and after weighting to the minimum bias events is compared to $Z \rightarrow ee$ in figures 6.5 and 6.6.

The zero bias sample consists of events with no selection except that the detector was read out in time with the beam crossings. This is ideal for studying multiple interactions along with the detector noise and pileup. In this case there is no need to scale the energy.

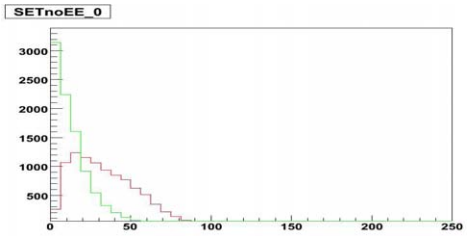


Figure 6.5. The scalar E_T of minimum bias events compared to the SET in Z events (MC simulated with Pythia and the Geant detector simulation).

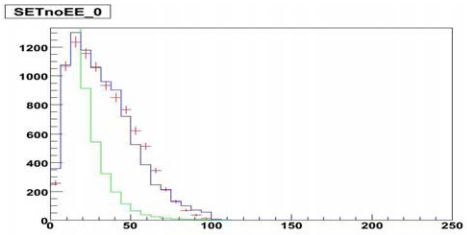


Figure 6.6. The scalar E_T of minimum bias events compared to the SET in Z events after weighting the minimum bias events (MC simulated with Pythia and the Geant detector simulation).

The soft recoil model is then the combination of the zero bias events and the minimum bias events with one vertex. The minimum bias events also include a contribution from the detector noise, pileup and soft interactions which results in a "double counting" of these effects. This double counting is accounted for in the tuning of the total $\vec{u}_T$ of PMCS. Because we have very large samples of zero and minimum bias data (compared to the W or Z events) we implement this model in PMCS by creating "libraries" of these events. For each event in the simulation we randomly select a minimum bias and zero bias event from the library.

6.1.3. Hadronic Model Tuning

We have assumed that the hard recoil and the soft recoil can be modeled independently. This assumption is a useful approximation, but the response and the resolution of the calorimeter both change in the presence of additional energy. This prevents the hard and soft recoil from being completely independent and introduces a correlation. The correlation arises primarily from the zero suppression of the calorimeter readout and pileup from previous beam crossings.

As we have seen zero suppression is used to reduce the number of calorimeter cells read out by excluding those cells with little energy, or energy consistent with incoherent noise. However, the underlying event and multiple interactions add energy to the calorimeter isotropically, scaling with $\mathcal{L}$. As can be seen from the distribution of instantaneous luminosity in figure 6.7 there is a significant range over which this may vary during Run IIa of the Tevatron. Consequently, this decreases the number of cells that will be zero suppressed and artificially increases the recoil energy observed as a function of the instantaneous luminosity. This effect is studied in with the DØ Geant detector simulation with Pythia Z events by adding and then removing the simulation of the multiple interactions. We find that the response changes by 10 to 15 percent with additional interactions. This motivates the necessity of adding a parametrization of the recoil that accounts for the correlations between the hard and soft components. This overall parametrization adjusts the energy response and resolution of the recoil and is derived by comparing the prediction of the total $\vec{u}_T$ to the $Z \rightarrow ee$ events in the data.

To tune the recoil parametrization we rely on the calibration of the EM calorimeter and the well understood electron energy parametrization in PMCS. The tuning is derived by

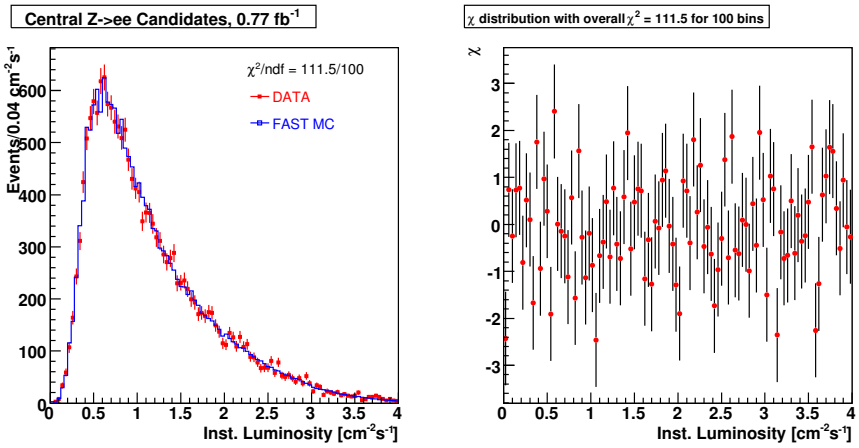


Figure 6.7. The instantaneous luminosity distribution of $Z \rightarrow ee$ events.

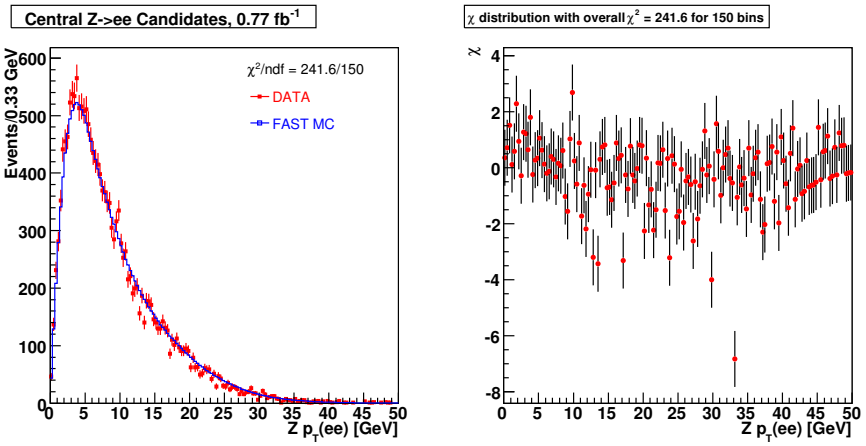


Figure 6.8. The $p_T(ee)$ distribution of $Z \rightarrow ee$ events. As a result of the work described in chapter five the agreement between data and PMCS is good overall, but particularly in the region of interest: $p_T(ee) < 30$ GeV.

balancing the transverse momentum of the electron system (shown in figure 6.8) against the transverse momentum of the recoil system (fig. 6.9, after tuning). In doing this it is convenient to adopt the coordinate system shown in figure 6.10.

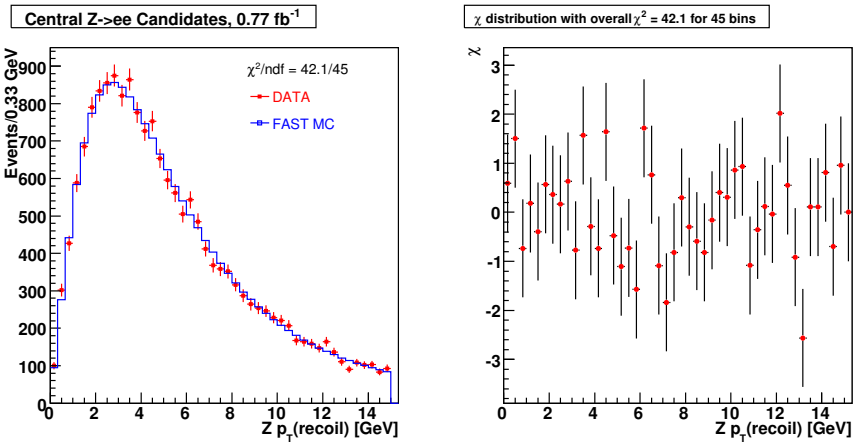


Figure 6.9. The $p_T(rec)$ distribution of $Z \rightarrow ee$ events after tuning the recoil system.

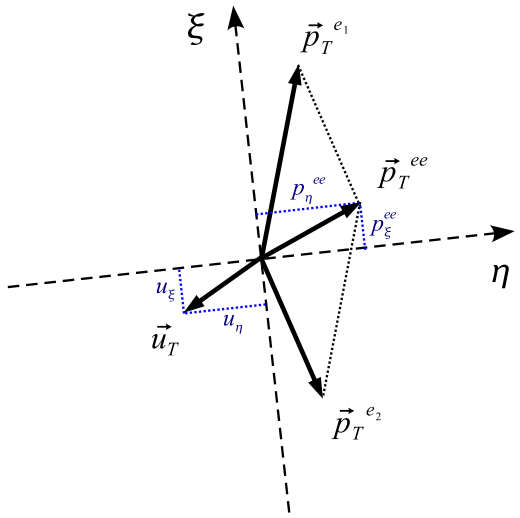


Figure 6.10. The UA2 coordinate system reduces our sensitivity to the electron resolution when tuning the recoil system.

In practice we balance of the transverse momentum projected along the η and ξ axes. The η and ξ balance are defined as

$$\eta_{imb} = \vec{p}_T^{\,ee} \cdot \hat{\eta} + \vec{u}_T \cdot \hat{\eta},$$

$$\xi_{imb} = \vec{p}_T^{\,ee} \cdot \hat{\xi} + \vec{u}_T \cdot \hat{\xi},$$

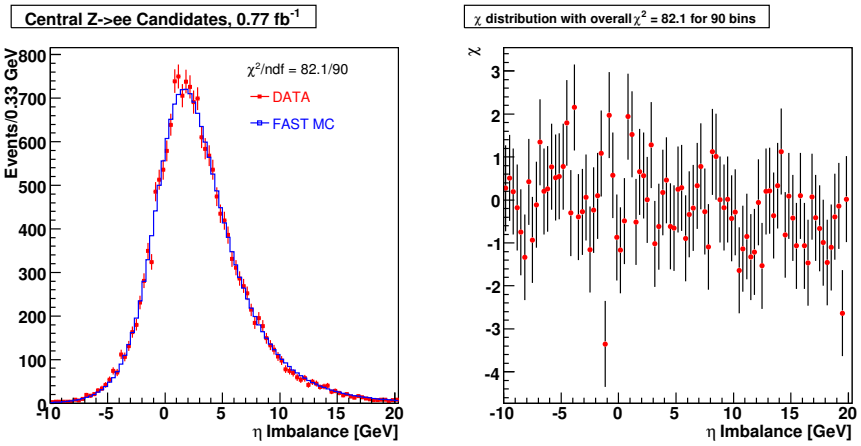


Figure 6.11. The $\eta_{\rm imb}$ distribution of $Z \rightarrow ee$ events after tuning the recoil system. The mean of this distribution is most sensitive to the p_T response of the recoil system and the width is sensitive to the resolution.

where $\vec{p}_T^{\,ee}$ is the observed di-electron momentum and $\vec{u}_T$ is the recoil momentum. The projection of the di-electron and recoil momentum along the $\hat{\xi}$ and $\hat{\eta}$ directions is written as $p_\eta^{\,ee}$ and u_η. This construction minimises the sensitivity of the tuning to the electron energy resolution, and was first developed by the UA2 Collaboration [**7**]. The η_{imb} distribution is used to tune the recoil momentum response and resolution (fig. 6.11). The width of the distribution is sensitive to the resolution and the mean is sensitive to the response. The ξ_{imb} distribution is relatively insensitive to the recoil tuning and used as a cross check (fig. 6.12).

The response and resolution are parameterized by the following formulae:

$$R = A + B\exp(-p_T^{\rm gen}/\tau)$$

$$\sigma_R = \sigma_A + \frac{\sigma_B}{p_T^{\rm gen}}$$

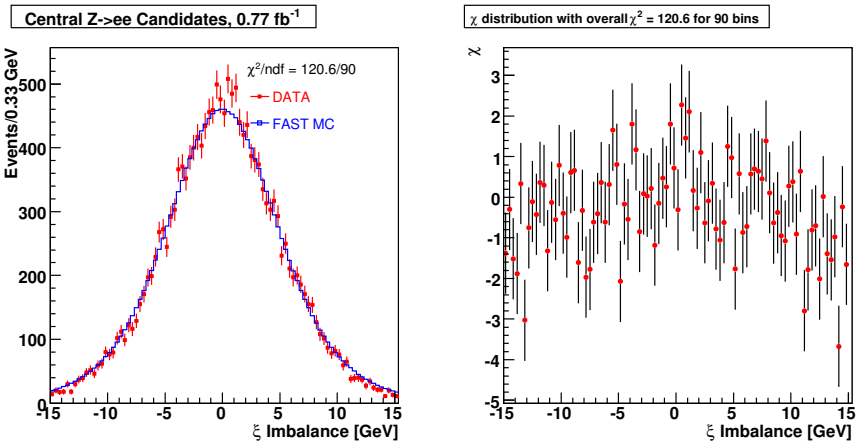


Figure 6.12. The $\xi_{\rm imb}$ distribution of $Z \rightarrow ee$ events after tuning the recoil system.

where R is the recoil momentum response and σ_R is the resolution. The $p_T^{\rm gen}$ is the boson p_T from the event generator. This response and resolution are applied to the hard recoil. An additional parameter α_{MB} is used to tune the underlying event energy of the soft recoil as follows:

$$p_y^{ue} = -\sqrt{\alpha_{MB}} E_y^{ue}$$

$$p_x^{ue} = -\sqrt{\alpha_{MB}} E_x^{ue}$$

where E_i^{ue} is the energy read from the randomly chosen event in the minimum bias library. The parameters A, B, σ_A and α_{MB} are determined by χ^2 fits of the η_{imb} distribution to the data, and parameters τ and σ_B are fixed to 5.0 GeV and 0.0 GeV after close examination of the data [**91**]. Two χ^2 fits are used to determine the four parameters. Again we use a template method where we compare distributions predicted at different values of A, B, σ_A and α_{MB} to the distribution in the data. Because the parameters A and B

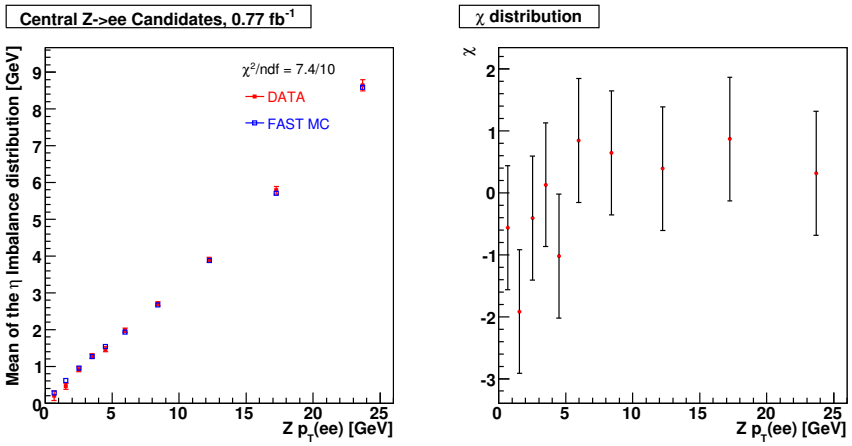


Figure 6.13. The mean of the $\eta_{\rm imb}$ distributions in bins of $\vec{p}_T^{\,ee}$ in the data and PMCS.

describe the response the mean of the η_{imb} distribution is examined in the fit. The width of the distribution is used to determine σ_A and α_{MB}. The events are separated into ten bins by $\vec{p}_T^{\,ee}$ and the η_{imb} is plotted in each bin. The mean and width of the η_{imb} is determined by fitting the distribution to a Gaussian function. The parameters are found to be $A = 0.922 \pm 0.014$, $B = 0.70 \pm 0.12$, $\sigma_A = 1.09 \pm 0.07$ GeV and $\alpha_{MB} = 0.66 \pm 0.08$ [**92**]. In figure 6.13 is shown mean of the η_{imb} in Z events as a function of $\vec{p}_T^{\,ee}$ after tuning PMCS to the data. Figure 6.14 is the width of the η_{imb} as a function of $\vec{p}_T^{\,ee}$ after tuning. The good agreement is expected as we are comparing the predictions to the data sample from which they were derived. We also note that the ϕ position of the recoil (relative to the di-electron momentum) is well described by the original, uncorrelated model of the soft and hard recoil without any need for parametrization. In figure 6.15 we again separate the events into bins by $\vec{p}_T^{\,ee}$ and plot the $\Delta\phi$ between the di-electron and recoil momentum in Z events.

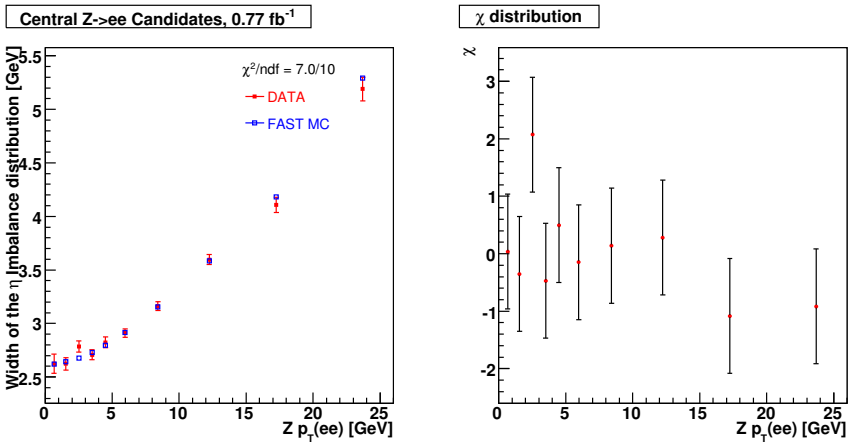


Figure 6.14. The width of the $\eta_{\rm imb}$ distributions in bins of $\vec{p}_T^{\,ee}$ in the data and PMCS.

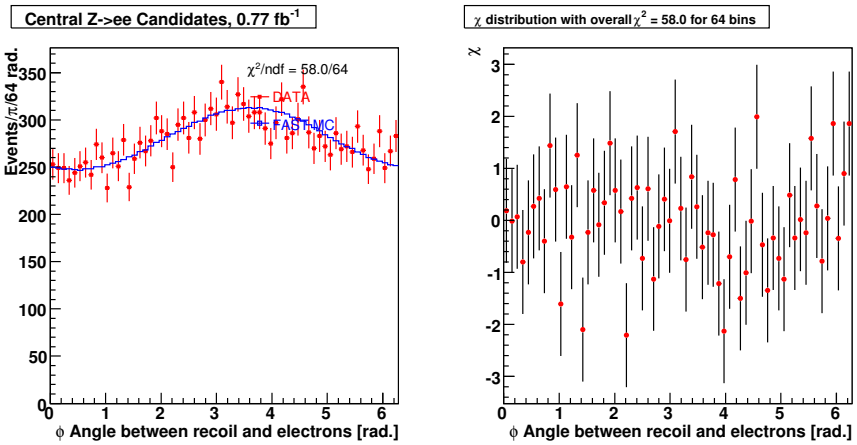


Figure 6.15. $\Delta\phi$ between the di-electron system and recoil momentum in Z events as a function of $\vec{p}_T^{\,ee}$.

6.2. Scalar E_T

The scalar E_T (SET) is also modeled in a manner similar to the hard recoil. It is studied with the same $Z \to \nu\nu$ Pythia events and a parametrization is derived. The SET of the minimum and zero bias events is weighted to match the distribution observed in $Z \to ee$ events.

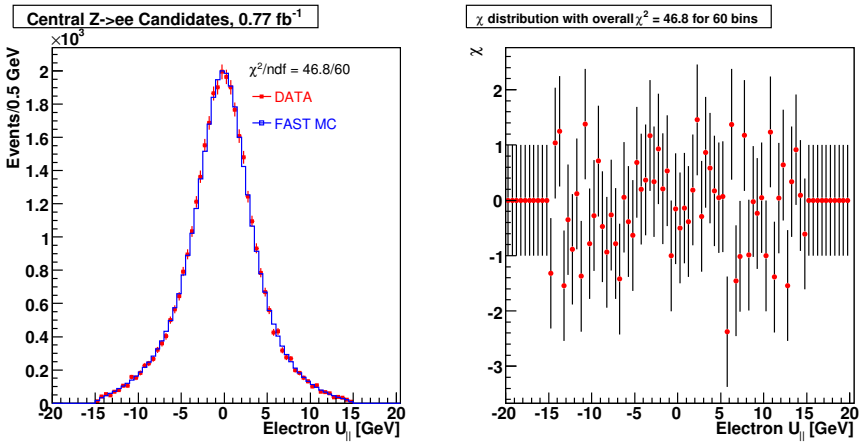


Figure 6.16. The $u_{\parallel}$ distribution in $Z \rightarrow ee$ events.

6.3. Overview

The combined model of the hard and soft recoil, once tuned, provides a good description of the observed distributions in $Z \rightarrow ee$ events. We expect the $W \rightarrow e\nu$ system to be very similar and compare predictions to the distributions observed in the data. Of first importance is the W p_T distribution in figure 6.18. The prediction distribution agrees with the observed. Next we examine the $u_{\parallel}$ and $u_{\perp}$ distributions in $W \rightarrow e\nu$ events in figures 6.19 and 6.20 (for comparison we reproduce the $u_{\parallel}$ and $u_{\perp}$ distributions from chapter five in figures 6.16 and 6.17). The $u_{\parallel}$ distribution is described quite poorly by PMCS. This indicates a critical problem because the $u_{\parallel}$ correction directly affects the mass measurement and the $u_{\parallel}$ efficiency shapes the distributions we will use to determine the mass. We will address this further in chapter nine and for now simply remark that one likely source of the discrepancy may be the poorly understood background contribution.

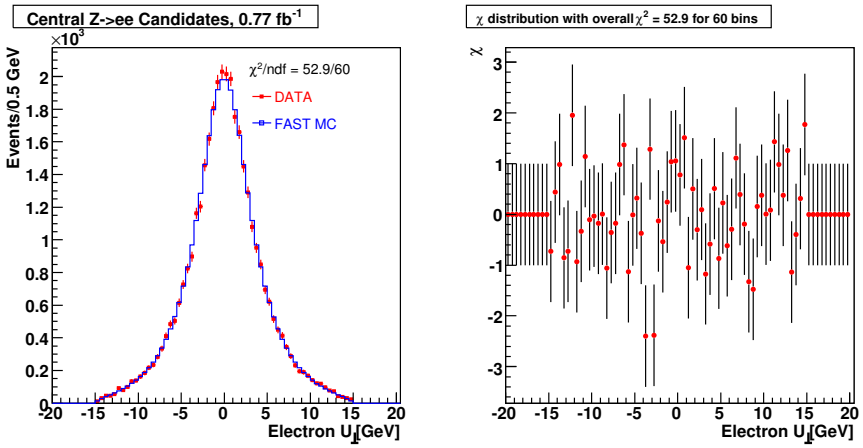


Figure 6.17. The $u_\perp$ distribution in $Z \rightarrow ee$ events.

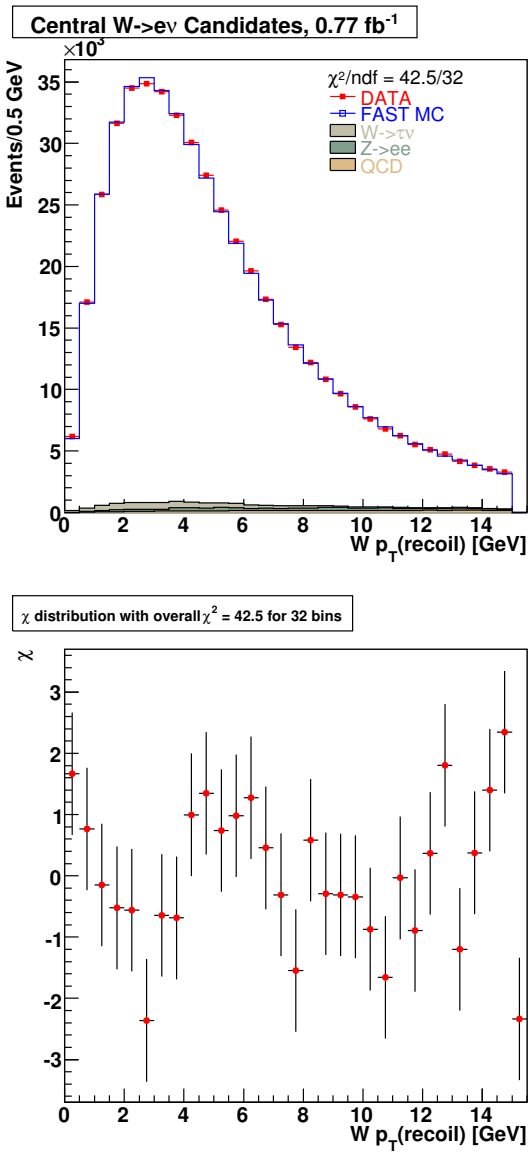


Figure 6.18. The W recoil p_T distribution in data and PMCS.

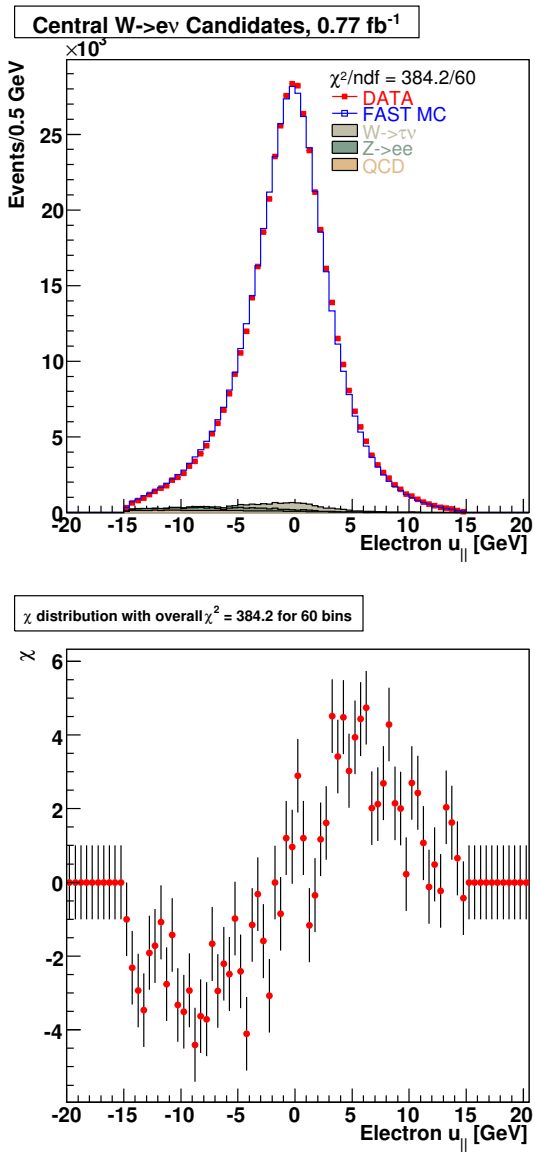


Figure 6.19. The W $u_{\parallel}$ distribution in data and PMCS. The description of the distribution by PMCS is poor.

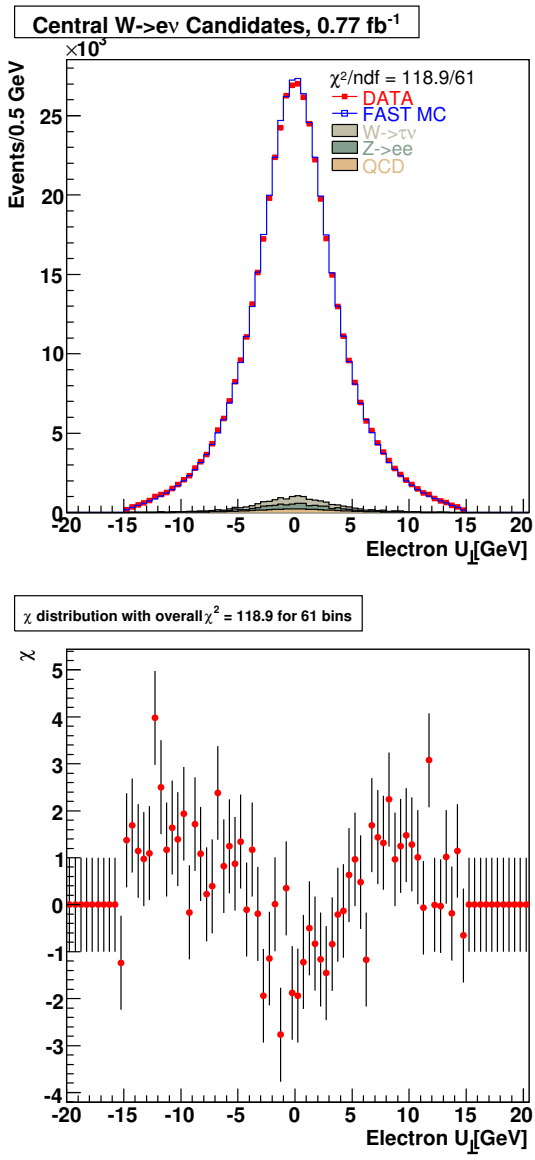


Figure 6.20. The W $u_\perp$ distribution in data and PMCS.

CHAPTER 7

Backgrounds

In this chapter we will describe the background processes that are present in the $W \rightarrow e\nu$ sample and how they affect the mass measurement. The background events change the shape of the distributions used to determine the W mass, as well as distributions used as cross checks. There are three major sources of background: $Z \rightarrow ee$ where one of the electrons is lost or misidentified, $W \rightarrow \tau\nu \rightarrow e\nu\nu\nu$ which is indistinguishable from the signal, and QCD background where in a di-jet event on jet is misidentified as an electron. Though the backgrounds are important, the $W \rightarrow e\nu$ signal is very clean in the region we will fit over and each background only contributes approximately 1% of the events in the sample. In application we do not subtract the background distributions from the data, but rather add the normalized background distributions to the distributions and templates generated by PMCS. Much of this work is documented in greater detail in [**93**] and this discussion relies on that work.

7.1. $Z \rightarrow ee$ Background

The $Z \rightarrow ee$ background is studied by simulating $Z \rightarrow ee$ decays with Pythia and the DØ Geant detector simulation. If one of the electrons is mis-measured, or passes through an un-instrumented region of the detector, the event will appear to have a large $\not\!\!E_T$ and one electron. This sort of event will then pass the W selection. A large sample of $Z \rightarrow ee$ MC is generated and the W selection is applied. The remaining events are

Source	Fraction	Uncertainty M_T [MeV]	Uncertainty $p_T(e)$ [MeV]	Uncertainty $\not\!\!E_T$ [MeV]
QCD	$1.0 \pm 0.03\%$	2.0 ± 0.3	3.4 ± 0.4	3.0 ± 0.3
$W \to \tau\nu$	$1.6 \pm 0.02\%$	1.4 ± 0.2	2.0 ± 0.3	2.0 ± 0.3
$Z \to ee$	$1.1 \pm 0.05\%$	1.0 ± 0.1	1.0 ± 0.1	1.0 ± 0.1

Table 7.1. Summary of the three most prominent background fractions and their uncertainties. From [**93**].

the background. To account for the acceptance and efficiency the background fraction is found by comparing the number of $Z \to ee$ events that pass the selection to the number of $W \to e\nu$ events that pass the selection, and adjusting the by the ratio of the W and Z cross-section. A background fraction of 1.1 ± 0.05 % is found. This uncertainty is propagated to the to the W mass and the results are summarized in table 7.1. The $Z \to ee$ background is shown in green in figure 7.1 for the electron transverse momentum distribution and 7.2 for the transverse mass distribution.

7.2. $W \to \tau\nu$

The $W \to \tau\nu$ background is studied by simulating these decays with Pythia and the DØ Geant detector simulation. In this case the background is identical to the signal as the τ decays to $e\nu\nu$. We simulate $W \to \tau\nu \to e\nu\nu\nu$ with Pythia the DØ detector simulation, and apply the W selection. Because this is a four body decay the final electron is much softer than the electron from $W \to e\nu$ decay, and the Jacobian edge is no longer centered on the W mass. In figures 7.4 and 7.3 we see that the edge has moved significantly lower. Due to lepton universality the cross-section for a W to decay to a τ is identical the cross-section for an electron, and we can directly compare the number of events that pass the selection and determine the background fraction. We find a fraction of 1.6 ± 0.02 %

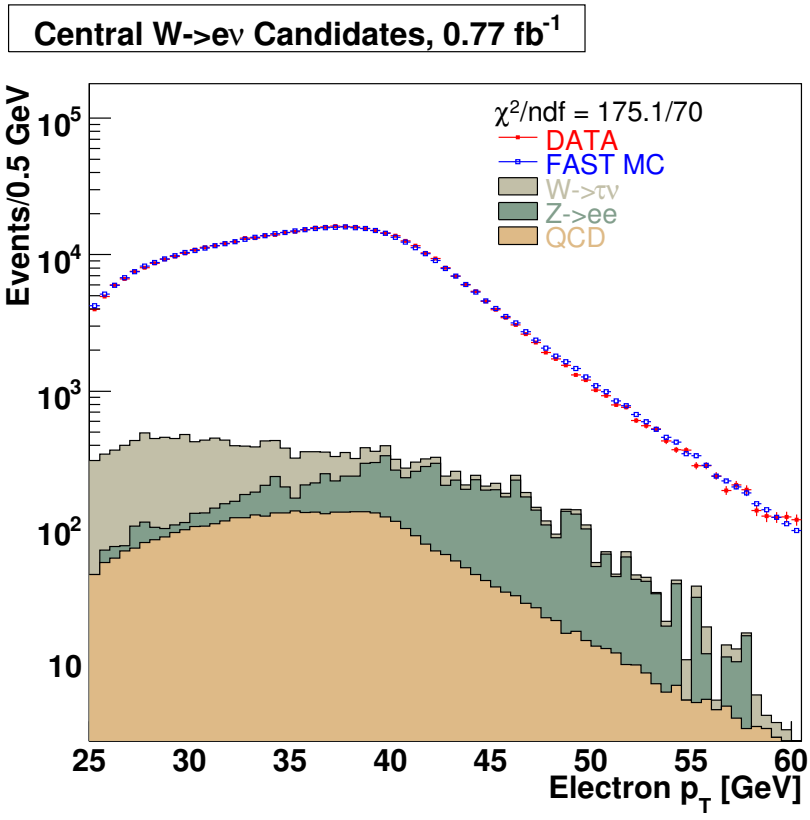


Figure 7.1. The electron p_T distribution in W events with backgrounds added to the PMCS prediction, shown on a log scale.

(see table 7.1), and the background is shown in gray in the distributions shown in figures 7.1 for the electron transverse momentum distribution and 7.2 for the transverse mass distribution.

7.3. QCD Background

The QCD background arises from di-jet events in which one jet is mis-identified as an electron[1]. This is studied with $W \to e\nu$ and $Z \to ee$ events in data using the matrix

[1]An extensive reference for jets at DØ is [**94**].

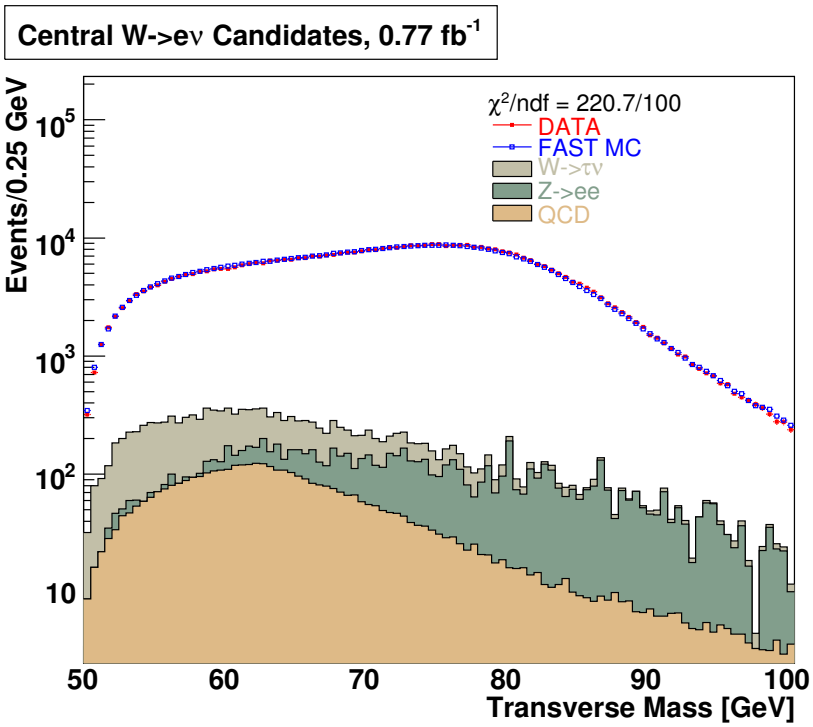


Figure 7.2. The M_T distribution for W events with backgrounds added to the PMCS prediction, shown on a log scale.

method. In the matrix method one identifies a "tight" sample of W events and a "loose" sample. Here this is done by eliminating the track match requirement of the electron in the loose sample. Then we can use

$$\begin{aligned} N &= N_W + N_{QCD} \\ N_{trk} &= \epsilon_{trk} N_W + f_{QCD} N_{QCD} \end{aligned} \tag{7.1}$$

where N and N_{trk} are the total number of W events with and without the track match requirement, N_W is the actual number of W events and N_{QCD} is the number of QCD events before the track match requirement. ϵ_{trk} is the track matching efficiency and f_{QCD} is the probability that a QCD event will have a fake track match.

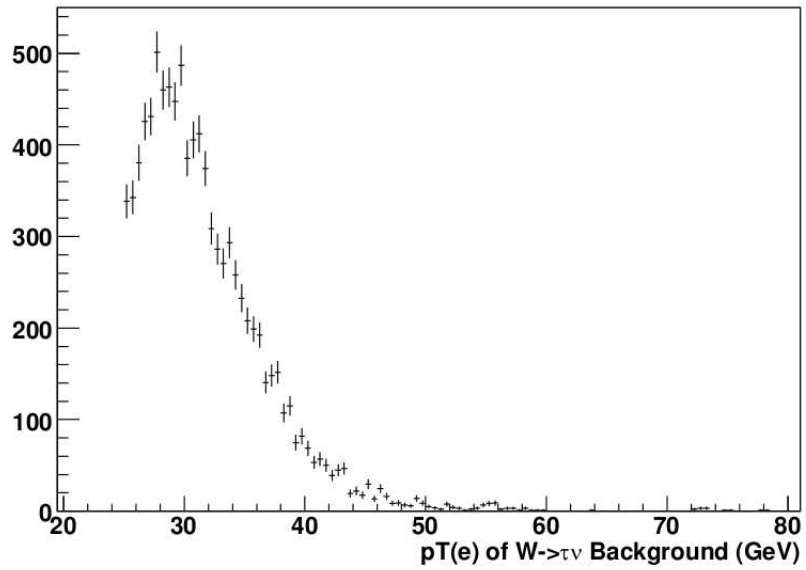


Figure 7.3. The electron p_T distribution for $W \rightarrow \tau\nu \rightarrow e\nu\nu\nu$. The Jacobian peak is no longer at $M_W/2$ in this four-body decay.

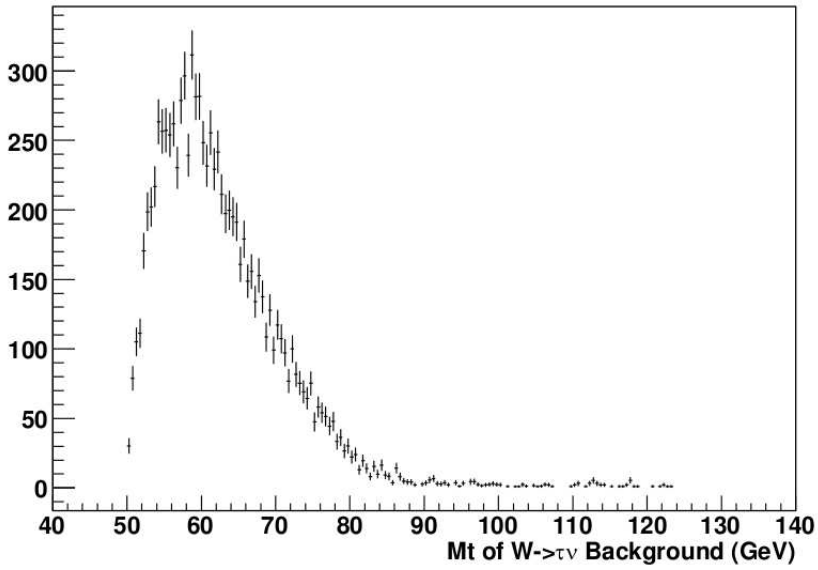


Figure 7.4. The M_T distribution for $W \rightarrow \tau\nu \rightarrow e\nu\nu\nu$. The Jacobian peak is no longer at M_W in this four-body decay.

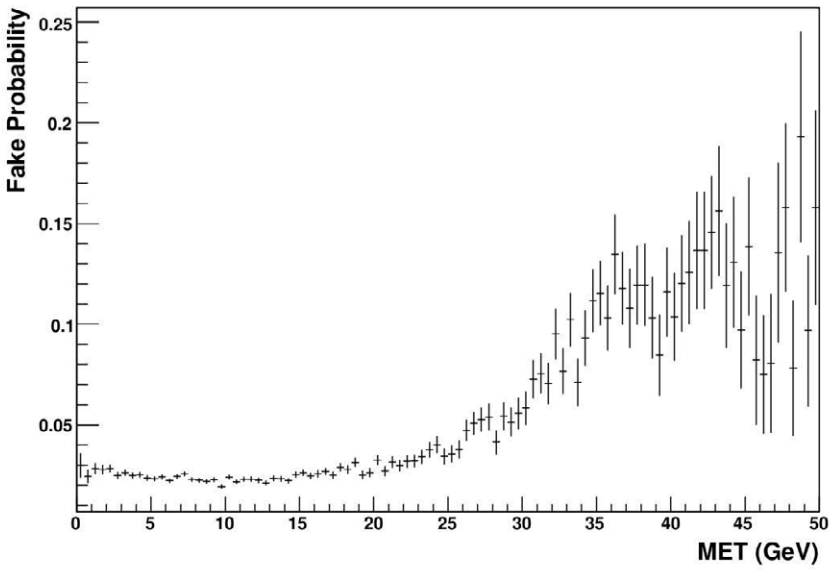


Figure 7.5. The probability that a jet will fake an electron as a function of $\not\!\!E_T$. The region $\not\!\!E_T < 15$ GeV is used in determining the QCD background.

The track match efficiency is studied in $Z \rightarrow ee$ events using the tag-and-probe method described previously. The probability that a QCD event will have a fake track match is studied using a sample that has an EM cluster which passes the electron ID requirements and is back-to-back with a jet. In this sample the electron can be a misidentified jet from a di-jet event. We determine the fake probability by checking to see if the EM object has a matched track. Figure 7.5 shows the fake probability as a function of $\not\!\!E_T$. After ~ 20 GeV as the $\not\!\!E_T$ increases the probability increases. These are frequently electrons from actual $W \rightarrow e\nu$ events. To ensure that we only look at QCD events we require $\not\!\!E_T < 15$ GeV, where f_{QCD} is nearly flat, and measure $f_{QCD} = 0.0224 \pm 0.0002$, where the uncertainty is statistical only.

To determine the QCD background the standard $W \rightarrow e\nu$ selection is applied with and without a track match. Then within each bin of the distributions the number of

background QCD events is calculated using the matrix method. We find a fraction of 1.0 ± 0.03 % (see table 7.1), and this background is shown in gold in the distributions shown in figures 7.1 for the electron transverse momentum distribution and 7.2 for the transverse mass distribution.

7.4. Uncertainties

The background uncertainty is propagated to the W mass measurement by varying each bin of the background distributions $\pm 1\sigma$ simultaneously. The new background distribution is added to the templates from PMCS. 100 pseudo-experiments are run and the difference between the value of the W mass determined by the fit using the default backgrounds and the new background is plotted in a distribution, the width of which is taken as the uncertainty on the W mass due to the uncertainty in the background. This is summarized in table 7.1 for the W mass found using the transverse mass, transverse momentum of the electron and $\not\!\!E_T$ distributions.

CHAPTER 8

Systematic Uncertainties

In this chapter we present the theoretical and experimental systematic uncertainties on the W mass measurement. In general the uncertainties are determined using a large ensemble of pseudo-experiments simulated with PMCS. Pseudo-experiments are generated in which a given parameter is varied individually $\pm 1\sigma$ and $\pm 2\sigma$ while holding all other parameters constant. M_W is then determined using a standard template fit. The difference between the true value of M_W and the new value resulting from varying the parameter is determined. M_W is estimated to change linearly with respect to the parameter varied in a small region around the parameter's central value. The change in M_W with respect to the change of the parameter is fit to a line and the slope of the line is used in the usual error propagation formula:

$$\sigma^2_{M_W}(X) = \left(\frac{\partial M_W}{\partial X}\right)^2 \sigma^2_X, \tag{8.1}$$

where $\frac{\partial M_W}{\partial X}$ is the slope and σ_X is the uncertainty on parameter X. This formula does not include correlations and in many cases we can safely assume the parameters are nearly uncorrelated. Where the is not true the more correct formula is (here for just two parameters. The extension to three or more parameters is straightforward.):

$$\sigma^2_{M_W}(X) = \left(\frac{\partial M_W}{\partial X_1}\right)^2 \sigma^2_{X_1} + \left(\frac{\partial M_W}{\partial X_2}\right)^2 \sigma^2_{X_2} + 2\sigma^2_{12} \left(\frac{\partial M_W}{\partial X_1}\right) \left(\frac{\partial M_W}{\partial X_2}\right) \tag{8.2}$$

where σ_{12} is the covariance found using the error matrix.

Where possible we make use of the fact that many of the uncertainties cancel in measuring the ratio of M_W/M_Z. We define the ratio of the masses to be

$$R_{meas} = \frac{W_{meas}(\vec{x})}{Z_{meas}(\vec{x})} \tag{8.3}$$

where $\vec{x}$ can be many parameters, assuming the different parameters x_i are uncorrelated. For now we examine only the single parameter x. Near the central value x_0 we can write the functions as a series about $x = x_0$

$$W_{meas}(x) = W(x_0) + (x - x_0)W'(x_0) + \mathcal{O}(x - x_0)^2 + \cdots \tag{8.4}$$

$$Z_{meas}(x) = Z(x_0) + x - x_0)Z'(x_0) + \mathcal{O}(x - x_0)^2 + \cdots \tag{8.5}$$

where W_{meas} is the measured mass at a particular parameter value, x is the parameter value and W' is $\frac{\partial W}{\partial x}$. Recall that $W_{meas}(x_0) = W^0$ and $Z_{meas}(x_0) = Z^0$, where W^0 is the "correct" value of the mass (and likewise for Z). Using these expansions we find the ratio is

$$R_{meas} \approx R^0 \left[1 + (x - x_0)\left(\frac{W'}{W^0} - \frac{Z'}{Z^0}\right)\right] \tag{8.6}$$

where $R^0 = \frac{W^0}{Z^0}$. Our observable is $W_{meas} = R_{meas}Z^0$. To find the uncertainty for a given parameter using 8.1 we need

$$\frac{\partial W_{meas}}{\partial x} \approx R^0 Z^0 \left(\frac{W'}{W^0} - \frac{Z'}{Z^0}\right) \tag{8.7}$$

assuming $\frac{\partial^2 W}{\partial x^2} \ll \frac{\partial W}{\partial x}\delta x$ and $\frac{\partial^2 Z}{\partial x^2} \ll \frac{\partial Z}{\partial x}\delta x$. Using this and σ_x in equation 8.1 we can calculate $\sigma_{W_{meas}}$, the contribution of the uncertainty on parameter x to the uncertainty in the measured W mass. This method is particularly useful in the calculation of uncertainties due to parameters that effect M_W and M_Z roughly equally. An example is the uncertainty due to the non-linearity of the electron energy (derived from our understanding of the detector material). Counter examples are uncertainties related to the recoil system. Here the cancellation of uncertainties is much smaller because M_Z is relatively insensitive to the recoil.

8.1. Theoretical

8.1.1. Parton Distribution Functions

The need for assessing an uncertainty due to the parton distribution functions (PDF) used in the event generation was discussed in chapter two. To reiterate, the PDF are derived from the fitting experimental results. The uncertainties on the experimental results must by propagated to the PDF and then to the W mass measurement. This measurement uses the PDF determined by the CTEQ collaboration, referred to as the CTEQ6.1 PDF [**46**]. The collaboration describes a method and provides tools for the uncertainty propagation [**47**]. Briefly, the fit for the PDF involves twenty nearly independent parameters. CTEQ provides forty PDF sets, in addition to the central PDF. In each of these forty sets one parameter has been varied either up or down by a certain tolerance (the tolerance is designed to be statistically similar to the 90% confidence limit). By fitting for the mass in psuedo-experiments created with PMCS using each of these forty PDF sets, and then comparing the difference between the value of M_W found with a particular set and

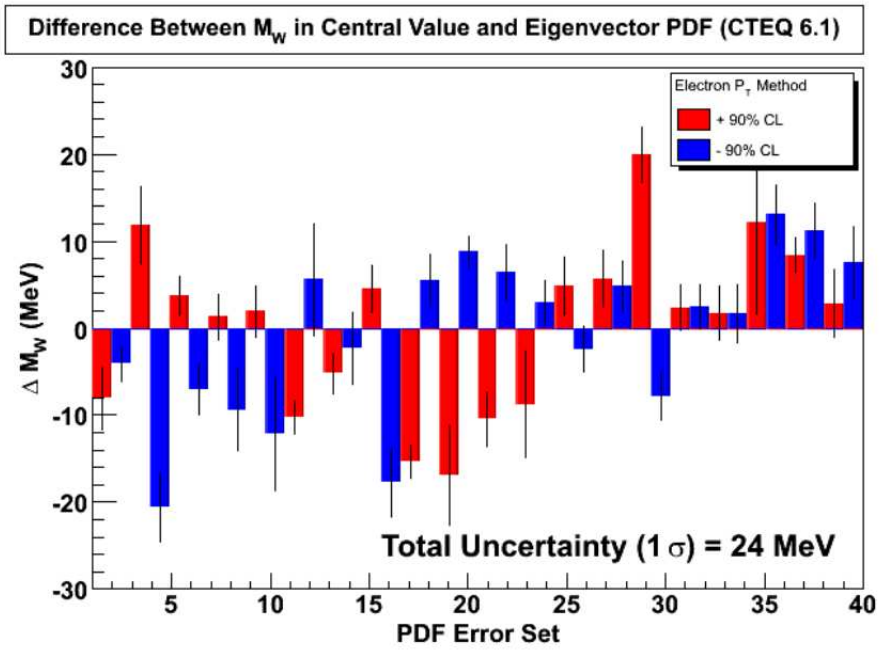


Figure 8.1. The electron p_T uncertainty due to the PDF. Each pair of red and blue columns is a single eigenvector varied up or down 1σ in parameter space.

the central value, we can assess an overall uncertainty. The formula for summing the uncertainties is: [**47**]

$$\sigma_{M_W} = \frac{1}{1.6}\frac{1}{2}\sqrt{\sum_{i=1}^{N}\left(M_i^{(+)} - M_i^{(-)}\right)^2} \tag{8.8}$$

where we divide by 1.6 in order to translate this 90% tolerance to a 1 σ uncertainty. It should be noted that this propagation was done (as are all the PMCS studies) using the next-to-leading order Resbos generator. The change in the W mass for each parameter is shown in figures 8.1 and 8.2 using the transverse momentum of the electron and the transverse mass respectively. The red and blue pairs are a single parameter varied either up or down 1σ, where the horizontal axis is the change in the W mass.

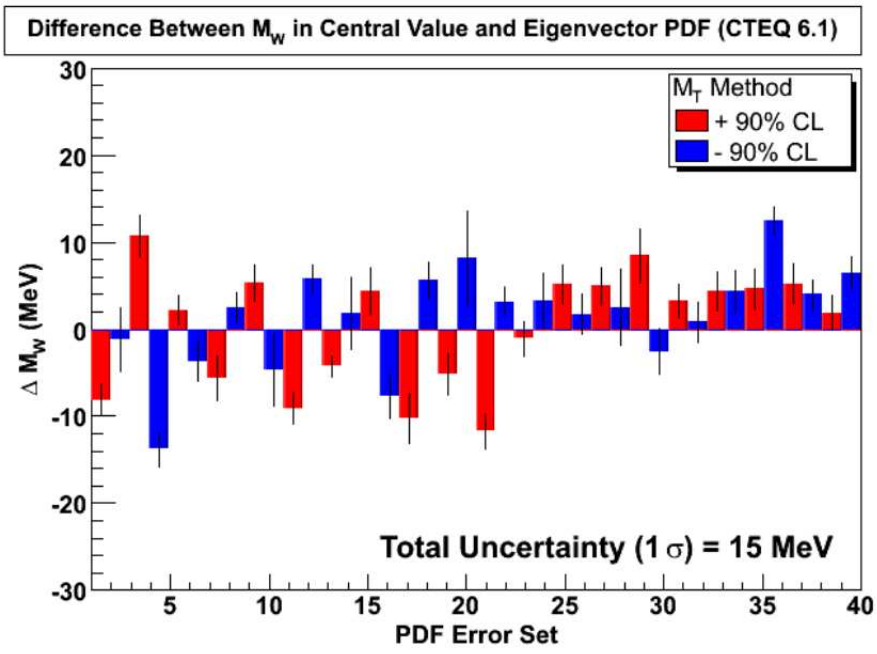


Figure 8.2. The M_T uncertainty due to the PDF. Each pair of red and blue columns is a single eigenvector varied up or down 1σ in parameter space.

The contribution to the mass uncertainty is 24 MeV for the measurement with the electron transverse momentum and 15 MeV for the transverse mass. Updated fits of the PDF with additional data could reduce this uncertainty; at present it is the leading uncertainty from our theoretical description of W boson production.

8.1.2. W and Z Boson p_T

The uncertainty due to the theoretical description of the transverse momentum spectrum of the boson is found to depend most significantly on the value of g_2 in the BLNY parametrization of the non-perturbative region of the spectrum (described in chapter two and [**51**]). The value of g_2 determines the most likely boson p_T. Using the Z boson p_T spectrum g_2 is determined to be consistent with the value found in the global fits [**52**].

We use the global fit value of 0.68 ± 0.02 [**51**] and propagate this uncertainty to the W mass measurement. We find an uncertainty of 2 MeV when using the transverse mass distribution and 5 MeV when using the electron p_T. It is likely that the g_2 value and its uncertainty will be re-examined in future analyses at DØ .

8.1.3. Photon Radiation

The Resbos generator neglects higher order QED processes, such as ISR-FSR interference and W and Z self-energy box diagrams. The WGRAD and ZGRAD programs [**95**], though not actually event generators, are used to calculate the cross-sections for these processes. To determine how this influences the measurement of the W mass we vary the photon energy cut and the width of the photon merging cone. We find the the uncertainty contribution to the W mass measured with the electron transverse momentum distribution to be 10 MeV and with the transverse mass it is 8 MeV [**96**].

8.1.4. W Width

The shape of the mass distribution depends on the width, as can be seen in 2.31. The W width is predicted by the SM to be 2094 ± 2 MeV. The derivative of the W mass with respect to W width is 1.51 for the mass measured with the electron transverse momentum and 0.64 for the transverse mass. Using the SM uncertainty on the width the uncertainty contribution to the W mass is negligible.

8.2. Experimental

8.2.1. Electron Energy Scale

The dominant uncertainties in the W mass measurement is derived from the precision with which we understand the electron energy. The uncertainty on the energy scale and offset are individually large (see chapter five). However, these parameters are highly negatively correlated in the fit, as is clear from the "tilt" of the error ellipse in figure 5.3.3.2. Using this correlation in the uncertainty propagation we find a significant degree of cancellation. Overall, the uncertainty due to the electron energy measurement is found to be 29 MeV, using either the transverse mass or electron p_T distributions.

8.2.2. Electron Energy Non-linearity - Detector Material Understanding

The precision with which we have measured the material in front of the detector contributes directly to energy measurement of the electron and therefore to the W mass. This measurement of M_W using the ratio of M_W/M_Z depends critically on the assumption that we can scale the calibration and tuning done at the Z mass down to the W mass. A mis-measured material distribution would be the primary source of a non-linearity in this scaling. The determination of this contribution to the uncertainty on the mass is complicated by the fact that the material is measured and then used in the calibration and reconstruction of electrons, not just in the tuning of the PMCS. In this case we still use PMCS pseudo-experiments, but we "undo" the standard energy loss corrections that were determined with for a particular amount of material X_0, and then apply energy loss corrections for $\pm 1\sigma_{\Delta n X_0}$. This is done first for $Z \rightarrow ee$ PMCS events to redetermine the EM calorimeter constant term, which is sensitive to changes in X_0. Then we generate

$W \rightarrow e\nu$ pseudo-experiments with the alternative energy loss corrections and constant term and fit for the mass. The uncertainty in the measurement of the upstream material results in a W mass uncertainty of 6 MeV when using the electron p_T distribution and 7 MeV when using the transverse mass distribution after taking into account the cancellation of uncertainty using equation 8.7.

8.2.3. Electron Energy Resolution

The uncertainty due to the electron energy resolution also requires measurement the constant term in pseudo-experiments. The sampling term of the calorimeter is parameterized as a function of X_0. As mentioned above, the constant term is correlated with the sampling term, so part of the uncertainty introduced by the sampling term will be compensated for by the determination of the constant term. The contribution is found to be small, and is conservatively estimated to be 2 MeV for both the measurement with the p_T of the electron and the transverse mass [**89**].

8.2.4. Recoil Momentum Scale and Resolution

The next significant uncertainty derives from the energy scale and resolution of the recoil. We use the parameters and uncertainties found in chapter six to propagate the uncertainty. The hard component of the recoil is the primary factor in the uncertainty of the momentum scale: 14 MeV using $p_T(e)$ and 17 MeV using M_T. The momentum resolution is affected by the soft and hard components and is 2 MeV for the $p_T(e)$ and 12 MeV for the M_T.

8.2.5. Efficiencies

The most significant efficiency related uncertainty results from the $u_{\parallel}$ efficiency. This uncertainty has two components: First, the determination of the efficiency itself from the $Z \rightarrow ee$ events, and second the scaling of this efficiency to the W events, determined using the DØ Geant detector simulation. Together the uncertainty is 11 MeV ($p_T(e)$) and 2 MeV (M_T).

8.3. Summary of Systematic Uncertainty

The systematic uncertainties are summarized in table 8.1. First are the experimental uncertainties and second are the theoretical uncertainties, both summed separately. It is interesting to note that though both methods have similar experimental uncertainties the transverse mass distribution results in substantially smaller theoretical uncertainties. Experimentally, the electron energy uncertainty is statistically limited by the number of $Z \rightarrow ee$ events, and could be significantly reduced by analyzing more data.

Source	$\sigma(M_W)$ MeV $p_T(e)$	$\sigma(M_W)$ MeV M_T
Experimental		
Electron Energy Scale	29	29
Electron Energy Nonlinearity	6	7
Electron Energy Resolution	2	2
Recoil Momentum Scale	14	17
Recoil Momentum Resolution	2	12
Efficiencies	11	2
Backgrounds	4	3
Experimental Total	35	37
Theoretical		
PDF	24	15
QED	10	8
Boson p_T	5	2
Theoretical Total	26	17

Table 8.1. Experimental and theoretical systematic uncertainties on the W boson mass measured with 770 pb^{-1} in the $W \to e\nu$ channel.

CHAPTER 9

Results and Conclusion

The W mass is determined using the transverse momentum distribution of the electron and the transverse mass distribution. The $\not\!\!E_T$ distribution is used as a cross-check. Before the final fitting of the mass an arbitrary offset was introduced [**20**]. This offset, or "blinding" was also used whenever comparing data and MC distributions that are sensitive to the mass. In this way we attempt to avoid any bias introduced by the experimenters. Before the measurement was done without the offset the complete analysis procedure was applied to a version of PMCS tuned using $Z \rightarrow ee$ events produced by Pythia and the DØ Geant detector simulation as described in chapter five. The mass was then measured in a comparable MC sample of $W \rightarrow e\nu$ events. The determination of the known W mass in the MC represented a closure test of the calibration and tuning procedure. This test was done using the equivalent of 6 fb^{-1} of Z events and 2 fb^{-1} of W events, making it a more challenging test of the detector model than is possible with the data. The closure test is described in detail in [**82**], and the successful result (with statistical uncertainties only) is shown in table 9.

9.1. Fitting Method

The template fit is performed for each of the three distributions using a binned negative log likelihood technique. The likelihood is found by calculating the product of the Poisson

	Measured Mass - MC Input [MeV]	Statistical Uncertainty [MeV]
Z Inv. Mass	7	11
W $p_T(e)$	1	15
W M_T	-5	13
W $\not\!\!E_T$	9	15

Table 9.1. The result of the MC closure test. The W boson mass was measured with MC equivalent to 2 fb^{-1} in the $W \to e\nu$ channel and the Z mass was checked with 6 fb^{-1} in the $Z \to ee$ channel .

probability for each bin, with n_i observed events and m_i expected events:

$$\mathcal{L} = \prod_{i=1}^{N} \frac{e^{-m_i} n_i^{m_i}}{n_i!}. \tag{9.1}$$

We take the logarithm of the likelihood using the approximation $\ln n! \approx (n+\frac{1}{2}) \ln n + 1 - n$:

$$\ln \mathcal{L} \approx \sum_{i=1}^{N} \left(n_i \ln m_i - m_i \right). \tag{9.2}$$

Using Minuit [**68**] we find the mass that minimize $-\ln \mathcal{L}$, and the $\pm 1\sigma$ values that increase $-\ln \mathcal{L}$ by 0.5.

The templates are spaced 10 MeV apart and splining is used for interpolation [**87**]. The fit is done with in the ranges of 32 GeV $< p_T(e) <$ 48 GeV, 65 GeV $< m_T <$ 95 GeV and 32 GeV $< \not\!\!E_T <$ 48 GeV, where the histograms have four bins per GeV in the M_T distribution and two bins per GeV in the $p_T(e)$ and $\not\!\!E_T$ distributions.

9.2. Fitting the Distributions

We first examine the electron transverse momentum distribution shown in figure 9.1 over a range somewhat greater than is used in fitting. The $\chi^2/ndf = 68/32$ within the fit

range is significantly worse than one would hope. Fitting we find the blinded mass to be 79308 ± 23 (stat) MeV.

The blinded mass measured in the transverse mass distribution is 79328 ± 19 (stat) MeV. The distribution is shown in figure 9.2. Here the $\chi^2/ndf = 88/60$ within the fit range, which though not unacceptable, is not as good expected. However, the mass measured with the the M_T distribution agrees with the mass measured with the $p_T(e)$ distribution.

Finally, the mass measured using the $\not\!\!E_T$distribution is found to be 79418 ± 20 (stat) MeV, as seen in figure 9.3. The predicted distribution does not agree well with the data, and though only a cross-check this distribution indicates problems with the parameterized model.

These three results lead one to conclude that this selection of events is not tuned acceptably for removing the blinding and measuring the mass, particularly in conjunction with the known difficulties in the $u_\parallel$ distribution (fig. 9.4). However, the $u_\parallel$ distribution does point the way to a solution. The $W \rightarrow e\nu$ events are significantly more difficult to reconstruct and model at $u_\parallel > 0$ GeV, where the recoil and electron systems overlap. It is possible to split the sample into two, one for $u_\parallel > 0$ GeV and another for $u_\parallel < 0$ GeV. Naturally this will increase the statistical uncertainty.

With the split samples we examine the key distributions separately. We return to the W boson transverse momentum distribution. For all events it was found to agree well with the data, as seen in figure 9.5. Selecting only $u_\parallel > 0$ GeV in figure 9.6 we find a significant discrepancy between data and PMCS. Again, $u_\parallel > 0$ GeV is the region more difficult to model and given the other distributions it is not surprising that this is not

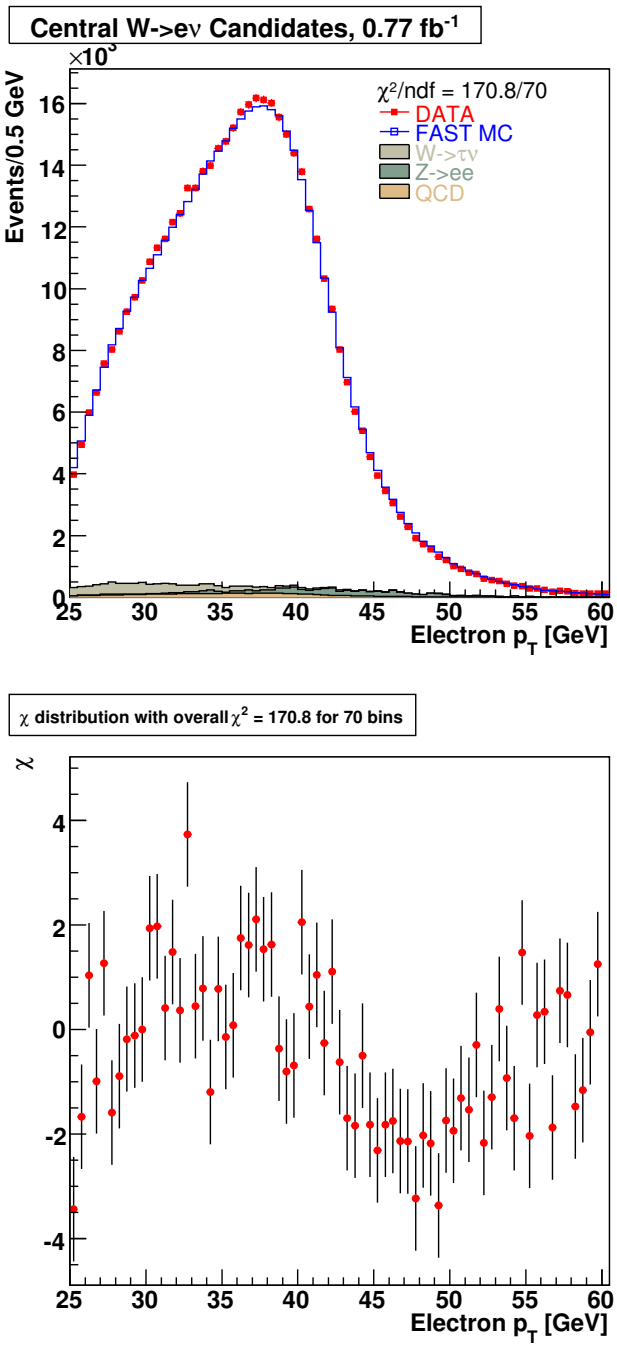


Figure 9.1. The electron p_T distribution in $W \rightarrow e\nu$ events with backgrounds added to the templates. The fitting range is 32 GeV $< p_T(e) <$ 48 GeV.

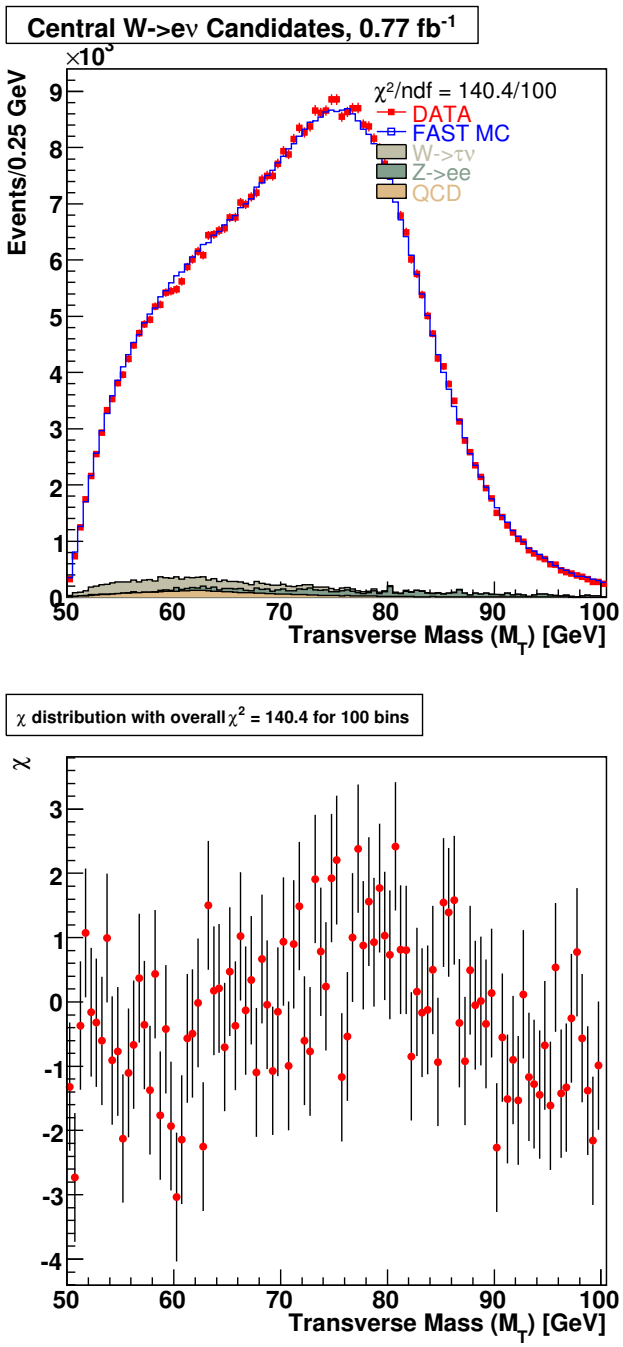


Figure 9.2. The M_T distribution for $W \rightarrow e\nu$ events with backgrounds added to the templates. The fitting range is 65 GeV $< M_T <$ 95 GeV.

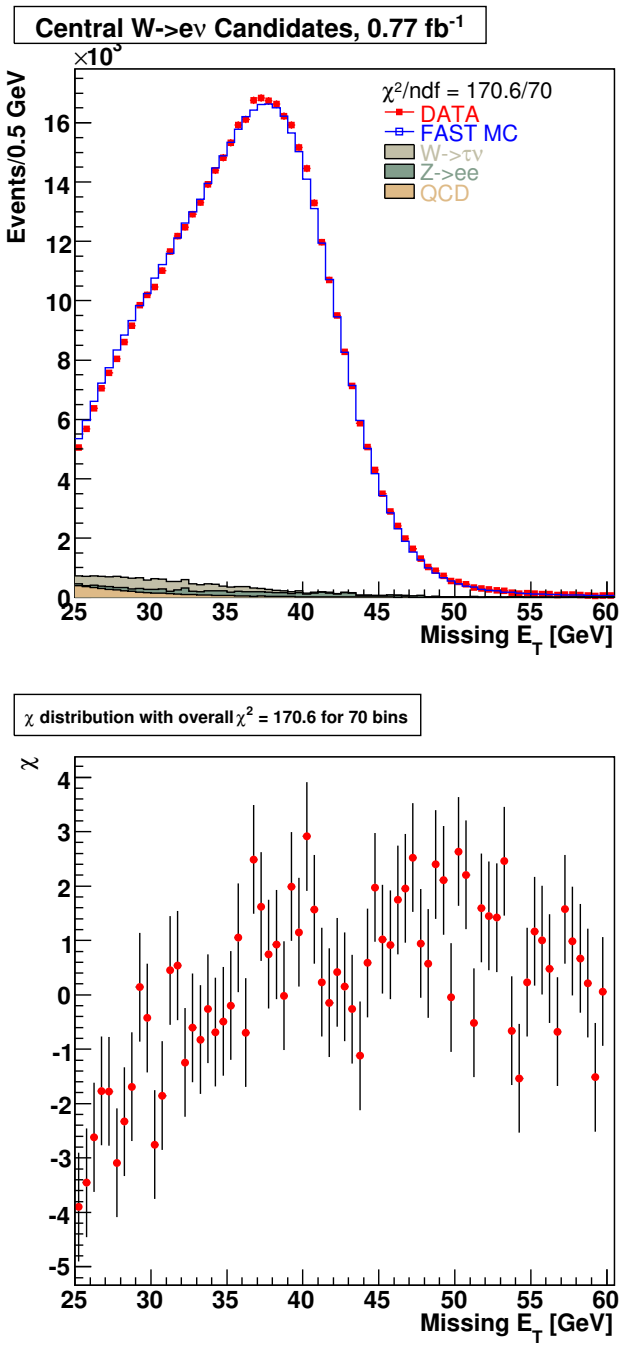


Figure 9.3. The $\not\!\!E_T$ distribution for $W \rightarrow e\nu$ events with backgrounds added to the templates. The fitting range is 32 GeV $< \not\!\!E_T <$ 48 GeV.

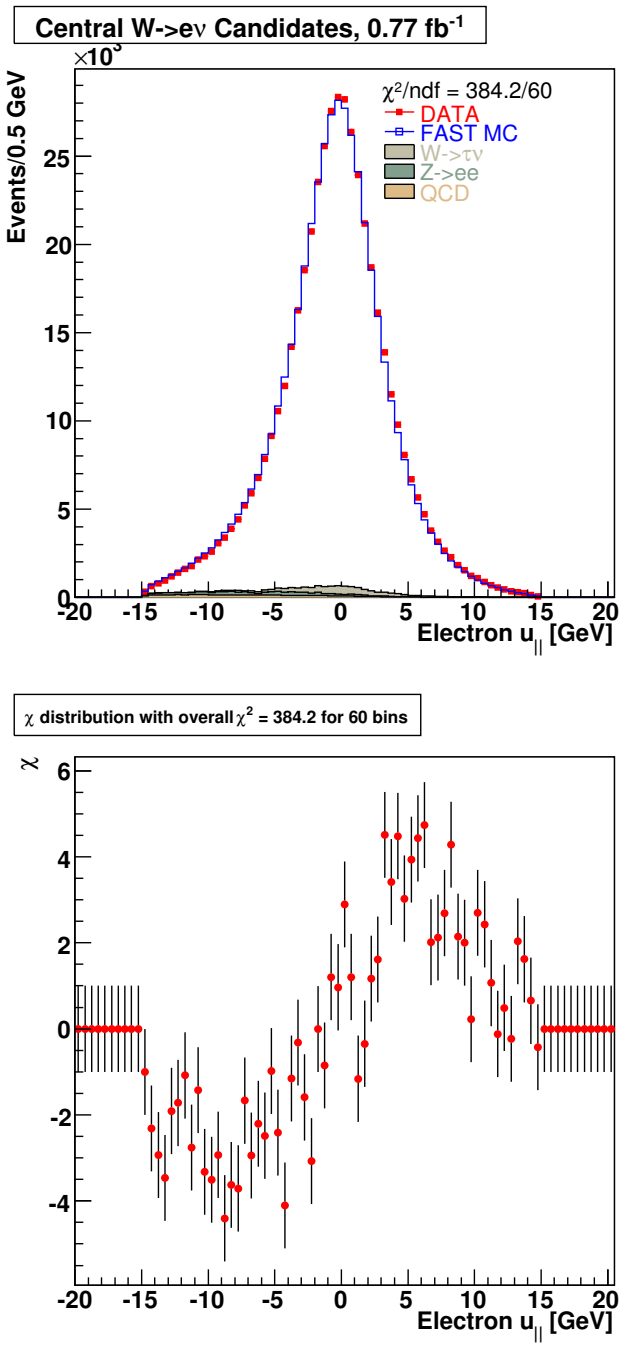


Figure 9.4. The W $u_{\parallel}$ distribution in data and PMCS.

	$p_T(e)$ [MeV]	M_T [MeV]
All $u_\parallel$	79308 ± 23	79328 ± 19
$u_\parallel < 0$ GeV	79246 ± 37	79267 ± 28
$u_\parallel > 0$ GeV	79556 ± 26	79420 ± 25

Table 9.2. W Mass (blinded) measured with the electron p_T and boson M_T distributions using different $u_\parallel$ selections.

as well described. Comparing to the $u_\parallel < 0$ GeV selection for the W boson transverse momentum distribution in figure 9.7 we find much better agreement. This agreement was hiding the poor agreement at $u_\parallel > 0$ GeV in the combined sample. The W p_T distribution and the $u_\parallel$ distributions indicate that it is necessary, for the present analysis, to select only events with $u_\parallel < 0$ GeV.

The electron transverse momentum and boson transverse mass distributions for $u_\parallel$ less than and greater than zero are shown in figures 9.8, 9.9, 9.10 and 9.11. In general, when separated in this manner the χ^2/ndf for these distributions indicates good agreement between the data and PMCS predictions. However, in table 9.2 we show the fit for the blinded mass for each of these four selections. For the $u_\parallel < 0$ GeV selection the blinded mass agrees again in either the electron p_T or the M_T distributions. For $u_\parallel > 0$ GeV the agreement disappears. We again conclude that the measurement of the mass after requiring $u_\parallel < 0$ is less sensitive to the modeling, i.e. more model-independent. Table 9.2 also includes the statistical uncertainties. The larger statistical uncertainty does not overwhelm the systematic uncertainties and is an acceptable cost for the more accurately described events.

It must be noted that the systematic uncertainties were determined without the selection of $u_\parallel < 0$. The most significant uncertainties were re-estimated with this selection,

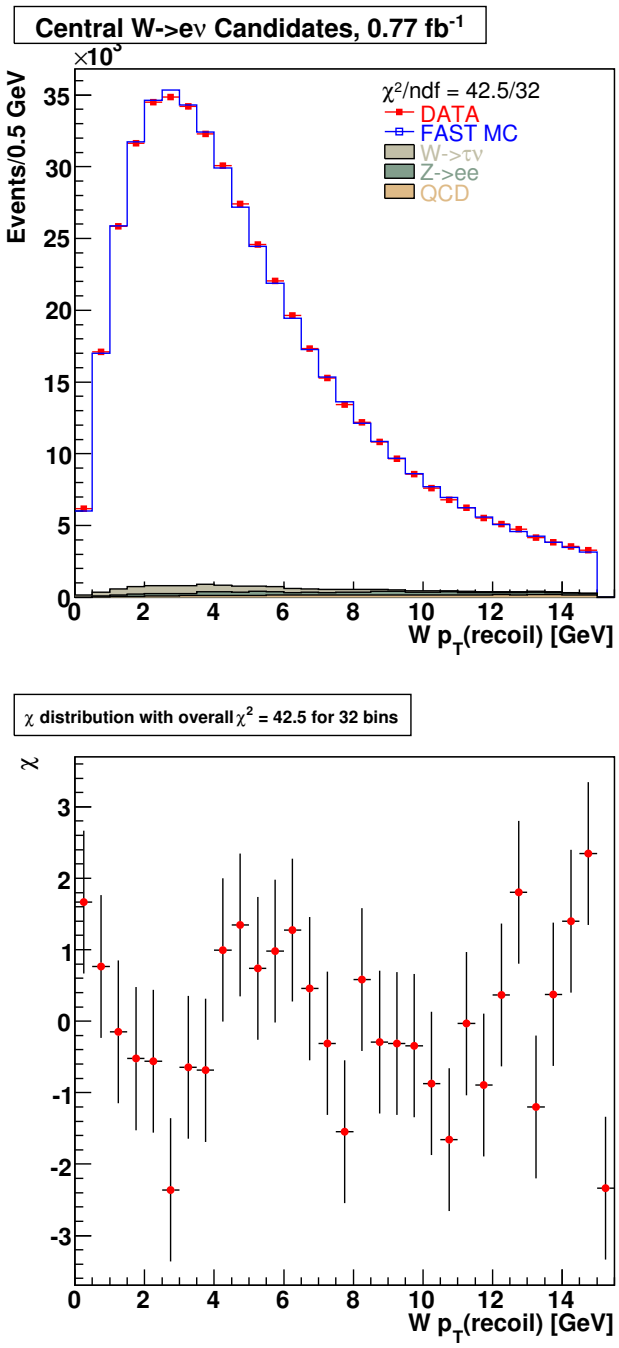


Figure 9.5. The W boson p_T distribution for $W \rightarrow e\nu$ events with backgrounds added to the templates for all $u_{\parallel}$.

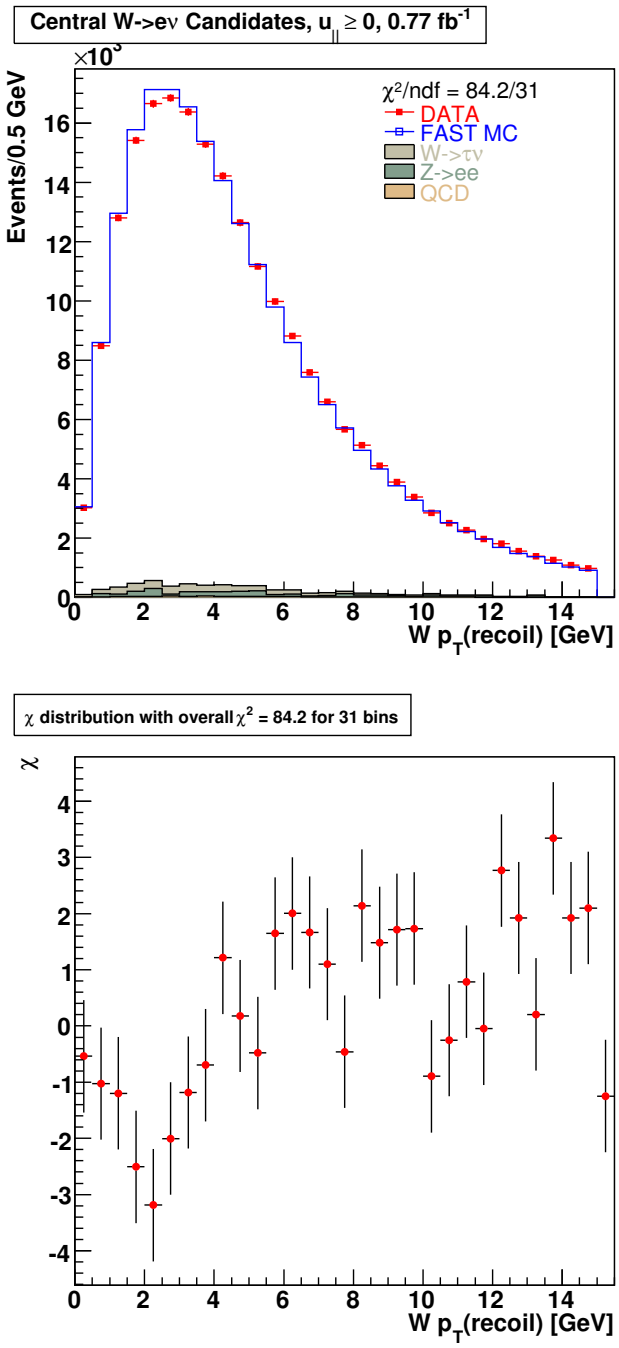


Figure 9.6. The W boson p_T distribution for $W \rightarrow e\nu$ events with backgrounds added to the templates and $u_{\parallel} > 0$ GeV. The agreement between the data and the prediction is poor.

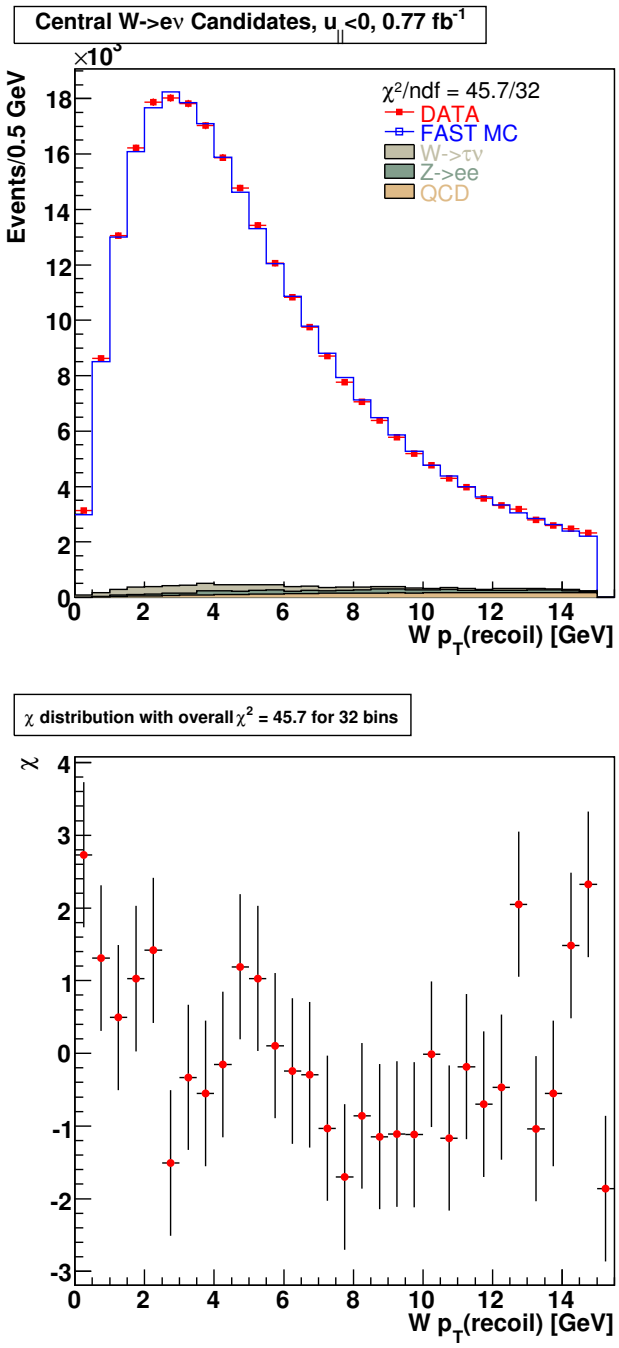


Figure 9.7. The W boson p_T distribution for $W \rightarrow e\nu$ events with backgrounds added to the templates and $u_{\parallel} < 0$ GeV. The agreement between the data and the prediction is reasonable, indicating that the $u_{\parallel} < 0$ GeV is the better modeled selection of events.

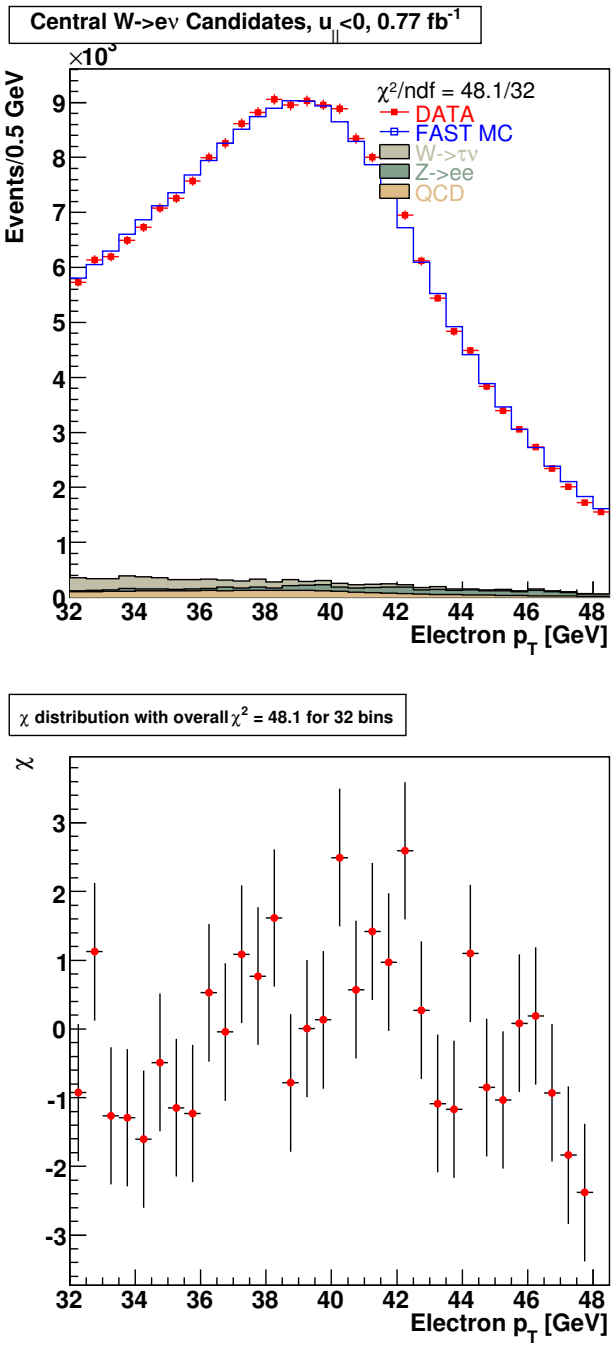


Figure 9.8. The electron p_T distribution in $W \rightarrow e\nu$ events with backgrounds added to the templates and $u_{\parallel} < 0$ GeV selected.

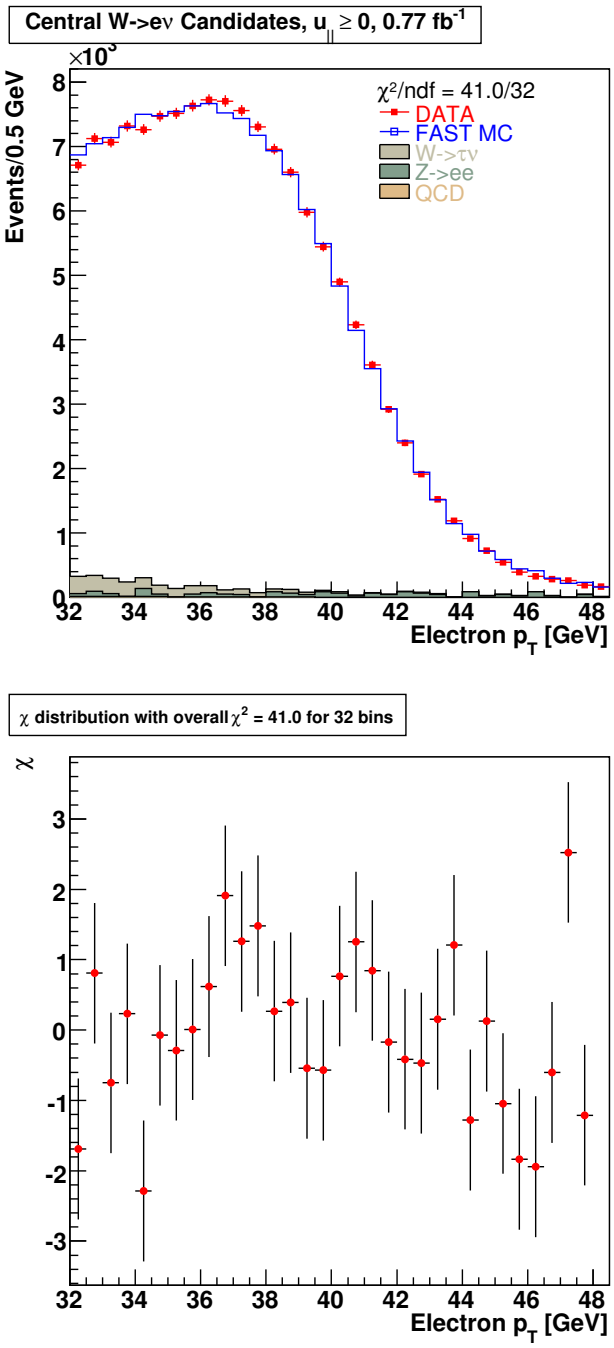


Figure 9.9. The electron p_T distribution in $W \rightarrow e\nu$ events with backgrounds added to the templates and $u_{\parallel} > 0$ GeV selected

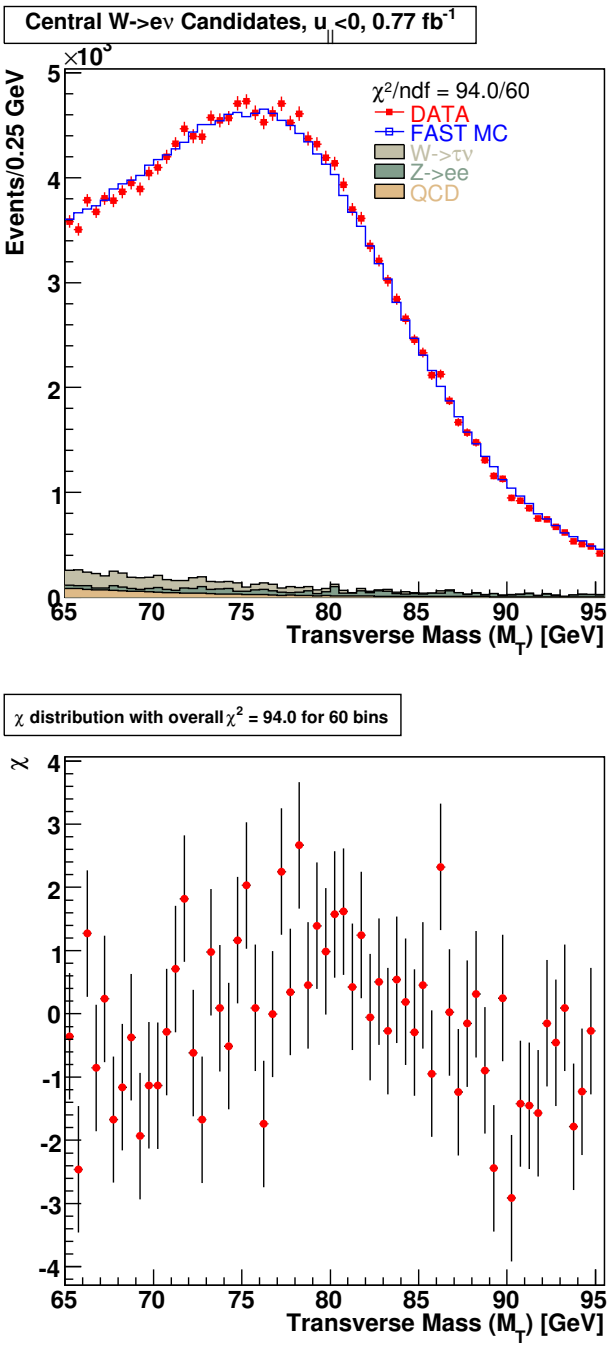


Figure 9.10. The M_T distribution for $W \rightarrow e\nu$ events with backgrounds added to the templates and $u_{\parallel} < 0$ GeV selected.

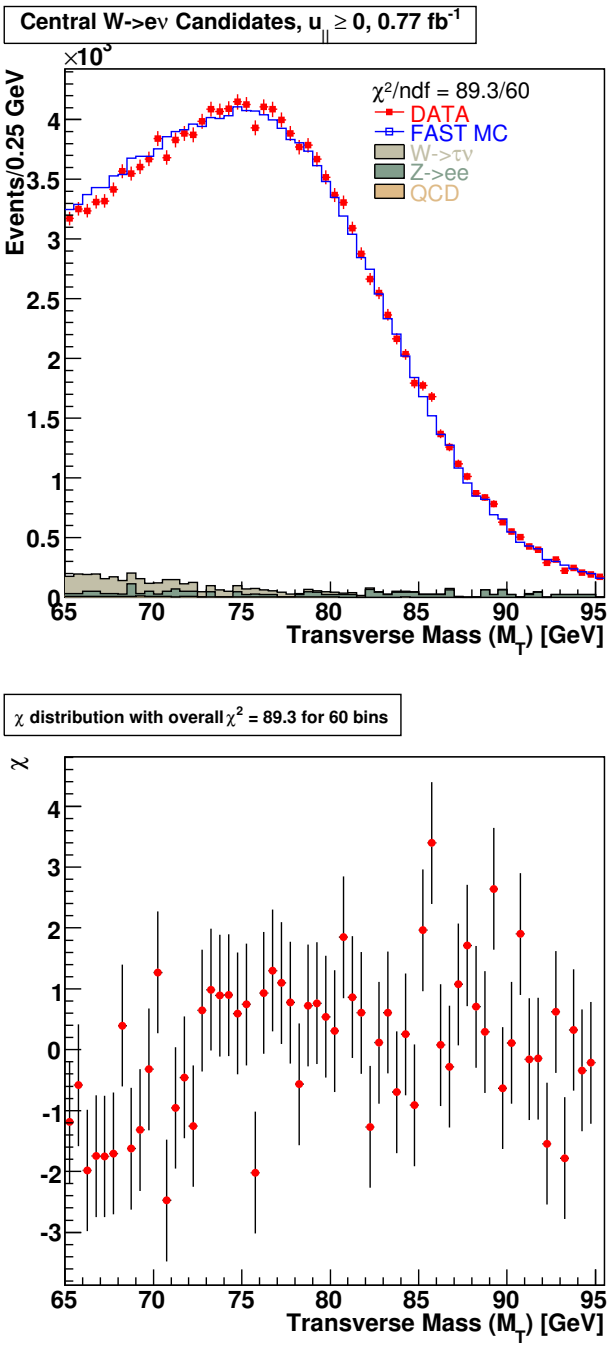


Figure 9.11. The M_T distribution for $W \rightarrow e\nu$ events with backgrounds added to the templates and $u_{\parallel} > 0$ GeV selected.

Source	$\sigma(M_W)$ MeV $p_T(e)$	$\sigma(M_W)$ MeV M_T
Experimental		
Electron Energy Scale	31	32
Recoil Momentum Scale	40	37
Efficiency ($u_\parallel$)	5	4

Table 9.3. Experimental systematic uncertainties on the W boson mass measured with 770 pb^{-1} in the $W \to e\nu$ channel and with the additional selection of $u_\parallel < 0$ GeV. The results are significantly different (particularly with regard to the recoil) than those without this selection.

and are summarized in table 9.2. The changes were minimal with regard to the electron system, but in the recoil system the effect is quite large. This is because the we have introduced an additional dependence on the recoil simulation through the $u_\parallel$ selection. It is clear that it would be important to re-estimate all the experimental uncertainties, but it is likely that the recoil system is the most sensitive to the change in the selection. The uncertainty due to the $u_\parallel$ efficiency was reduced because we have eliminated the data that was most affected.

9.3. W Mass Measurement

We chose to use the $u_\parallel < 0$ GeV selection to measure M_W. This choice was made before removing the blinding. The electron transverse momentum and transverse mass distributions in the $W \to e\nu$ channel are now used to measure M_W without the blinding. Using the transverse momentum of the electron distribution we determine the mass to be

$$\begin{aligned} M_W &= XXXXX \pm 37 \text{ (stat.)} \pm 26 \text{ (sys. theo.)} \pm 51 \text{ (sys. exp.) MeV} \\ &= XXXXX \pm 68 \text{ MeV} \end{aligned} \tag{9.3}$$

and with the transverse mass distribution

$$\begin{aligned} M_W &= XXXXX \pm 28 \text{ (stat.)} \pm 17 \text{ (sys. theo.)} \pm 51 \text{ (sys. exp.) MeV} \\ &= XXXXX \pm 61 \text{ MeV}. \end{aligned} \tag{9.4}$$

This measurement is more precise than the previous measurement done at DØ which found $M_W = 80483 \pm 84$ MeV [**15**]. [...Discussion removed...] The uncertainty is an estimate derived from a combination of using and not using the $u_{\parallel}$ selection, and should be understood to be approximate.

We also report the mass measured with the full selection. With the transverse momentum of the electron distribution the mass is

$$\begin{aligned} M_W &= XXXXX \pm 23 \text{ (stat.)} \pm 26 \text{ (sys. theo.)} \pm 35 \text{ (sys. exp.) MeV} \\ &= XXXXX \pm 49 \text{ MeV} \end{aligned} \tag{9.5}$$

and with the transverse mass distribution

$$\begin{aligned} M_W &= XXXXX \pm 19 \text{ (stat.)} \pm 17 \text{ (sys. theo.)} \pm 37 \text{ (sys. exp.) MeV} \\ &= XXXXX \pm 45 \text{ MeV}. \end{aligned} \tag{9.6}$$

In this case the uncertainties are determined consistently, but the problem with $u_{\parallel}$ means that we may have neglected an unknown uncertainty. Until we fully understand the discrepancy between the transverse mass and electron transverse momentum methods for $u_{\parallel} > 0$ GeV we prefer to quote the restricted $u_{\parallel} < 0$ GeV as the primary result.

9.4. Future Prospects

Clearly it is of the utmost importance to fully understand the modeling of the events $u_{\parallel} > 0$ GeV. By doing this it may be possible for DØ to make the worlds most precise single measurement of the W mass. Aside from this, the significant limiting factor of the measurement of the W mass is the calibration and tuning of the electron energy. This is done primarily by using the $Z \rightarrow ee$ events, of which there are approximately factor of 10 fewer than W events at the cross-sections for production at $\sqrt{s} = 1.96$ TeV. With the addition of data which has already been collected by DØ and is awaiting analysis it should be possible to reduce the systematic uncertainty by a factor of two over the next several years. The combination of the final analyses done at DØ and CDF with $\sim 8\text{fb}^{-1}$ will further reduce the uncertainty. The use of less traditional techniques, such as the "transform" method [**97**] in which the Z events are used to directly create templates for fitting the W distributions, may also decrease the uncertainty. This brings one close to the point where further improvement is limited only by the theoretical description of the partons. It is expected that this will also be a limiting factor for the W mass measurement at the LHC experiments[1], which is scheduled to begin collecting data later this year (2008). However it remains to be seen whether the electron energy and hadronic recoil can be understood with the precision necessary in the high luminosity environment of the LHC, despite the increase in the W and Z boson cross-sections with collisions at $\sqrt{s} = 14$ TeV. In the longer term a linear electron collider (such as the proposed International Linear Collider) could be used to measure the W mass with extraordinary precision, being aided by an insensitivity to the understanding the parton model and

[1]The Large Hadron Collider is a future pp collider at CERN with two experiments larger than, but similar to, DØ and CDF.

having an extremely clean interaction environment. This remains at least a decade away and there are compelling reasons to hope that there are new and exciting particle physics phenomena to be discovered in the interim.

References

[1] D. Griffiths, *Introduction to Elementary Particles*, Heppenheim, Germany: Wiley-VCH, (2004).

[2] I. Aitchison, A. Hey, *Gauge Theories in Particle Physics, Vols. 1 and 2*, Philadelphia: IOP Publishing, (2004).

[3] S. Glashow, *Partial-Symmetries of Weak Interactions* Nuclear Physics, **22**, 579, (1961).

[4] S. Weinberg, *A Model of Leptons*, Physical Review Letters, **19** 1264, (1967).

[5] A. Salam *et. al*, *Electromagnetic and Weak Interactions*, Physics Letters **13**, 168 (1964).

[6] G. Arnison *et. al*, *Experimental Observation of Isolated Large Transverse Energy Electrons with Associated Missing Energy at* $\sqrt{(s)} = 540 \;\; GeV$, Physics Letters B, **122**, 103, (1983).

[7] M. Banner *et. al*, Physics Letters B, **122**, 476, (1983).

[8] P. Higgs, *Broken Symmetries and the Masses of the Gauge Bosons*, Physical Review Letters, **13**, 508, (1964).

[9] F. Englert, R. Brout, Physical Review Letters, **13**, 321 (1964).

[10] S. Heinemeyer *et. al*, hep-ph/0604147, hep-ph/0412214; A. Djouadi *et. al*, Physical Review Letters, **78**, 3626, (1997); Physical Review D **57**, 4179, (1998); S. Heinemeyer, G. Weiglein, JHEP **10**, 72, (2002); J. Haestier *et. al*, hep-ph/0508139.

[11] V. Abazov *et. al*, *Measurement of the top quark mass in the dilepton channel*, Physics Letters B **655**, 7, (2007).

[12] V. Abazov *et. al*, *Combination of CDF and D0 Results on W Boson Mass and Width*,Physical Review D, **70**, 092008, (2004).

[13] E. Flattum, *A Measurement of the W Boson Mass in $p\bar{p}$ Collisions at $\sqrt{s} = 1.8$ TeV*, PhD Thesis, Michigan State University, East Lansing, Michigan, (1996).

[14] I. Adam, *Measurement of the W Boson Mass with the DØ Detector using the Electron E_T Spectrum*, PhD Thesis, Columbia University, New York, New York, (1997).

[15] V. Abazov *et. al*, Physical Review D, **66**, 012001, (2002); B. Abbott *et. al*, Physical Review D, **62**, 092006, (2000).

[16] T. Affolder *et. al*, Physical Review D, **64**, 052001, (2001).

[17] The LEP Electroweak Working Group, `http://lepewwg.web.cern.ch/LEPEWWG/plots/winter2008/`.

[18] T. Aaltonen *et. al*, Physical Review Letters, **99**, 151801, (2007).

[19] The ALEPH, DELPHI, L3, OPAL, SLD Collaborations, the LEP Electroweak Working Group, the SLD Electroweak and Heavy Flavour Groups, *Precision Electroweak Measurements on the Z Resonance*, Physics Reports, **427(5-6)**, 257, (2006).

[20] P. Petroff, J. Stark, *Proposal to perform a blind measurement of the W mass in Run II*, DØ Note 5388, (2007).

[21] M. Peskin, D. Schroeder, *An Introduction to Qunatum Field Theory*, New York: Westview Press, (1995).

[22] C. Quigg, *Gauge Theories Of Strong, Weak, And Electromagnetic Interactions* , New York: Westview Press, (1997).

[23] H. Georgi, *Weak Interactions and Modern Particle Theory*, San Fransico: Benjamin/Cummings, (1984) (a substantially updated version is available at `http://www.people.fas.harvard.edu/%7Ehgeorgi/weak.pdf`).

[24] C. Quigg, *The Electroweak Theory*, 3, in *Flavor Physics for the Millennium: TASI 2000*, edited by Jonathan L. Rosner. Singapore: World Scientific, (2001).

[25] C. Quigg, *Spontaneous Symmetry Breaking as a Basis of Particle Mass*, arXiv:0704.2232v2 [hep-ph], (2007).

[26] P. Langacker, J. Erler, *The Electroweak Model and Constraints on New Physics* Review of Particle Properties, `http://pdg.lbl.gov/`, (2006).

[27] W. Marciano, Z. Parsa, *Electroweak Tests of the Standard Model*, Ann. Rev. Nucl. Particles, **36**, 171, (1986).

[28] E. Commins, P. Bucksbaum, *Weak Interactions of Quarks and Leptons*, Cambridge: Cambridge University Press, (1983).

[29] P. Langacker (ed.), *Precision tests of the standard electroweak model*, Singapore: World Scientific, (1995).

[30] Image produced by Fermilab Visual Media Serives.

[31] A. Franklin, *Are There Really Neutrinos*, Cambridge, MA: Perseus, (2000).

[32] A. Pais, *Inward Bound*, New York: Oxford University Press, (1986).

[33] W. Pauli, *Rapp. Sepitème Conseil Phys. Solvay, Brussels 1933* Paris: Gautier-Villars, (1934).

[34] E. Fermi, Zeitschrift für Physik, **88**, 161, (1934).

[35] T. Lee, C. Yang, Physics Review, **104**, 254, (1956).

[36] C. Wu *et. al*, Physical Review, **105**, 1413, (1957).

[37] C. Yang, R. Mills, Physical Review, **96**, 191, (1954).

[38] J. Goldstone *et. al*, Physical Review, **127**, 965, (1962).

[39] W. Heisenberg, Zeitschrift für Physik, **77**, 1, (1932).

[40] N. Cabibbo, Physical Review Letters, **10**, 531, (1963).

[41] M. Kobayashi, K. Maskawa, Progress in Theoretical Physics, **49**, 652, (1973).

[42] A. Sirlin, Physical Review D, **22**, 971, (1980).

[43] M. Consoli, W. Hollik, F. Jegerlehner, *Electroweak Radiative Corrections For Z Physics*, LEP Physics Workshop, **1**, 7, (1989).

[44] M. Veltman, Acta Physica Polonica B, **8**, 475, (1977).

[45] P. Nadolsky, *Theory of W and Z boson production*, AIP Conf. Proc., **753**, 158, (2005).

[46] D. Stump *et. al*, *Inclusive jet production, parton distributions, and the search for new physics*, JHEP **0310**, 046, (2003).

[47] P. Nadolsky *et. al*, *Implications of CTEQ global analysis for collider observables*, arXiv:0802.0007 [hep-ph], (2008).

[48] W.-M. Yao *et. al*, *The Review of Particle Physics*, Journal of Physics G, **33**, 1 (2006).

[49] J. Zhu, *Direct Measurement of the W Boson Decay Width in Proton-Antiproton Collisions at* $\sqrt{s} = 1.96$ *TeV*, PhD Thesis, University of Maryland, College Park, Maryland (2004).

[50] J. Collins, D. Soper, G. Sternman, Nuclear Physics B, **250**, 199, (1985).

[51] F. Landry, R. Brock, P. Nadolsky, C.-P. Yuan, *Tevatron Run-1 Z boson data and Collins-Soper-Sterman resummation formalism*, Physical Review D, **67**, 073016, (2003).

[52] V. Abazov *et. al*, *Measurement of the shape of the boson transverse momentum distribution in* $p\bar{p} \rightarrow Z\gamma^* \rightarrow e^+e^- + X$ *events produced at* $\sqrt(s) = 1.96$ *TeV, 1/fb*, Physical Review Letters, **100**, 102002, (2008).

[53] E. Mirkes, J. Ohnemus, *W and Z polarization effects in hadronic collisions*, Physical Review D, **50**, 5692, (1994).

[54] U. Baur, S. Keller, D. Wackeroth, *Electroweak Radiative Corrections to W Boson Production in Hadronic Collisions*, Phys. Rev. D, **59**, 013002, (1999).

[55] J. Guo, J. Zhu, *Photon radiation modelling in PMCS*, DØ Note 5657, (2008).

[56] T. Cole *et. al*, Technical report, Fermilab TM-1909, (1994).

[57] S. Mishra, *Presented at Particle Accelerator Conference (PAC 03)*, FERMILAB-CONF-03-194, (2003).

[58] V. Abazov *et. al*, *The Upgraded DØ Detector*, Nucl. Instrum. Methods Phys. Res., **A565**, 463, (2006).

[59] S. Abachi *et. al*, *The DØ Detector*, Nucl. Instr. and Methods, **A338**, 185, (1994).

[60] D. Perkins, *Introduction to High energy Physics*, Menlo Park: Addison-Wesley, (1987).

[61] R. Fernow, *Introduction to Experimental Particle Physics*, Cambridge: Cambridge University Press, (1986).

[62] R. Wiggmans, *Calorimetry*, Oxford: Clarendon Press, (2000).

[63] M. Wetstein *et al.*, *Gain Calibration for the EM Calorimeter in Run II*, DØ Note 5004, (2006).

[64] G. Grindhammer, S. Peters, *The Fast Simulation Of Electromagnetic And Hadronic Showers*, Nucl. Instrum. Methods, **A290**, 469, (1990).

[65] Application Software Group, *GEANT: Detector Description and Simulation Tool*, CERN Program Library Long Writeup, W5013.

[66] J. Stark, T. Andeen, *Electron response model*, DØ Note 5658, (2008).

[67] J. William, *Search for the Top Quark in the Muon + Jets channel at DØ* , PhD Thesis, State University of New York at Stony Brook, Stony Brook, New York (1994).

[68] F. James, M. Roos, *Minuit: A System for Function Minimization and Analysis of Parameter Errors and Correlations*, Comput. Phys. Commun., **10**, 343, (1975).

[69] T. Andeen *et. al*, *The DØ experiment's integrated luminosity for Tevatron Run IIa*, FERMILAB-TM-2365, (2006).

[70] D. Adams, *Finding Tracks*, DØ Note 2958.

[71] H. Greenlee, *The DØ Kalman Track Fit*, DØ Note 4303.

[72] A. Khanov, *HTF: histograming method for finding tracks: The algorithm description*, DØ Note 3778.

[73] G. Hesketh, *Central Track Extrapolation through the DØ Detector*, DØ Note 4079.

[74] H. Greenlee, *Motion of a Charged Particle in a Magnetic Field*, DØ Note 4180.

[75] H. Greenlee, *The DØ Interacting Propagator*, DØ Note 4293.

[76] A. Schawrtzman and M. Naraian, *Primary Vertex Selection*, DØ Note 3907.

[77] H. Schellman, *The longitudinal shape of the luminous region at DØ* , DØ Note 5142.

[78] T. Sjöstrand, Comput. Phys. Commun., **82**, 74, (1994); T. Sjöstrand, L. Lönnblad, S. Mrenna, P. Skands, Pythia 6.206, hep-ph/0108264, (2001).

[79] G. Ladinsky, C.-P. Yuan, *The nonperturbative regime in QCD resummation for gauge boson production at hadron colliders*, Physical Review D **50**, 4239, (1994).

[80] C. Balazs, C.-P. Yuan, *Soft gluon effects on lepton pairs at hadron colliders*, Physical Review D, **56**, 5558, (1997).

[81] E. Barberio, Z. Was, *PHOTOS–A universal Monte Carlo for QED radiative corrections. Verion 2.0* Comput. Phys. Communications, **79**, 291, (1994).

[82] P. Petroff *et. al*, *W Mass MC Closure Test*, DØ Note 5659, (2008).

[83] J. Zhu. Private talks at DØ .

[84] F. Guo, J. Guo, J. Zhu, *Correction to the electron energy cluster*, DØ Note 5660, (2008).

[85] F. Guo *et. al*, *Studies of energies below electron window for W mass measurement*, DØ Note 5661, (2008).

[86] T. Andeen, *Fit for Electron energy response*, DØ Note 5662, (2008).

[87] M. Wetstein, *WZ Fitter*, DØ Note 5663, (2008).

[88] M. Wetstein *et al.*, *Sampling Term in Run IIa*, DØ Note 5004, (2006).

[89] T. Andeen, *Constant term and Energy Nonlinearity*, DØ Note 5664, (2008).

[90] M. Cwiok, *Modeling the Hadronic Recoil*, DØ Note 5668, (2008).

[91] J. Stark, Private communication.

[92] J. Guo, Private communication.

[93] J. Guo, *Background Study for W Mass Measurement*, DØ Note 5665, (2008).

[94] *Jet Energy Scale Determination at DØ Run II (p17 version)*, DØ Note **5382**, (2007).

[95] U. Baur, D. Wackeroth, *Electroweak Radiative Corrections to* $p\bar{p} \rightarrow W^{\pm} \rightarrow l^{\pm}\nu$ *Beyond the Pole Approximation*, Phys. Review D, **70**, 073015, (2004).

[96] J. Guo *et. al*, *QED Uncertainty for the W Mass Measurement*, DØ Note 5666, (2008).

[97] S. Yacoob, *Description of the Transform Method W Mass Analysis at DØ* , DØ Note 5667, (2008).